THE UNIVERSITY *of* EDINBURGH

A computational framework for the discovery of retinal microvascular biomarkers of diabetes and renal disease

Ylenia Giarratano

THE UNIVERSITY *of* EDINBURGH
Edinburgh Medical School

Doctor of Philosophy

Edinburgh Medical School

University of Edinburgh

April, 2022

To Andrea,
my sister Myriam,
and
my parents for their
incommensurable love

Declaration

I declare that this thesis titled "A computational framework for the discovery of retinal microvascular biomarkers of diabetes and renal disease" has been composed by myself and this represents my own work except where due acknowledgements have been made. I further declared that this work has not been previously submitted to any other institution for a degree, diploma or professional qualifications.

Edinburgh, 2021

Ylenia Giarratano

Acknowledgements

First and foremost, I would like to express my immense gratitude to my principal supervisor Miguel O. Bernabeu for his guidance, encouragement, and endless support throughout the duration of this degree. His patience and counseling have constantly guided me in this journey, proving the great mentor he is. Similarly, I would like to thank my co-supervisors, Tom MacGillivray and Baljean Dhillon, for the technical and clinical expertise, for the insightful and enthusiastic comments during our meetings, and for monitoring my progress and offering advice and encouragement throughout. I would also like to express my sincere appreciation to Neeraj Dhaun, Rik Sarkar, Shareen Forbes, and Andrew Morris, for their enthusiasm for my topic, for the fruitful and stimulating discussions on clinical and computational aspects of this work – which were essential in helping me complete this project. A very special thank goes to Dan, Tariq, Laura, Emma, Eleonora, Calum, Alisa, Jie, Ian, Rowan, Rayna, and Alessandro, for their contributions to this research. I am very grateful to all fellow people in Miguel's group, Charles, Romain, David, Lowell, Claire, Darwon, Ellie, Xin, and Jess, for their invaluable support and beneficial social distractions. In particular, I would like to thank my colleague and friend Ana for her youthful spirit, patience, cooking skills, wine, and unfailing source of reassurance. I wish to thank all the members of the VAMPIRE group, especially Emanuele Trucco, for the warm welcoming in their team and the enthusiastic discussions. Thanks to the people in BioQuarter, Minhong, Holly, Pierre, Kevin, and Sofia for the laughs, food sharing, social breaks, and PhD advice. My heartfelt thanks are due to Agastya for her lovely weirdness and Alex for the very needed coffee breaks. I owe a debt of gratitude to Guido, Giulio, Andreas, Michalis, and Dimitrios, for firstly introducing me to the academic research, and my Precision Medicine DTP companions, Greg, Alex, Theoklis, and Giovanni with whom I shared courses, projects, and lovely walks. I welcome this opportunity to thank my friends Marisa, Malcolm, Valessia, and Giuseppe, for the social runs/walks and long-distance calls which have enormously contributed to my well-being during the pandemic. Finally, my acknowledgements would not be complete without thanking my family for their love and support, always and forever.

This work was supported by the Medical Research Council MRC Precision Medicine DTP (MR/N013166/1). All study participants, the NHS Lothian R&D, Edinburgh Imaging, and the Edinburgh Clinical Research Facility at the University of Edinburgh are gratefully acknowledged.

List of Publications

JOURNALS:

[1] Giarratano, Y., Bianchi, E., Gray, C., Morris, A., MacGillivray, T., Dhillon, B., Bernabeu, M.O.; Automated Segmentation of Optical Coherence Tomography Angiography Images: Benchmark Data and Clinically Relevant Metrics. Trans. Vis. Sci. Tech. 2020;9(13):5.

CONFERENCES:

[1] Giarratano, Y., Pavel, A., Lian, J., Andreeva, R., Fontanella, A., Sarkar, R., .. , Bernabeu, M.O. (2020). A Framework for the Discovery of Retinal Biomarkers in Optical Coherence Tomography Angiography (OCTA) In: Fu H., Garvin M.K., MacGillivray T., Xu Y., Zheng Y. (eds) Ophthalmic Medical Image Analysis. OMIA 2020. vol 12069. Springer, Cham.

[2] Andreeva, R., Fontanella, A., Giarratano, Y., Bernabeu, M.O. (2020). DR Detection Using Optical Coherence Tomography Angiography (OCTA): A Transfer Learning Approach with Robustness Analysis. In: Fu H., Garvin M.K., MacGillivray T., Xu Y., Zheng Y. (eds) Ophthalmic Medical Image Analysis. OMIA 2020. vol 12069. Springer, Cham.

ABSTRACTS:

[1] Giarratano, Y., Pavel, A., Lian, J., Sarkar, R., Reid, L., Forbes, S., Dhillon, B., MacGillivray, T., Bernabeu, M.O.; Optical coherence tomography angiography (OCTA) analysis of the diabetic eye: network-level vascular changes and patient classification. *Invest. Ophthalmol. Vis. Sci.* 2020;61(7):4105. (ARVO2020 conference)

[2] Bernabeu, M.O., Giarratano, Y., Pavel, A., Sarkar, R., Pugh, D., Farrah, T., Dhaun, N., Dhillon, B., MacGillivray, T.; Retinal vascular changes in chronic kidney disease and following kidney donation measured with Optical Coherence Tomography Angiography (OCTA). *Invest. Ophthalmol. Vis. Sci.* 2020;61(7):4834. (ARVO2020 conference)

[3] Giarratano, Y., Pavel, A., Lian, J., Sarkar, R., Pugh, D., Farrah, T., Dhaun, N., Dhillon, B., MacGillivray, T., Bernabeu, M.O.; Long-term risk assessment of living kidney donors: a retinal study. *Invest. Ophthalmol. Vis. Sci.* 2021;62(8):2484. (ARVO2021 conference)

DATASETS:

[1] OCTA-RSS: Optical Coherence Tomography Angiography retinal scans and segmentations. DOI: https://doi.org/10.7488/ds/2729.

Abstract

The retina is a thin layer at the back of the eye unique in allowing easy observation of blood vessels using simple and non-invasive instruments. The visualisation of the *in vivo* vasculature using retinal imaging has thereby become a key modality for the study of retinal phenotypes that can lead to the development of biomarkers for early detection not only of eye diseases but also of systemic diseases that may affect the cardiovascular system and the central nervous system.

In the last two decades, thanks to the advance in technology, new retinal imaging modalities have been introduced, optical coherence tomography (OCT) and OCT angiography (OCT-A), as new methods of visualising the neuro-retinal landscape. In particular, OCT-A, a fast and efficient technology, allows the visualisation of the vasculature at the capillary level. Considering changes in microvessel structure a common characteristic in cardiovascular disease, neurodegenerative disease, and diabetes, among others, this technology offers a unique opportunity to investigate and identify alterations associated with diseases and contribute to timely targeting patients at risk.

This thesis proposes a fully automated approach for the analysis of OCT-A images with the aim of providing novel retinal microvascular biomarkers for early detection of vascular changes and identification of disease status, realising the full potential of this imaging technology.

The first step of the OCT-A computational framework involves image processing and vessel segmentation. This is a crucial procedure in OCT-A analysis since results may be highly dependent on the accuracy of this task. To date, however, no standard blood vessel

segmentation for OCT-A images has been established. This work investigates the best image processing pipeline for this type of technology by creating an original OCT-A dataset (publicly available) and by scrutinising a large set of blood vessel segmentation methods. State-of-the-art handcrafted filters and deep learning approaches (DL) for medical images are surveyed and evaluated by using standard performance metrics and newly customised OCT-A vascular measures. Results show the preeminence of DL methods over handcrafted filters and the susceptibility of clinical measurements to each of the segmentation approaches, suggesting that precaution should be taken in performing meta-analyses.

The second step of the analysis concerns the processing of the segmented OCT-A images for the discovery of candidate retinal biomarkers. Despite the popularity of deep learning approaches, these methods require a large amount of labeled data for training purposes which are not always available. Therefore, using a network-based framework, this work takes advantage of a feature engineering approach instead. Structural and functional retinal characteristics are proposed based on the current clinical knowledge. Furthermore, novel microvascular metrics based on geometric and topological properties of the graph representation of the vasculature are implemented to cover the full spectrum of possible retinal measurements, enabling the hypothesis-free discovery of new clinically relevant biomarkers of diseases.

Finally, using the extracted OCT-A microvascular phenotypes, it is possible to explore associations with ocular and systemic dysfunctions and elucidate potential biological and physiological mechanisms linked to diseases. The same OCT-A measurements can also help to identify diseased patients by using machine learning models based on modestly sized image datasets and, contrarily to many deep learning approaches, without compromising features interpretability.

This thesis presents the application of the OCT-A computational framework in three case studies: diabetic retinopathy (DR), chronic kidney disease (CKD), and living kidney

donation. This framework enables to reproduce previous findings but also to show novel unreported changes. In the DR study, in accord with other investigations, results indicate a reduction in vascular skeleton density and an enlargement of the intercapillary spaces in the superficial layer of the retina. In the CKD study, changes to vessel radius and curvature of the foveal avascular zone are reported in patients with CKD when compared to healthy controls. The classification of participants, based on the retinal measurements extracted using the OCT-A computational framework, demonstrates that patients with DR are easier to identify than participants with diabetes without DR, whereas changes in patients with CKD are more subtle and challenging to detect.

The final application of the OCT-A computational framework involves participants who have donated a kidney. Despite living kidney donors being considered near-healthy patients, they are at higher risk of developing CKD and cardiovascular disease, and identifying those donors most at risk of these complications remains an open clinical challenge. The present research explores, for the first time, the possibility of using non-invasive imaging of the retinal microvasculature as a tool to improve the targeting of patients at-risk, and suggests that OCT-A microvascular phenotypes may shed light on the timing of vascular changes in kidney donors.

Studies over the past decades have provided important information about how changes in the retina vasculature can occur due to diseases years before other signs become apparent. This has led to an increasing interest in mining the retinal landscape for biomarkers of both ocular and systemic disease, and the emergence of OCT-A as a key modality for the study of the retinal microvascular system *in vivo*. This research proposes an automated framework for the analysis of OCT-A images and demonstrates the wide spectrum of clinical applications of this technology, showing the full potential of OCT-A imaging modality.

Lay summary

The eye is considered a window to many health conditions. By capturing images of the retina, a thin layer at the back of the eye rich in blood vessels, it is possible to detect alterations due to diseases. The study of blood vessel characteristics can reveal information about diseases of the eye and, more generally, diseases of other organs that affect indirectly the vessels in the retina.

Retinal imaging devices are medical technologies that enable the visualisation of the blood vessels in the eye allowing the diagnosis and the tracking of disease progression. Among those devices, optical coherence tomography angiography (OCT-A) captures images of the tiniest vessels in the retina in a fast and efficient way. This technology offers a unique opportunity to investigate diseases at the microvascular level, such as cardiovascular disease, diseases of the brain, kidney disease, and diabetes.

Even though OCT-A is a promising technology, its use in clinical practice is still under investigation. This thesis contributes to the realisation of the full potential of OCT-A imaging device by developing a framework for the analysis of images captured using this technology, and by proposing new measurements to characterise small blood vessels in the eye that can help to detect alterations in the retina and contribute to guiding clinicians in identifying patients at risk or monitoring disease progression.

The use of the OCT-A computational framework is presented in three case studies. The first application concerns the investigation of changes in the eye in patients with diabetic retinopathy, a complication of diabetes. Results align with previous findings reported in other studies, validating the capability of the framework in measuring changes in the eye and the reproducibility of other investigations. The second application involves a cohort of

patients suffering from chronic kidney disease, a condition that describes the progressively decrease in kidney function. Indeed, eye and kidney present similar structural traits, and diseases of the two organs are closely linked. Results suggest that changes in the eye due to chronic kidney disease might be challenging to detect, and further investigations are needed to exploit the potential of the OCT-A technology in renal disease.

The final application investigates the long-term risk assessment of kidney donation. Recent studies have shown that kidney living kidney donors are at higher risk of developing cardiovascular disease and kidney disease. However, identifying those most at risk is a clinical unmet challenge. Using retinal measurements computed by the framework, results suggest that it may be possible to gain further information about long-term risk assessment of kidney donation and timely target patients at risk by monitoring alterations in the eye using OCT-A technology.

Changes in the eye have been reported in multiple ocular and systemic diseases, even years before other symptoms manifest. Therefore, over the past decades, retinal imaging has become a key tool for the investigation of many conditions. This thesis proposes an automated framework for analysis of OCT-A retinal images that lays the foundation of a novel approach to characterise changes in the eye accelerating the implementation of patient-specific approaches to achieving precision medicine.

Contents

List of Figures

List of Tables

List of Acronyms & Abbreviations

ACC	Accuracy
AD	Alzheimer's Disease
AMD	Age-related Macula Degeneration
AT	Adaptive Thresholding
AUC	Area Under Curve
CCP	Choroid Capillary Plexus
CKD	Chronic Kidney Disease
CNN	Convolutional Neural Network
CNV	Choroidal Neovascularisation
CODAA	Complex OCT-signal Difference Analysis Angiography
CS-Net	Channel Spatial U-Net
CVD	CardioVascular Disease
DCEL	Double Connected Edge List
DCP	Deep Capillary Plexus
DL	Deep Learning
DM	Distance Metric
DR	Diabetic Retinopathy
DRIVE	Digital Retinal Images for Vessel Extraction
ESKD	End Stage Renal Disease
ETRS	Early Treatment of Diabetic Retinopathy Study
F	Foveal
FA	Flourescein Angiography
FAZ	Foveal Avascualar Zone
FD	Fractal Dimension
FI	Flow Index

FN	False Negative
FOV	Field Of View
FP	False Positive
K-NN	K-Nearest Neighbours
I	Inferior
ICP	Intermediate Capillary Plexus
ILM	Inner Limiting Membrane
IOP	IntraOcular Pressure
IPL	Inner Plexiform Layer
LR	Logistic Regression
ML	Machine Learning
MS	Multiple Sclerosis
MSE	Mean Square Error
MSFD	MultiSpectral Fractal Dimension
N	Nasal
NPDR	NonProliferative Diabetic Retinopathy
NTG	Normal-Tension Glaucoma
OAG	Open Angle Glaucoma
OCT	Optical Coherence Tomography
OCT-A	Optical Coherence Tomography Angiography
OCTA-RSS	OCTA Retinal Scans and Segmentations
OCTARA	OCTA Ratio Analysis
OMAG	Optical MicroAnGiography
ONH	Optic Neuritis History
OOF	Optimal Oriented Flux
OR	Outer Retina
PAN	Percentage Area Non-perfusion
PDR	Proliferative Diabetic Retinopathy
PH	Persistent Homology
RAO	Retinal Artery Occlusion
ReLU	Rectified Linear Unit

RF	Random Forest
RNFL	Retinal Nerve Fibre Layer
ROI	Region Of Interest
RVO	Retinal Vein Occlusion
S	Superior
SCC	Slope Chain Code
SCIRD-TS	Scale and Curvature-Invariant Ridge Detector for Thin Structures
SCONe	Scottish Collaborative Optometry-Ophthalmology Network e-research
SCP	Superficial Capillary Plexus
SD	Standard Deviation
SD-OCT	Spectral Domain OCT
SE	Standard Error
SEN	Sensitivity
SGD	Stochastic Gradient Descent
SLO	Scanning Laser Ophthalmoscopy
SOA	Spectral-domain OCT Angiography
SOAM	Sum Of Angles Metric
SSADA	Split-Spectrum Amplitude-Decorrelation Algorithm
SS-OCT	Swept Source OCT
SPE	Specificity
STARE	Structural Analysis of the REtina
SVD	Small Vessels Disease
SVM	Support Vector Machine
T	Temporal
TL	Transfer Learning
TNR	True Negative Rate
TPR	True Positive Rate
VD	Vessel Density
VEGF	Vascular Endothelial Growth Factor
UWF	Ultra Wide Field
WF	Wide field

W Whole

Chapter 1

Introduction

1.1 Background and motivations

The retina is a thin layer of tissue in the eye unique in allowing easy observation of blood vessels using simple and non-invasive instruments. It lines the inner surface of the human eye and comprises layers of tissue made of neurons and supporting cells. Its strategic importance is due to the fact that it is also the only accessible site for live imaging the blood vessels *in vivo*. Retinal imaging devices are commonly used for monitoring eye health conditions and for the diagnosis of retinal disease. The principal imaging modalities are: *fundus camera*, the union of a low power microscope and a camera, *fluorescein angiography* (FA), a dedicated fundus camera equipped with filters that requires intravenous administration of a contrast agent in the eye, and *optical coherence tomography* (OCT), a non-invasive technology for *in vivo* cross-sectional imaging. These standard retinal imaging techniques are widely used to provide information on healthy and diseased vasculature. However, these technologies fail to visualise the finest capillary network due to limited imaging resolution or the requirement of the invasive use of contrast agents, which may carry the risk of adverse reactions. Recently, a more powerful technique has been developed: optical coherence tomography angiography (OCT-A). It is a non-invasive technique capable of resolving the microvasculature of the retina to the deepest levels of detail without requiring a dye injection. Recent studies have provided promising results about how changes in the retinal microvasculature can occur due to diseases years before other signs become apparent and how technology like OCT-A can become a key modality for the study of microvascular diseases. Nonetheless, the potential

of OCT-A in clinical diagnostic is still under investigation. Changes in blood vessels have close relationships with many systemic, metabolic, and hematologic conditions. Consequently, morphological and functional properties of the retinal vasculature can be used to identify and classify the severity of ocular and systemic diseases. Early identification of pathological conditions such as diabetic retinopathy [1], chronic kidney disease [2], cardiovascular diseases [3], and neurodegenerative diseases [4], through features derived from retinal imaging, would add further insights into these conditions, allowing the classification of patients at risk and the identification of people who may benefit from preventative therapies.

1.2 Thesis objectives

The aim of this thesis is to provide an automated computational framework for the discovery of retinal microvascular biomarkers in OCT-A imaging and demonstrate the potential of this technology. To achieve this goal, this thesis contributes as follows.

1. The creation of the first publicly available open dataset of OCT-A images with corresponding ground truth segmentations (manually performed by myself) [5].

2. The comparison of state-of-the-art segmentation methods in OCT-A imaging with the goal of assessing a standardised image processing pipeline for this technology. Several approaches have been proposed in the literature for retinal vessel segmentation, however, how they compare to each other is not known. Using the previously generated open dataset, it is possible to compare those methodologies against each other and benchmark future research. Furthermore, how each segmentation method can affect clinical measurements is explored [5].

3. The development of a network-based framework for the modeling of the retinal microvasculature in OCT-A images and the extraction of morphological retinal microvascular phenotypes to assess and characterise microvascular changes [6].

4. The implementation of novel retinal vascular metrics able to capture geometric, topological, and functional properties of the vasculature [6].

5. The classification of patient status in three case studies, diabetic retinopathy, chronic kidney disease, and living kidney donation, using machine learning models and the novel OCT-A retinal microvascular phenotypes extracted using the computational framework [6].

An overview of the OCT-A computational framework is depicted in figure 1.1.

1.3 Thesis outline

The thesis is organised as follows. Chapter 2 provides the necessary background to retinal imaging modalities, focusing on OCT-A technology and its applications to ocular and systemic disease. Chapter 3 introduces the investigation of several segmentation methods to establish a standard for OCT-A image segmentation. It describes the creation of the open dataset with manually segmented images, and the comparison of different algorithms evaluated on pixelwise, topological, and clinical metrics. Chapter 4 concerns the description of the network-based framework for the modeling of the vasculature as a graph, the implementation of known and novel retinal phenotypes involving structural and functional properties of the vasculature, and the assessment of the robustness of the microvasculature features. Chapter 5 presents the first application of the computational framework to the NHS Lothian cohort, concerning the characterisation of retinal changes in diabetic patients with and without diabetic retinopathy. Retinal vascular phenotypes obtained using this framework are used to assess differences across groups of participants and to build machine learning models for disease detection. Chapter 6 describes the application of the framework to chronic kidney disease, a systemic condition with a retinal vascular footprint. Retinal vascular features are used to investigate associations with disease and to construct different machine learning models to identify patients with impaired renal function. Chapter 7 provides an exploratory study on the risk assessment of kidney donation by using OCT-A retinal features. Cross-sectional and longitudinal analyses are presented to gain insights into retinal vascular changes in living kidney donors. Finally, chapter 8 concludes with a summary of the key motivations and main contributions of this thesis and a discussion on future work.

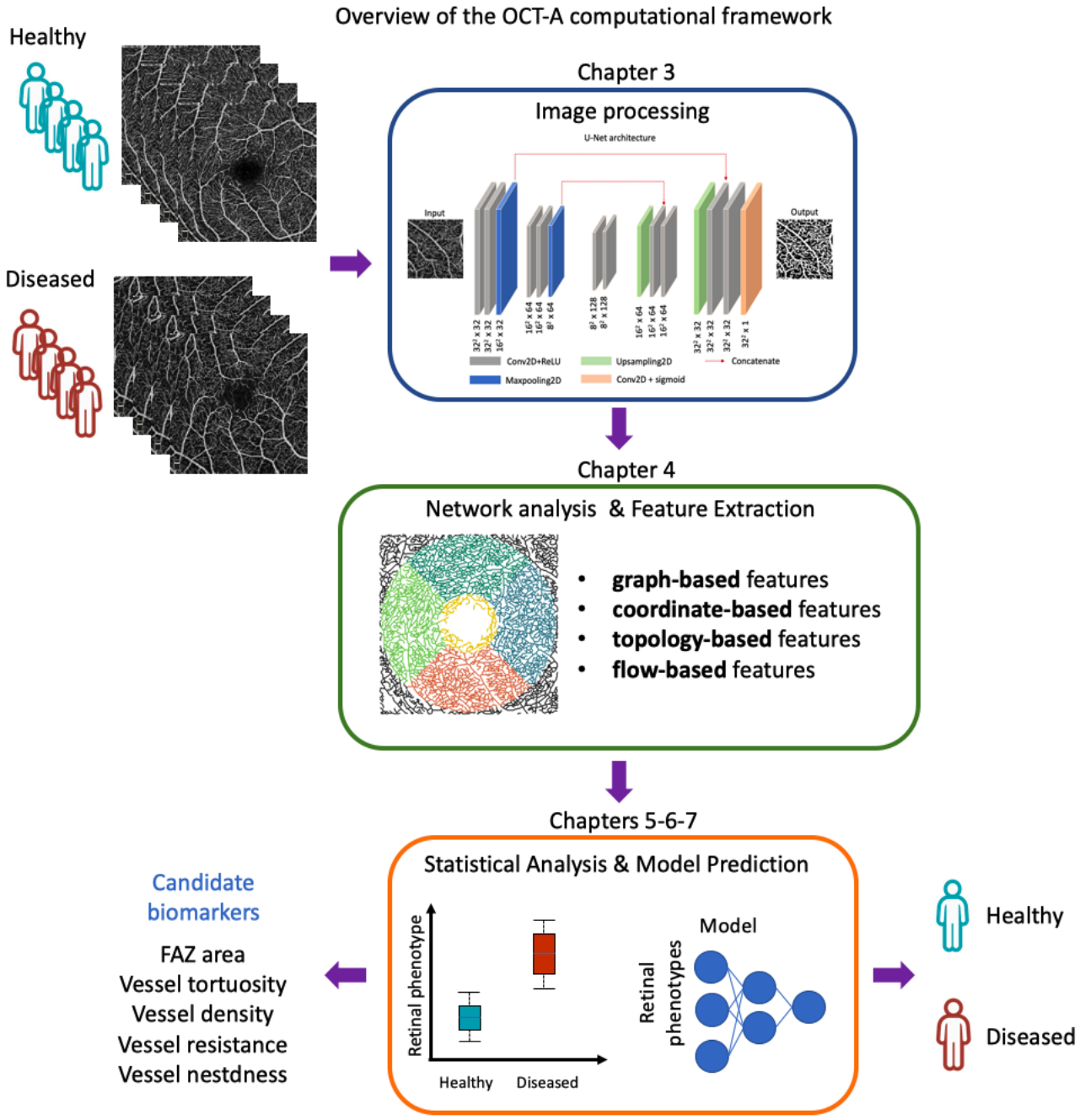

Figure 1.1: Overview of the OCT-A computational framework.

Chapter 2

Retinal imaging & OCT-A clinical applications

2.1 Introduction to retinal imaging

The retina is a neurosensory tissue at the back of the eye containing photoreceptor cells responsible for capturing light and transmitting signals to the brain through the optic nerve (figure 2.1). It is covered with an intricate structure of vascular networks of large and small vessels which spread across the different layers to supply blood and nutrients to each cell of the retinal tissue. Thanks to the transparency of the ocular media, which allows the light to penetrate and reach the photoreceptors, the retina can be considered as a window into the human body. In fact, using retinal imaging is possible to visualise *in vivo* and in a non-invasive way part of the cardiovascular system, and portions of neural tissue (since eyes are a developmental outgrowth of the brain), allowing the investigation not only of eye diseases but also cardiovascular diseases, neurodegenerative diseases, and systemic diseases that might manifest in the eye.

This chapter begins with an overview of common retinal imaging modalities, fundus photography, fluorescein angiography (FA), optical coherence tomography (OCT), and OCT-Angiography (OCT-A). Basics to understand OCT-A technology are introduced to explain image generation and differences across OCT-A retinal devices. Finally, common OCT-A measurements and their applications to investigate ocular diseases as well as systemic diseases are discussed to highlight the clinical potential of this technology.

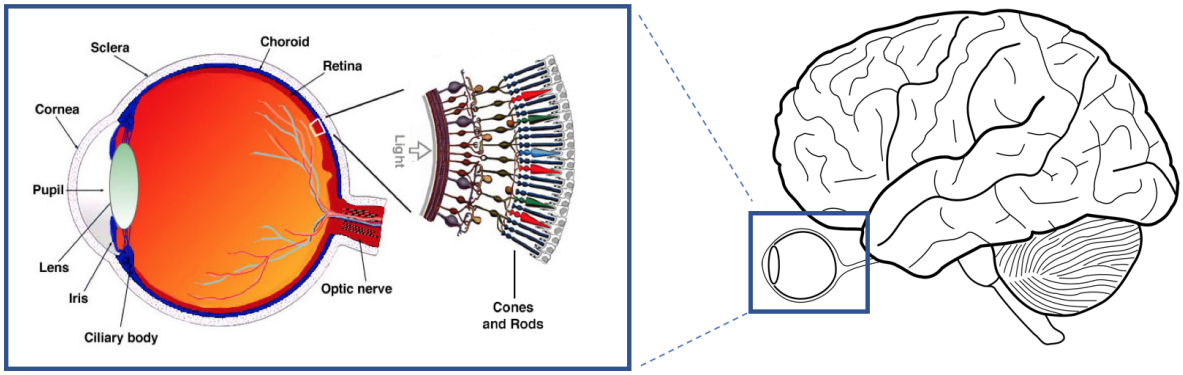

Figure 2.1: Eye anatomy with zoom into retinal layers (image adaptation from [7]).

2.2 Fundus photography

Colour fundus photography has been for many years the main imaging modality for capturing images of the retina. Similar to an ophthalmoscope, this device is the union of a low power microscope and a camera that allows to capture pictures of the retinal landscape, its major vessels, and the optic nerve with a field of view (FOV) typically in the range of 30° to 50°, as shown in figure 2.2A.

With the advance in technology more sophisticated cameras have been developed to facilitate image acquisition and to improve image quality. Hence, novel modalities have emerged to acquire fundus images. Scanning laser ophthalmoscopy (SLO) exploits the use of a monochromatic laser beam with narrow wavelength bands to minimise aberrations due to poor pupil dilatation and to produce high contrast and detailed retinal images. The laser beam scans the fundus of the eye following a raster pattern and the light reflected back from each retinal point is captured by a detector that converts the light into an electrical signal. An example of SLO retinal scan is shown in figure 2.2B. By using multiple monochromatic lasers, it is also possible to selectively acquire structural information at different depths in the retina and generate a pseudo-colour image as shown in figure 2.2C. Other innovations of fundus photography, such as widefield (WF) and ultra-widefield (UWF) fundus imaging have been developed to acquire images with wider FOV, able to capture the periphery of the retinal where early changes due to diseases might occur. These extensions are able to acquire images up to 200° and to capture the 82% of the retina surface (figure 2.2D).

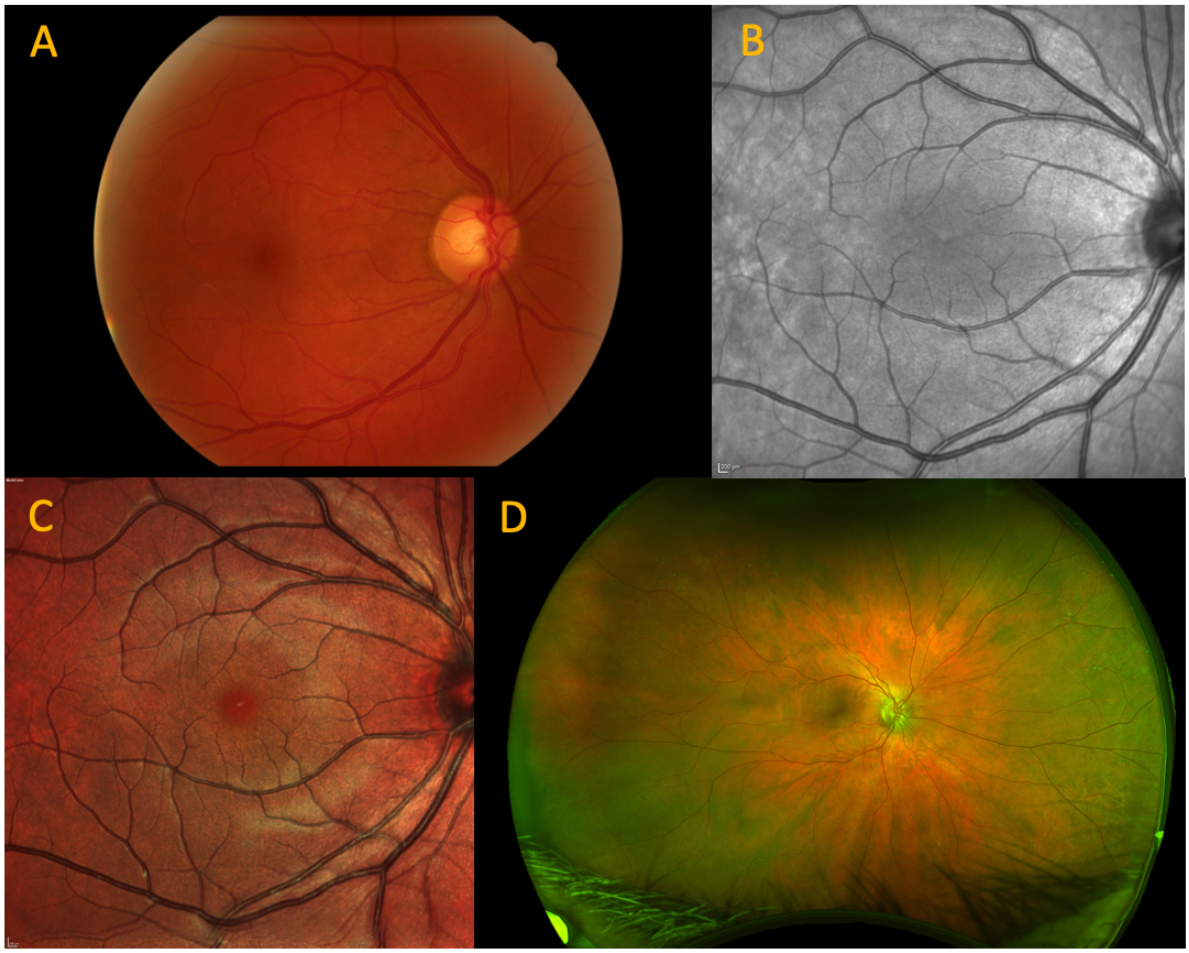

Figure 2.2: (A) Fundus photography. (B) Monochromatic SLO. (C) Multicolour SLO. (D) Ultra-widefield fundus photography.

Fundus photography is widely used for diagnostic purposes of ocular conditions such as age-related macular degeneration, glaucoma, retinal detachment, and diabetic retinopathy. As one of the oldest and still the most prominent imaging modality, large fundus camera imaging datasets have been collected to develop methodologies and meta-analyses, from vessel segmentation to disease prediction. Among these collections, DRIVE [8], STARE [9], and MESSIDOR [10] are some of the open publicly available fundus image datasets. Moreover, databanks such as UKBiobank [11] and SCONe [12], containing thousands of fundus camera images, demographic information, and genetic data are available to researchers to investigate multiple diseases at the population level.

2.3 Fluorescein angiography

Fluorescein Angiography (FA) is a technique that requires a dye injection and a fundus camera equipped with excitation wavelengths. Described for the first time by Novotny and Alvis in 1961 [13], this technique is considered the gold standard for understanding the circulation in the retina. The technical principle is based on the fluorescence phenomenon. When susceptible molecules are excited to a higher energy state, they produce photoluminescence. Therefore, the FA procedure requires a dye injection into the bloodstream of the patient, then using excitation wavelengths it is possible to track the flow in the retina. Excitation of fluorescein sodium molecules (the one used in FA) occurs at wavelengths between 465-490 nm, with the fluorescence occurring at the yellow-green wavelengths of 520 to 530 nm. Advantages of FA include heamodynamic information, the visualisation of small capillaries in the center of the retina (*i.e.*, macula), and the assessment of dye leakages. However, it is characterised by small FOV and low depth resolution. Moreover, dye injection is an invasive procedure requiring skilled personnel, causing patient discomfort, and at risk of possible adverse reactions. Figure 2.3 shows two examples of fundus fluorescein angiography images at different time points.

Fluorescein angiography is currently used to acquire more information about the extent of damage to the retina after the diagnosis of ocular diseases such as diabetic retinopathy, age-related macular degeneration, and vascular occlusions. This technique is also applied for prognostic evaluation and to track disease progression or to monitor the results of treatment.

Figure 2.3: Fundus image with the corresponding FA after 30 seconds and 6 minutes. Images from [14].

2.4 Optical coherence tomography (OCT)

Introduced in the early 1990's, optical coherence tomography (OCT) has revolutionised retinal imaging research by providing *in vivo* cross-sectional images of the eye (figure 2.4)[15]. Although systems can differ in broadband sources and signal processing procedures, the basic principle can be summarised as shown in figure 2.5A. The light generated by a broadband source is split into equal beams directed toward two different paths, the reference arm and the sample arm. The beam of the first arm is reflected back by a mirror, whereas the beam in the sample arm scans the target tissue. By measuring the interference between the reflected beam from the reference arm and the backscattered signal from the sample arm it is possible to extract axial structural information of the tissue that can be represented as an A-scan (see figure 2.5B). Multiple A-scans can then be performed laterally to obtain the cross-sectional image of the tissue. Images can be acquired in real-time and with axial resolution in the range of 5-15 μm. This allows ophthalmologists to measure the thickness of the retinal layers and assess associations with histopathologic findings. Dilatation of the choroidal thickness caused by the increase of vessel width, for example, can lead to increase blood pressure and vessel permeability. Thinning of the choroidal layer can cause dysfunctions in blood and nutrients supply, leading to photoreceptor cell death.

OCT technology has found applications in many diseases such as retinal edema, retinal detachment, diabetic retinopathy, chronic kidney disease, and multiple sclerosis. Current innovations in OCT have expanded the potential of this device beyond retinal imaging. Its ability to visualise nontransparent tissues and provide real-time images has found also applications in dermatology, biopsy, and guided surgery [16]–[18].

2.5 OCT-Angiography (OCT-A)

Although fundus photography produces realistic colour images of large vessels, it fails in capturing the smallest capillaries nourishing the retina. Optical coherence tomography angiography (OCT-A) is a relatively novel imaging technology (commercially available since 2015) that allows the *in vivo* visualisation of the retinal vasculature in a fast and non-invasive way. A sequence of A-scans in the axial direction is acquired at high speed to

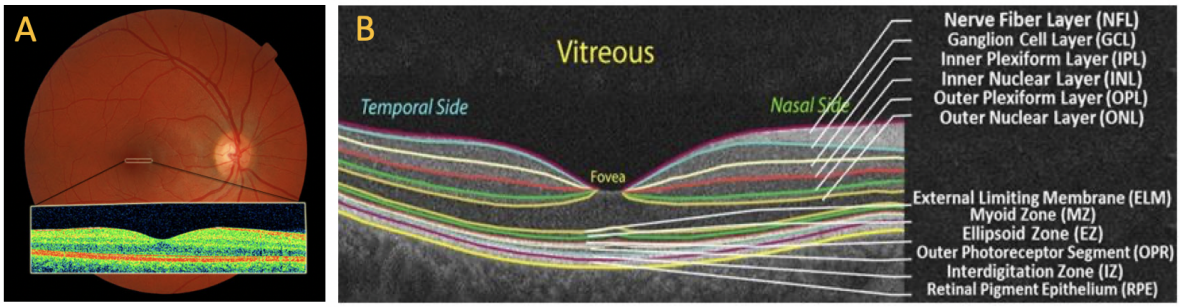

Figure 2.4: (A) OCT scan of the foveal region in a healthy patient. Image from [19]. (B) OCT scan with labeled retinal layers. Image from [20].

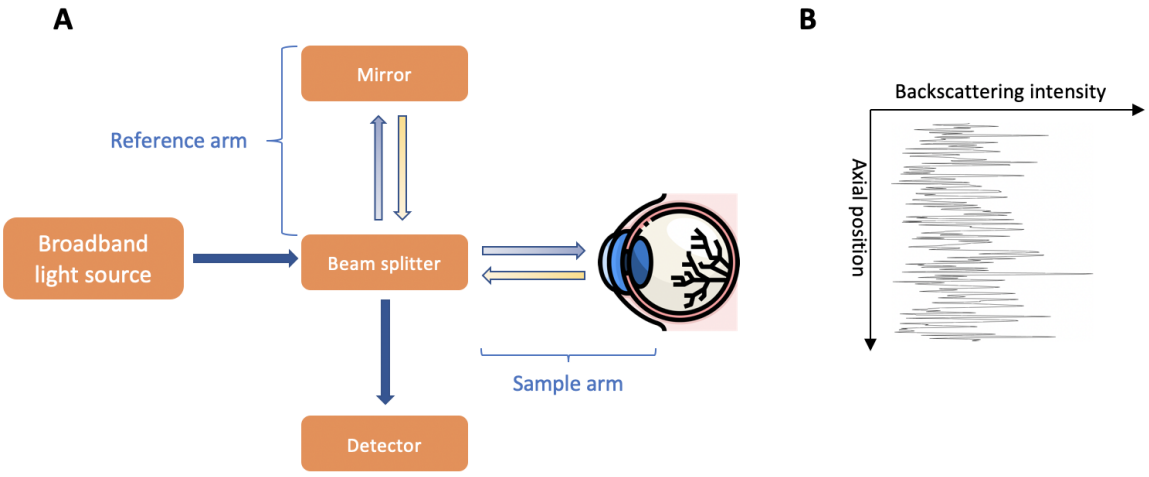

Figure 2.5: (A) Schematic overview of an OCT system. (B) OCT image reconstruction.

generate cross-sectional B-scans (brightness amplitude scans). Comparing the differences in the OCT signal intensity (decorrelation signal) between sequential B-scans captured at the same position in the retina allows the generation of a blood flow map (OCT angiography data). Static tissue will remain steady across B-scans, while moving blood cells in the vessels will show high variance in the OCT signal. Finally, the OCT-A software creates a 3D volumetric OCT image which is used to identify the different layers in the retina. The projection of the 3D volume on the z-axis produces the 2D *en face* angiogram at different depths as shown in figure 2.6.

OCT-A devices produced by different manufacturers apply different algorithms to obtain B-scans. Furthermore, OCT-A images captured by different systems can differ in field of view. Common FOV areas are 3×3 mm^2 and 6×6 mm^2 centered either at the foveal

region in the retina or at the optic nerve. In general, all devices provide images at four different depths, superficial capillary plexus (SCP), deep capillary plexus (DCP), choroid capillary plexus (CCP), and outer retina (OR). However, definitions of SCP and DCP can be different across devices. SCP is usually defined as the part of the tissue enclosed by the inner limiting membrane (ILM) and the beginning of the inner plexiform layer (IPL), whereas the DCP extends from the bottom of the IPL to the outer plexiform layer (OPL). Recent studies [21], [22], have also proposed the addition of an intermediate capillary plexus (ICP), as a border between SCP and DCP, including the IPL and inner nuclear layer (see figure 2.4B). An overview of the different output images obtained from the OCT-A device RTVue XR Avanti (Optovue, Inc., Fremont, CA, USA) using a $6 \times 6\ mm^2$ FOV is shown in figure 2.7. Figure 2.8 displays OCT-A images of the optic disc which allow the investigations of diseases affecting the optic nerve, such as glaucoma and other neurodegenerative conditions.

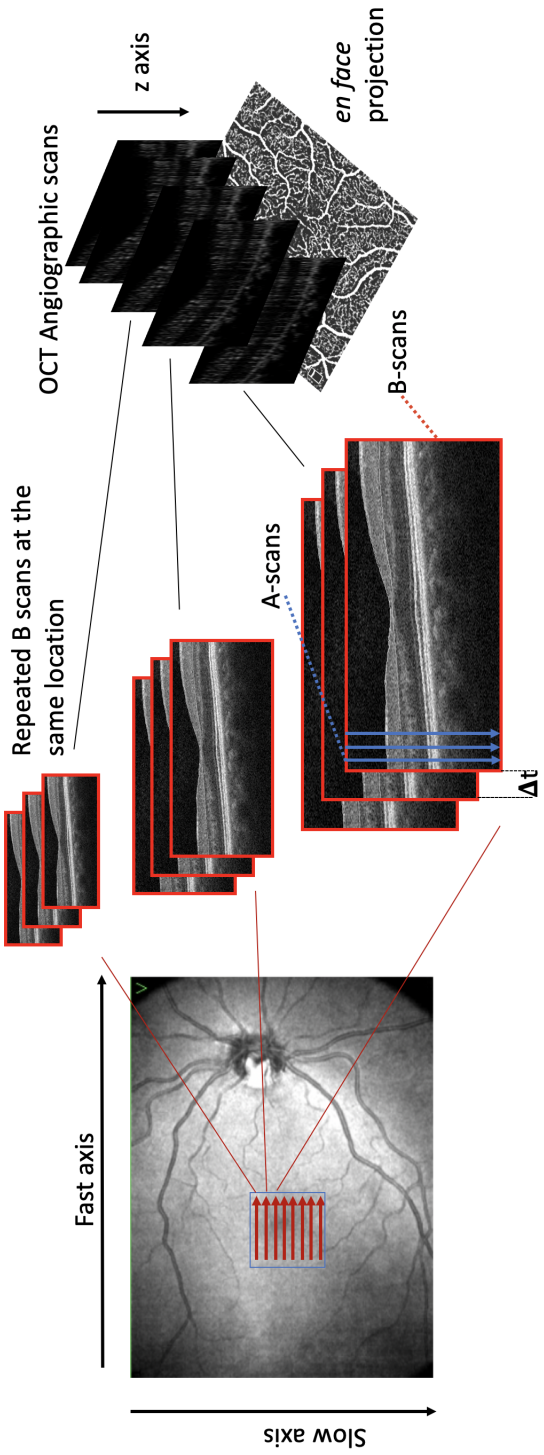

Figure 2.6: Overview OCT-A system. Rapid A-scans (in blue) generate the B-scans. Repeated B-scans at the same location are then used to create OCT angiographic data. The projection of the 3D OCT volume creates the final OCT-A.

2.5.1 OCT-A devices

A summary of commercially available OCT-A devices, from different manufacturers, is shown in Table 2.1. Two groups of OCT-A technology can be distinguished according to the type of OCT system. Devices using a broadband source with center wavelength of 840 nm and a spectrometer as detector of the interference are known as spectral-domain OCT or SD-OCT, whereas instruments using a range of optical frequencies (usually centered ∼1050 nm) are called swept-source OCT or SS-OCT. SD-OCT devices include the RTVue XR Avanti (OptoVue), Spectralis OCT2 (Heidelberg), CIRRUS HD-OCT 5000 (Carl Zeiss), Revo NX (Optopol), OCT-HS100 (Canon), and RS-3000 Advance (Nidek). PlexElite (Carl Zeiss) and DRI Triton (Topcon) are more recent SS-OCT devices. It is worth mentioning that algorithms used to generate the OCT angiographic data may differ across OCT-A devices. This can lead to non-identical OCT-A measurements that are not directly comparable. Recent studies investigating the robustness and the reliability of OCT-A measures across different devices have reported poor agreement among systems [23], [24]. The work developed in this thesis is based on images acquired by the same OCT-A device, the RTVue XR Avanti. Both SCP scan, from the internal limiting membrane (ILM) to the inner plexiform layer (IPL) and DCP (from IPL to the outer plexiform layer (OPL) scans with $3 \times 3\ mm^2$ FOV (figure 2.9) are employed to extract retinal microvascular phenotypes (chapter 4).

2.5.2 OCT-A: advantages and limitations

OCT-A technology offers the advantage of visualising the microvasculature in the eye at its finest details. Contrarily to FA, it is fast and does not require a dye injection associated with the risk of adverse reaction. Since it uses volumetric data, OCT-A gives the possibility of capturing vessels in the different layers of the retina, and images can be visualised as *en face* (2D projection) and cross-sectionally. Despite the potential of this technology in clinical applications and the advantages with respect to other imaging modalities, there are still some limitations to overcome. OCT-A device is very sensitive to eye movements. Motion artifacts can arise from patients moving during the scan acquisition, causing stretching and quilting defeats (figure 2.10A-B). Better B-scans registration and correction algorithms are currently under investigation to cope with these artifacts and may be

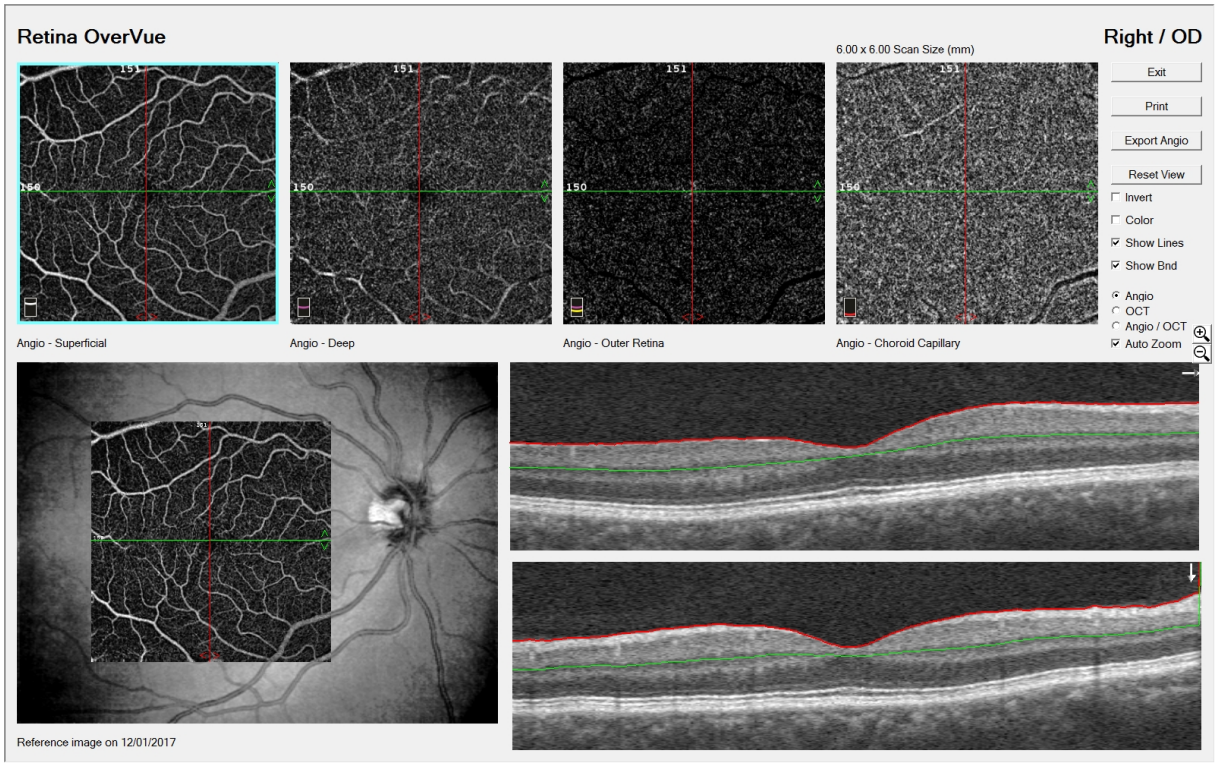

Figure 2.7: Overview of output centered at the foveal region in the AngioVue system RTVue XR Avanti (Optovue, Inc., Fremont, CA, USA).

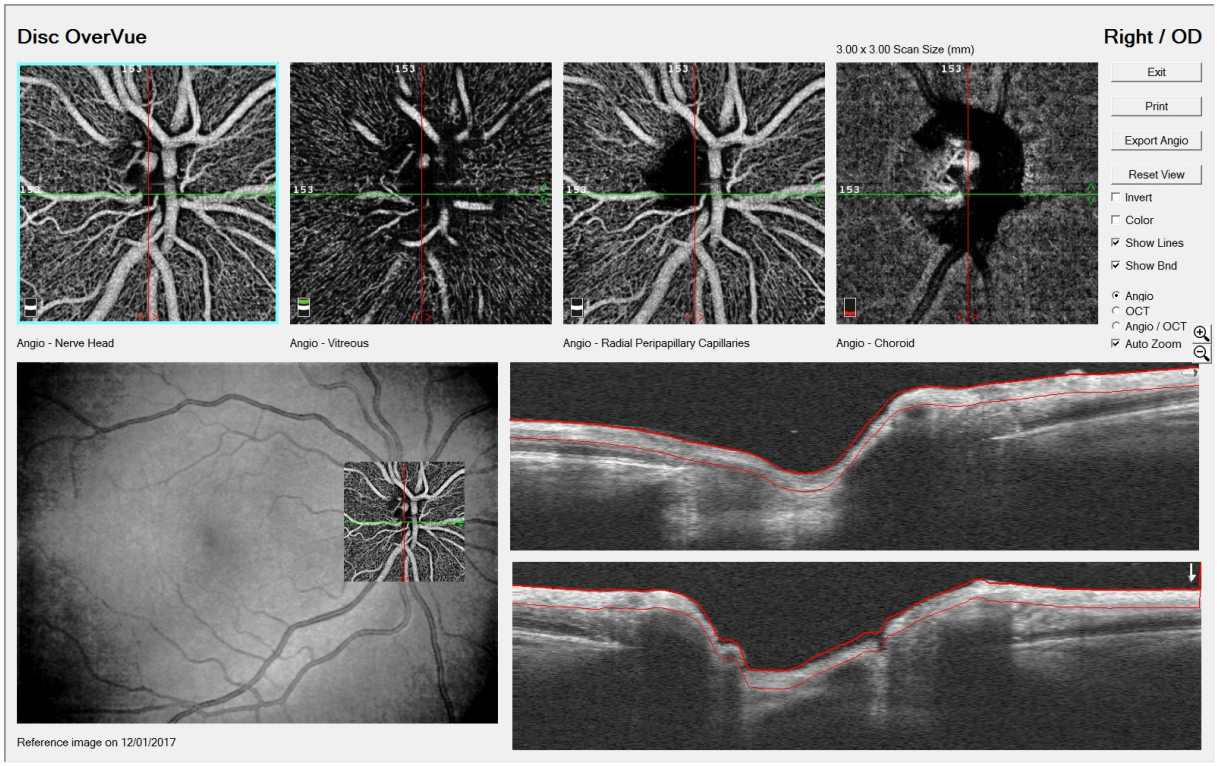

Figure 2.8: Overview of output centered at the optic disc in the AngioVue system RTVue XR Avanti (Optovue, Inc., Fremont, CA, USA).

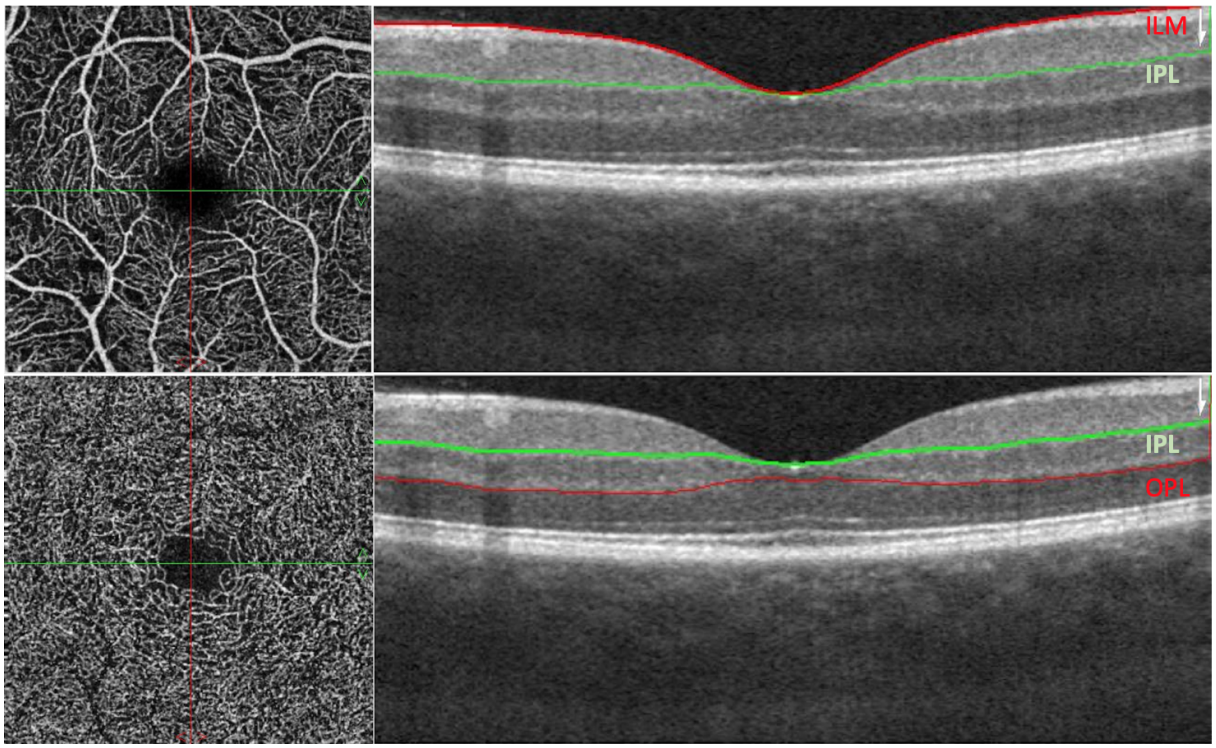

Figure 2.9: OCT-A scans of SCP and DCP with corresponding OCT scans).

Device	Manufactorer	Technology	Wavelength	Algorithm	OCT-A size (pixels)
RTVue XR Avanti	OptoVue, Fremont Inc.	SD-OCT	840 nm	SSADA [25]	304 × 304
Spectralis OCT2	Heidelberg Engineering	SD-OCT	870 nm	Probabilistic OCTA Algorithm [26]	512× 512
CIRRUS HD-OCT 5000	Carl Zeiss Meditec Inc.	SD-OCT	840 nm	OMAG [27]	245 × 245
RS-3000 Advance	Nidek	SD-OCT	880 nm	CODAA [28]	256 × 256
OCT-HS100	Canon New Zealand	SD-OCT	855 nm	Full spectrum [29]	232×232
Revo NX	OPTOPOL Technology	SD-OCT	830 nm	SOA [30]	512× 300
DRI Triton	Topcon Corporation	SS-OCT	1050 nm	OCTARA [31]	256× 256
PlexElite	Carl Zeiss Meditec Inc.	SS-OCT	1060 nm	OMAG	300×300

SSADA: split-spectrum amplitude-decorrelation algorithm, **OMAG**: optical microangiography, **CODAA**: complex OCT-signal difference analysis angiography, **SOA**: spectral-domain OCT angiography, **OCTARA**: OCTA Ratio Analysis.

Table 2.1: Technical characteristics of eight different OCT-A systems.

available in future software updates. Projection artifacts are observable on the *en face* image when vessels from superficial layers are falsely visualised also in deeper layers obscuring deeper vessels (figure 2.10C-D). Opacification of the ocular media can lead to

low signal causing light aberration and artifacts in the final projection. It should be pointed out that OCT-A is based on the motion of blood cells along vessels, however, the actual blood flow is not detectable in the current commercially available devices [32], [33]. Furthermore, if the motion of the erythrocytes (blood cells) is below the device sensitivity threshold, vessels are not detected.

Finally, built-in OCT-A software offers the opportunity of computing retinal measurements that can help in the assessment of disease status. However, these measurements rely on algorithms that are different across OCT-A instruments and often undisclosed by the manufacturer due to commercial sensitivities. It should be also noted that measurements can be influenced by common ocular problems such as myopia where the eye axial length affects the image acquisition leading to possible bias in the measurements [34], [35].

2.6 OCT-A analysis and clinical measures

To investigate the clinical potential of OCT-A imaging, studies have been focusing on the extraction of retinal phenotypes able to distinguish between healthy and diseased microvasculature. The majority of these investigations utilises a small set of metrics derived by using either the built-in OCT-A software or customised imaging processing pipelines. The most common measurements are **vessel density (VD)**, defined as the ratio between the white pixels in a binarised OCT-A image and the total number of pixels in the scan, and metrics associated with the **foveal avascular zone (FAZ)** (figure 2.11). FAZ is the region at the center of the retina free from blood vessels and responsible for the sharpest view since the light can reach directly photoreceptor cells without the aberration of the vasculature. Besides FAZ area and perimeter, studies have shown that FAZ shape is an important clinical biomarker [36]–[38], hence many metrics have been implemented to capture geometrical characteristics of this region. Among those, the **acircularity index (AI)** describes how close to a circle is the shape of the FAZ, and major and minor axis passing through the FAZ center can be used to compute the **axis ratio** [36], [37].

Another prominent metric used to characterise the complexity of the vascular pattern appearing in OCT-A images is **fractal dimension (FD)**. Fractals are used to describe the

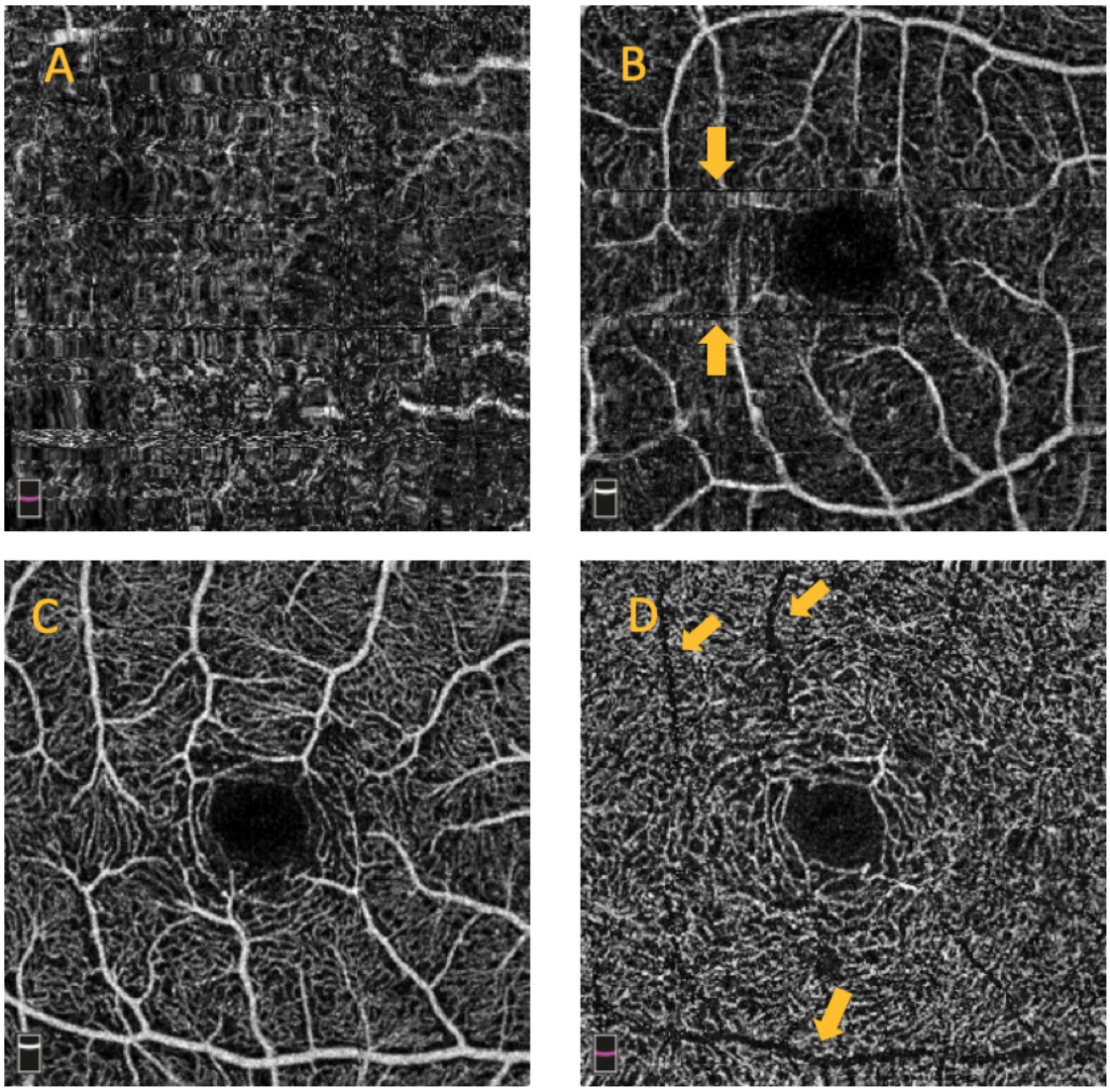

Figure 2.10: Motion artifacts. (A) Quilted artifacts, (B) stretches defects, (C) SCP scan, (D) Projection artifacts (yellow arrows) on DCP scan.

degree of complexity of biological structures. It is obtained by knowing two quantities, the number of pieces (N), and the magnification factor (s). In image processing, it is usually estimated by applying the *box counting* method where the image is progressively divided into boxes of smaller and smaller size to analyse patterns at different scales [39]. The boxes containing vessels are counted at each scale and the slope of the regression line

$$logN = (FD) \log s$$

corresponds to the estimated fractal value. Finally, another popular metric is the **flow index (FI)** computed as the average of the decorrelation values and used to capture haemodynamic information in OCT-A scans [40]–[43].

Despite the clinical potential of these metrics, their accuracy and reproducibility rely on the quality of the image processing which can be either undisclosed by the manufacturer or customised for the purpose of a study. This lack of standardisation in the image processing pipeline can lead to incomparable results across studies and undermine the reproducibility of the analysis. A step towards standardisation has been made by recent studies which have publicly shared OCT-A imaging datasets to compare and benchmark different methodologies for OCT-A image analysis ([5], [44], [45]).

Finally, many clinical studies exploit measurements computed by the built-in OCT-A software. Although useful, these limited number of features are not representative of the wide spectrum of retinal phenotypes and possibly are not sufficient to univocally characterise ocular and systemic diseases.

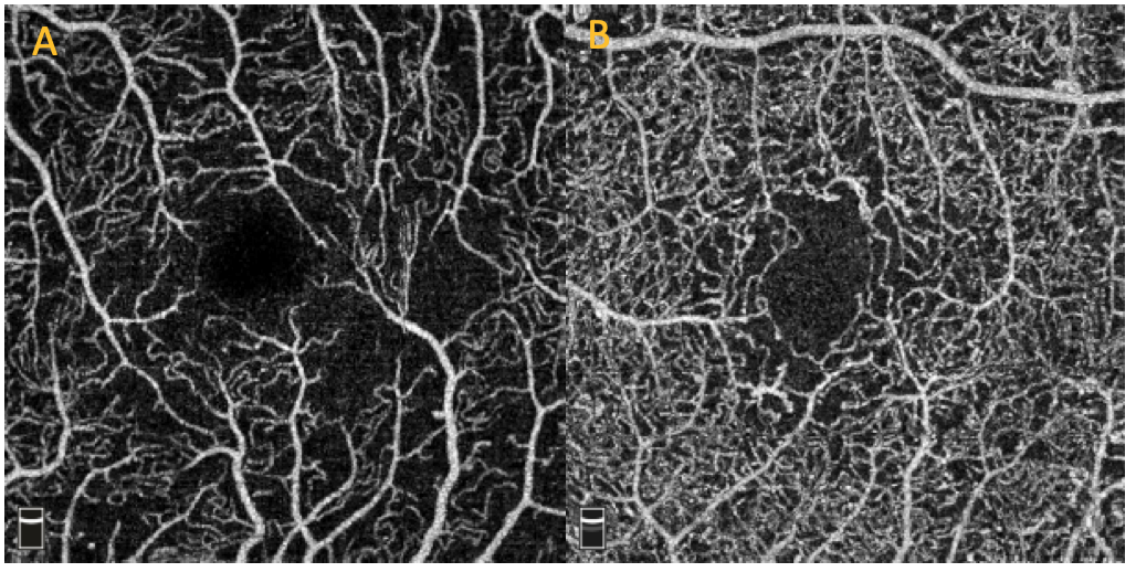

Figure 2.11: (A) OCT-A scan with low vascular density in a diabetic patient. (B) OCT-A scan showing large and irregular FAZ in a diabetic patient.

2.7 OCT-A in ocular diseases

This section summaries common applications of the OCT-A technology to ocular diseases: diabetic retinopathy, age-related macula degeneration, and glaucoma.

2.7.1 Diabetes and diabetic retinopathy

Diabetes mellitus (DM) is a systemic disease caused by unbalanced levels of sugar (glucose) in the blood. It can be distinguished in type I, where the cells that produce insulin are attacked and destroyed by the individual immune system, and type II, where there is insufficient production of insulin or the body is not effectively using it. A long-term complication of high level of glucose in the blood includes macrovascular and microvascular damage which can lead to cardiovascular diseases, kidney disease, ocular diseases, and neuropathies.
Diabetic retinopathy (DR) is the most common complication of DM and a leading cause of blindness in working-age adults worldwide [1]. It is estimated that approximately 80% of patients with diabetes mellitus develop DR after 15 years [1]. Chronic unbalanced sugar can weaken blood vessels in the retina causing leakage of blood or fluids, cotton wool spots, and aneurysms. According to the type of lesions, DR is classified following the Early Treatment of Diabetic Retinopathy Study (ETDRS) guidelines [46] into two major forms: nonproliferative and proliferative (see figure 2.12).

- Nonproliferative DR (NPDR) is characterised by white patches along the retina called cotton wool spots, intraretinal hemorrhages, microaneurysms, and occluded/tortuous vessels. NPDR can be further classified into mild, moderate, severe, and very severe categories. According to this classification, follow-up visits and treatments approaches are evaluated to reduce the risk of progression to proliferative retinopathy.
- Proliferative DR (PDR) is characterised by the formation of new blood vessels growing from the existing vascular plexus and the optic disc. Consequences of this neovascularisation are retinal detachment and vitreous hemorrhage. The severity of PDR can be stratified in early, high risk, and severe. Untreated PDR results in a progressive increase in the risk of severe vision loss.

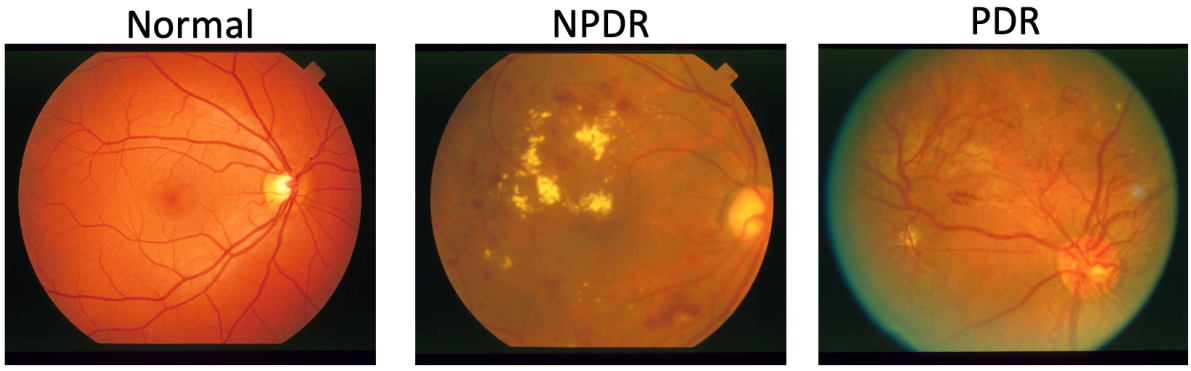

Figure 2.12: Examples of fundus photography in a normal, NPDR, and PDR patients. Images are part of the STARE dataset [9].

DR is diagnosed by visual inspection of the retina to identify lesions in the eye. However, the majority of patients with DR do not experience visual problems until later stages of the disease. Consequentially, by the time of diagnosis, damage to the retina has already occurred. There is no cure for DR, and current treatments can only slow down disease progression. Therefore, the development of retinal biomarkers for early detection of DR can help in targeting patients who would benefit from preventative therapies and monitoring disease progression. Studies have suggested that early constant features in DR patients are capillary pericytes loss and endothelial cell degeneration within retinal capillaries [47]. These changes are associated with impaired or absent perfusion. The diminished oxygen and nutrients transport causes an upregulation of angiogenic signalling molecules, such as VEGF, which increases the vascular permeability and, in the late stage of DR, promotes neovascularisation. OCT-A has emerged as the ideal retinal imaging device to extract candidate biomarkers for its ability to visualise the microvasculature in the eye in a fast and efficient way. Despite the fact that OCT-A is a recent technology and its potential in DR has not fully-explored, its ability of capturing retinal vasculature with high resolution makes this device an ideal modality for the detection and monitoring of DR progression.

Preliminary studies have already reported the potential of OCT-A in showing microvascular changes in diabetic patients. Alibhai *et al.* (2019) [48] have reported an increase in FAZ area, perimeter, and major and minor axis lengths, when comparing healthy subjects with DR participants. Hwang *et al.* (2016) [49] found reduced perivascular

and paravascular vessel density, and an increase of avascular zones in participants with DR. Kim *et al.* (2016) [50] showed a negative correlation between severity of DR and VD, skeleton density, and fractal dimension, and a positive association with vessel diameter index. Krawitz *et al.* (2017) [36] observed significant differences in acircularity index between healthy participants and diabetic subjects without retinopathy (NoDR), and axis ratio between healthy and both NoDR and DR. Takase *et al.* (2015) [51] confirmed the enlargement of the FAZ in diabetic patients independent from the presence of retinopathy, suggesting that vascular alterations can be detected before DR develops. Finally, Nesper *et al.* (2017) [41] reported associations between VD, FAZ area, and percentage area of nonperfusion (PAN) with DR severity, and PAN and adjusted flow index between healthy and NoDR, suggesting those metrics as candidate indicators of early diabetic retinopathy. Figure 2.13 shows examples of OCT-A scans in healthy, NoDR, and DR participants.

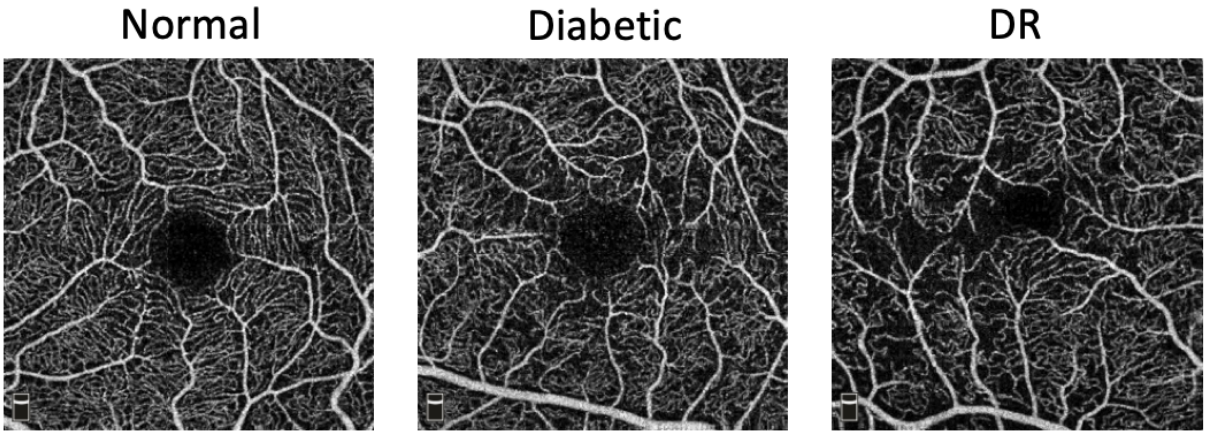

Figure 2.13: Examples of OCT-A scan in a normal, NoDR, and DR patients.

2.7.2 Age-related macula degeneration (AMD)

Age-related macula degeneration describes the impairment or loss of vision in the central part of the retina (macula) that typically affects people of age over 60. Its aetiology is not well understood, however, common risk factors include smoking, high blood pressure, and obesity. AMD can be marked as dry (nonexudative) or wet (exudative). Dry form accounts for the 80% of subjects with AMD and is characterised by drusen, macula thinning, and loss of photoreceptors. It can slowly progress to wet AMD, where new vessels form from blood leakages. This type of AMD can cause abrupt damage to vision

and lead to blindness. Current investigations are focusing on the early identification of choroidal neovascularization (CNV) to slow down disease progression and prevent vision loss. OCT-A offers the opportunity to visualise the choroidal layer and observe vascular alterations leading to vision impairment (figure 2.14). It has been used by Toto *et al.* (2016) [52] to investigate dry AMD. The authors found a significant reduction in choroidal thickness and superficial and deep retinal vessel densities between patients with AMD and healthy controls. Miere *et al.* (2015) [53] used OCT-A to capture images of patients with wet AMD to classify structural vessel patterns in CNV lesions. Their results suggested that OCT-A technology has the potential of detecting CNV lesions before other retinal devices such as OCT and FA where scarring appears as a hyperreflective lesion. Future investigations using OCT-A examining the history, progression, and response to treatment in AMD may help to gain a better understanding of the pathogenesis of this disease and improve patient outcomes.

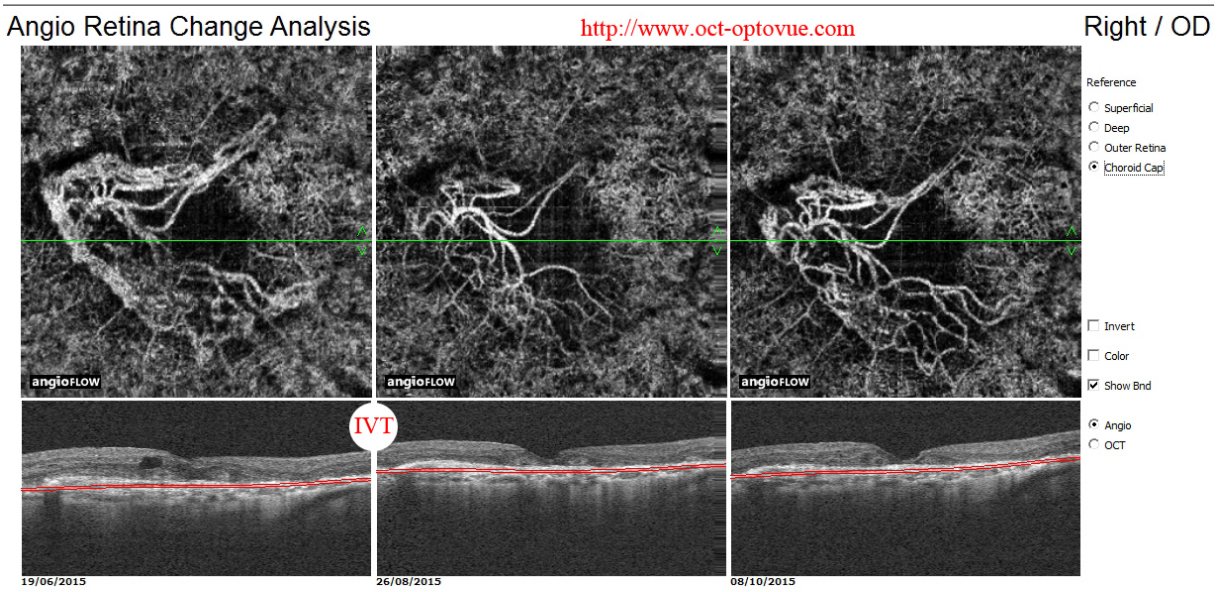

Figure 2.14: CNV detection using Angiovue OCT-A system (Image from [54]).

2.7.3 Glaucoma

The term glaucoma indicates a group of conditions characterised by a progressive damage to the optic nerve. It is a leading cause of blindness worldwide and a cure is not available yet. As with diabetic retinopathy, visual symptoms manifest when the condition is

advanced. Early diagnosis can help to prevent or slow down the disease progression and vision loss. Even though the pathogenesis is not well understood, the majority of patients suffering from optic neuropathy are characterised by high intraocular pressure (IOP) known as open angle glaucoma (OAG). However, flow impairment in the optic nerve head (ONH) and in the retinal nerve fibre layer (RNFL) can play a crucial role in glaucoma progression, especially in patients with normal IOP, known as normal-tension glaucoma (NTG). Damage to the optic nerve can progressively affect the vascular network in the retina. OCT-A gives the opportunity to visualise both the optic nerve head (ONH) and the vasculature at the center of the retina. Lévêque *et al.* (2016) [55] investigations showed a 20–25% reduction in VD in ONH in glaucomatous patients with respect to controls. ONH vessel density reduction was found also by Bojikian *et al.* (2016) [56] in OAG, and NTG when compared to healthy patients. However, there was no difference between IOP and NTG groups. More recently, Cheng *et al.* (2021) [57] investigated changes in the perifoveal vasculature at the center of the retina. The authors reported a decrease of VD and a lower multispectral fractal dimension (MSFD) in NTG subjects, highlighting OCT-A potential for early diagnosis and monitoring disease progression in different types of glaucoma.

2.8 OCT-A in neurodegenerative diseases

Recent studies have proposed the retinal landscape as a source of biomarkers for neurodegenerative disease [4]. Indeed, the eyes are part of the central nervous system and the retina is a developmental outgrowth of the brain. Consequentially, changes in the eye may reflect changes in the brain. OCT-A technology, capturing the smallest capillaries in the retinal plexuses and the optic nerve, has emerged as imaging modality to also investigate neurodegenerative disease.

2.8.1 Small vessel disease, stroke, and dementia

Small vessel disease (SVD) is a heterogeneous group of conditions characterised by the progressive decline of brain function. Cerebral SVD is common in older adults and causes a wide range of clinical symptoms, including 25% of ischemic strokes, 80% of intracerebral hemorrhages, and contributes to up to 50% of dementias worldwide [58], [59]. Changes in

the brain structure and function are thought to occur years before clinical symptoms manifest, meaning that this disease may remain undiagnosed for decades. Therefore, the investigation of structural biomarkers of brain changes in middle-aged people is a promising approach to evaluate the risks of future diseases or aid early diagnosis and targeted interventions. Moreover, neurological assessments, which are undertaken late in the disease course, can be very demanding for patients (i.e., measuring biomarkers in cerebral spinal fluid) and involve expensive healthcare examinations, such as MRI and PET scans. Retinal imaging offers the possibility for studying SVD using fast and non-invasive imaging devices, less costly diagnosis procedures, and the opportunity for earlier and more regular patient monitoring. Recent studies on participants with Alzheimer's disease (AD) have shown promising results using OCT-A retinal imaging. Yoon *et al.* (2019) [60] reported significantly reduced macular VD compared to mild cognitive impairment subjects and controls. Rifai *et al.* (2021) [61] showed an increase in FAZ area and a significant decrease in VD in patients with AD. Zhang *et al.* (2020) [62] investigated OCT-A measurements in two groups of participants with two types of stroke reporting a reduction in VD in the deep layer of the retina and a significant low FD in the large-artery atherosclerosis group compares to healthy controls. Although those OCT-A metrics may be considered as candidate biomarkers for SVD, further investigations are needed to demonstrate their potential in clinical applications.

2.8.2 Multiple sclerosis

Multiple sclerosis (MS) is a neuredegenerative and neuroinflammatory disorder that can cause visual impairments and physical disabilities. OCT retinal imaging has become part of a range of the MS diagnostic tools for its ability to assess retinal layer thickness which has been reported as a candidate marker of neuronal loss [63]. Since MS symptoms involve also damages to the optic nerve, recent studies have investigated how OCT-A can contribute to the diagnosis and monitoring disease progression. Feucht *et al.* (2019) [64] found VD of SCP and DCP scans were positively associated with thickness of the retina layers. Patients with MS and optic neuritis history (ONH) had reduced VD compared to healthy subjects. An increase of VD in the choroidal layer was associated to recent inflammatory diseases. Wang *et al.* (2014) [65] found a reduced FI in the MS group

compared to the healthy controls. Abnormal FI was detected in the group of MS with ONH, suggesting this metric as a possible candidate biomarker to identify damages to the optic nerve. Future investigations may open the opportunity for the development of novel OCT-A biomarkers able to characterise MS and different optic nerve disorders since OCT-A offers advantageous insights into the evaluation of blood flow in the optic nerve and in the retina layers.

2.9 OCT-A in systemic diseases

Systemic diseases are conditions that affect different parts of the body. The eyes share similar structural characteristics and physiological pathways of other organs. Therefore, symptoms due to diseases affecting other anatomical regions can also manifest indirectly as ocular dysfunctions. The section that follows examines systemic diseases with a retinal vascular footprint that have been investigated using OCT-A imaging.

2.9.1 Chronic kidney disease

The kidney and the eye are remarkably similar. The structure of the microvasculature in the glomerulus resembles the extensive capillary beds in the choroid, the filtration barrier in the kidney shares similar developmental pathways of the retina, and kidney and eye employ the same physiological mechanisms (*i.e.*, renin–angiotensin–aldosterone hormonal cascade) [2]. Moreover, metabolic and vascular risk factors, such as hypertension, diabetes, and smoking play a crucial role in both ocular and kidney diseases. Consequentially, diseases of the two organs are closely linked.

Chronic kidney disease (CKD) is a condition that describes the progressive reduction of kidney function. It can lead to end-stage renal disease (ESRD) where a lifetime of dialysis or a kidney transplant are the only treatments. The pathogenesis of kidney impairment is still under investigation. Evidence suggests that microvasculature alterations are a possible cause of renal dysfunction [66]. Compromised blood flow can arise from systemic inflammation, unbalance in angiogenic growth factors, and dysfunction of the glomerular endothelial cells. This can promote vessel rarefaction which increases haemodynamic dysfunction and renal ischaemia leading to kidney scarring and progressing to ESRD.

Since the close connection between these two organs, retinal microvascular changes have been previously associated with renal dysfunction. Vadalà *et al.* (2019) [67] showed choroidal thinning and lower VD in the central region of the retina in participants with CKD. Similar results were reported by Yeung *et al.* (2019) [68] which found lower VD in both SCP and DCP OCT-A scans, and by Wu *et al.* (2020) [69] reporting a reduction in retinal thickness and VD. These studies show the potential of OCT-A as a promising technology to investigate CKD and retinal microvascular changes which might reflect underlying mechanisms of inflammation, endothelial dysfunction, and disruption of renal blood flow affecting kidney function.

2.9.2 Cardiovascular diseases

Cardiovascular disease (CVD) is a group of conditions that affect the heart or the cardiovascular system. It is one of the leading causes of mortality worldwide [70]. Common CVD biomarkers such as blood pressure, cholesterol, serum creatine, and albuminuria, are not sufficiently specific to stratify and monitor CVD progression. Change in the microvasculature is a common characteristic of CVD, and retinal imaging offers a unique opportunity to visualise the cardiovascular system in *vivo*. Previous studies have predominantly used fundus photography, however, OCT-A opens the possibility to study CVD at the microvasculature level. Wang *et al.* (2019) [71] reported a reduction of VD and FI in SCP, DCP, and choroidal OCT-A scans in patients with coronary heart disease compared to healthy controls. Arnould *et al.* (2018) [72] found associations between VD measured on OCT-A and cardiovascular risk profile, and VD and the impaired left ventricular ejection fraction. Clinical translation of OCT-A retinal measurements in CVD is still, however, poorly investigated. These studies are a first step towards the development of retinal features that can offer a better understanding of microvascular changes and cardiovascular risk assessments.

2.9.3 Hypertension

Hypertension is a condition that describes persistent elevated blood pressure. If left untreated, it can cause microvascular damage, stroke, aneurysms, heart failure, and dementia [73]. Considering the effects on the microvasculature, recent studies have used

OCT-A technology to investigate this condition. Sun *et al.* (2020) [74] reported associations of hypertension with reduction of VD and enlargement of the FAZ. Similar results have been shown by Lee *et al.* (2019) [75], where a decrease in VD and an increase of FAZ areas in chronic hypertension and relieved hypertensive retinopathy groups were reported compared to healthy controls. These studies suggest that the effects of hypertension on the microvasculature can be captured using retinal imaging and OCT-A has the potential to be the optimal device for monitoring disease progression.

2.9.4 Artery and vein occlusions

Central retinal artery occlusion (RAO) and central retinal vein occlusion (RVO) represent obstructions to the blood flow in the eye. By decreasing or cutting off the blood supplies, the retinal tissue and the optic nerve will suffer from nutrients and oxygen deprivation which may lead to damage in the eye and possibly to vision loss. They typically affect people suffering from hypertension, glaucoma, high cholesterol, or cardiovascular diseases. FA is the gold standard imaging modality to assess RAO and RVO, however, it can be an invasive procedure (it requires the injection of fluorescent dye) and generate not clear images of the FAZ region and deeper retinal layers crucial for their prognostic values. Recent studies have highlighted the advantages of using OCT-A technology instead. Since based on the movement of the erythrocytes and volumetric data, OCT-A can easily visualise ischaemic regions at different depths in the retina.

To date, a limited number of OCT-A studies have investigated these two conditions. Qualitative research on patients with central RAO confirmed the potential of OCT-A to monitor changes in vascular flow as an alternative to FA [76], [77]. Quantitative investigations on patients with RVOs have reported vascular changes more prominent in the DCP layer, including a reduction in foveal and parafoveal vessel density [78].

2.10 OCT-A predictive models

Most of the clinical studies involving the use of OCT-A imaging investigate associations of retinal measurements with diseases applying multivariate analysis or statistical tests. Some more recent investigations have employed OCT-A imaging to build machine

learning models able to identify disease status among different groups of participants. Aslam *et al.* (2020) [79] considered only one eye of 182 participants to discriminate between control, NoDR, DR. Using FAZ circularity, average area of the avascular zones in the foveal region, average percentage of skeletonised capillary vessels, mean capillary intensity, and mean vessel intensity, a logistic regression model was used to distinguish healthy subjects from diseased patients achieving area under the curve (AUC) score of 0.91. Whereas a random forest classifier was used to discriminate diabetic patients without retinopathy (NoDR) from DR patients, reaching area under the curve (AUC) equal to 0.80. Alam *et al.* (2020) [80] used a support vector machine (SVM) classifier to discriminate control participants from NoDR group. Both eyes were included in the model based on five features, vessel tortuosity, vascular caliber, vessel perimeter index, vessel density, FAZ area, and FAZ contour irregularity. The final model achieved 0.92 in AUC. A similar score was obtained using the same model for the classification of healthy controls and mild nonproliferative DR (NPDR). The same AUC score is achieved by Sandhu *et al.* (2018) [81] which used local vessel density on the SCP and DCP scans, vessel calibre, and FAZ area to train an SVM classifier to identify disease stage of 106 participants with and without DR. Finally, a deep learning model was used by Lee *et al.* (2019) [75] to classify control, NoDR, and DR participants. A transfer learning (TL) approach based on VGG16 neural network architecture is used to train the classifier which achieved almost AUC = 0.96 [82]. A summary of the studies with details about OCT-A devices and performances can be found in table 2.2.

Studies	OCT-A device	Groups	Number of participants	Number of features	Model	Performance (AUC)
Aslam *et al.* (2020) [79]	DRI-OCT Triton	Healthy vs Diabetic	49/103	5	Random Forest	0.80
Aslam *et al.* (2020) [79]	DRI-OCT Triton	NoDR vs DR	50/53	5	Logistic regression	0.91
Alam *et al.* (2020) [80]	RTVue XR Avanti	Healthy vs NoDR	20/60	6	SVM	0.92
Alam *et al.* (2020) [80]	RTVue XR Avanti	Healthy vs mild NPDR	20/20	6	SVM	0.92
Sandhu *et al.* (2018) [81]	CIRRUS ZEISS	NoDR vs mild NPDR	23/83	4	SVM	0.92
Le *et al.* (2020) [82]	RTVue XR Avanti	Healthy vs NoDR vs DR	32/24/75	-	VGG16 +TL	0.96

Table 2.2: Studies using OCT-A imaging for disease prediction.

2.11 OCT-A: clinical translation

This chapter introduced the main retinal imaging modalities with particular emphasis on the OCT-A system technology. A summary of common OCT-A retinal measurements is presented along with their possible applications in clinical diagnostics on multiple ocular and systemic diseases. Finally, recent studies using machine learning models to predict patient status based on the extraction of retinal vascular phenotypes from OCT-A images were reviewed. Future directions towards predictive models on large cohorts of patients imaged with OCT-A technology will allow early detection of disease, stratification of patients according to disease severity, tracking disease progression, and customised treatments to achieve precision medicine (see figure 2.15).

Despite the potential of OCT-A imaging, there are still barriers to the clinical translation of this technology. The incompatibility regarding metrics computed on different OCT-A devices and the lack of a standard method to analyse OCT-A images are still open problems in OCT-A-based research. Other concerns arise from the small set of retinal measurements used to characterise the vasculature in the eye which may not be sufficient to cover the full spectrum of structural and functional retinal biomarkers required to reach precision medicine. This thesis tackles some of these issues. The next chapter addresses the problem of standardisation of the OCT-A image processing (chapter 3), whereas chapter 4 proposes a network-based framework for the analysis of OCT-A images with the introduction of novel retinal metrics to increase the current limited number of retinal phenotypes.

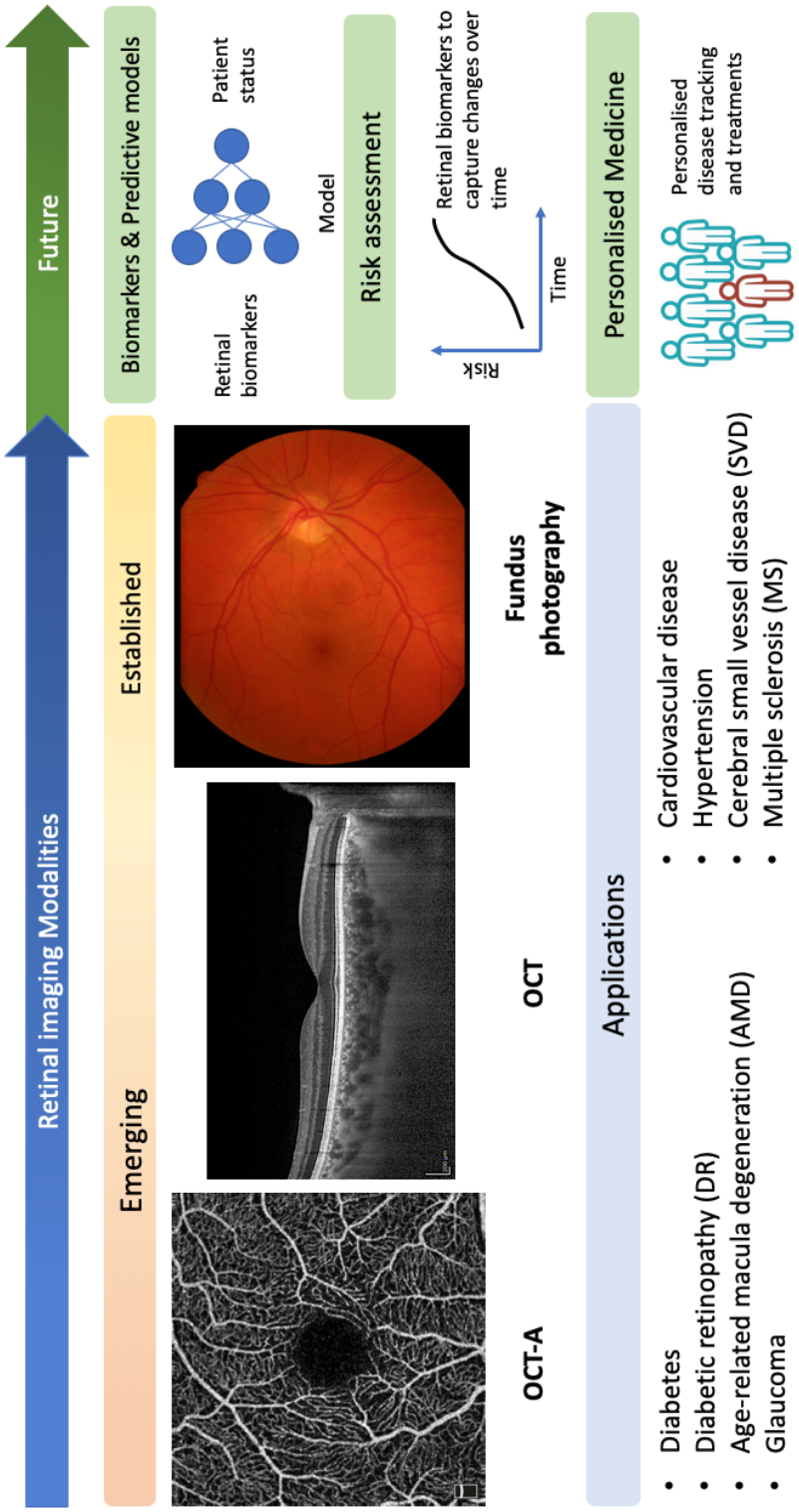

Figure 2.15: Overview of chapter 2.

Chapter 3

Image Processing and OCT-A image segmentation

3.1 Retinal image segmentation

The term segmentation refers to the process involving the grouping of pixels making up different objects in an image. In retinal imaging, it can be interpreted as the identification of pixels representing either the vasculature or the background tissue (e.g., in fundus photography and OCT-A scans) but also as the detection of the different layers making up the retina volumes (e.g., in OCT scan figure 3.1). Segmentation is a crucial step in the image processing pipeline since the accuracy and reliability of candidate biomarkers for ocular and systemic diseases are based on the segmented image obtained after the processing of the retina scan. Manual segmentation of blood vessels is a time-consuming procedure and prone to operators' subjectivity. Hence, the necessity of establishing an automated method that provides objectivity in repeatability and reproducibility.

OCT-A is a fairly recent technology and the application of customised and automated segmentation algorithms is still under investigation. Despite the fact that many segmentation approaches have been developed for medical images, no single method is suitable for different anatomical regions or imaging modalities. Therefore, after providing an overview of the state-of-the-art in blood vessel segmentation and OCT-A, the investigation of the application of different vessel segmentation approaches on OCT-A images with the aim of establishing a standard approach for this recent technology is presented. Contributions of this chapter include i) the first comparison of a large set of

state-of-the-art vessel segmentation methodologies (including handcrafted filters and deep learning approaches) to assess the best method in OCT-A imaging; ii) the creation of the first open OCT-A image dataset with manually segmented scans (OCTA-RSS); iii) the implementation of novel segmentation evaluation metrics that take into account similarities not only in pixels but also in vascular structures; iv) finally, the source code openly available to support standardisation efforts.

This work has been published in Translational Vision Science & Technology [5].

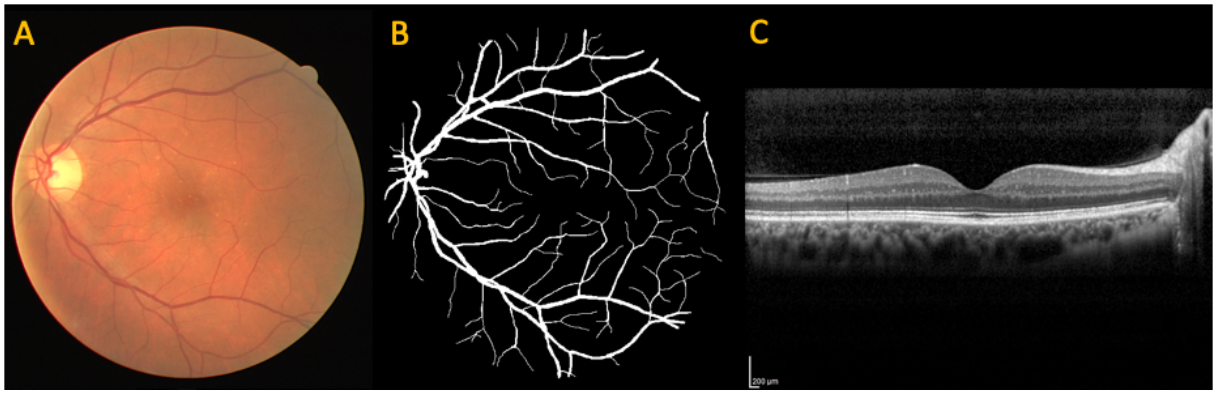

Figure 3.1: (A) Fundus photograghy scan and its segmentation (B) from DRIVE dataset [8]. (C) OCT scan.

3.2 Retinal blood vessel segmentations

Blood vessel segmentation is a procedure that is applied to several medical domains, from cardiology to ophthalmology. However, there is no segmentation approach suitable for any medical device or anatomical region. Briefly, an overview of the main steps to segment retinal blood vessels is provided. The whole segmentation pipeline can be divided into four steps as shown in the diagram in figure 3.2 (blue boxes).

The first step involves preliminary pre-processing procedures such as the adjustment of colour, contrast, and noise reduction. The core of the segmentation pipeline is, however, the second step, *i.e.,* the vessel enhancement. Several approaches have been developed to highlight the vasculature in medical imaging and these approaches can be grouped into four categories:

- *handcrafted filters* are hand-designed structures that enhance the vessel perception by increasing the contrast between the vessel and the background tissue;

- *machine learning methods* learn how to enhance the vessel structure using training examples;
- *deformable models* exploit geometric and topological properties of curves or surfaces in the image domain to highlight vessel structures;
- *tracking approaches* consist of a growth process where the starting points are randomly chosen in the image.

More details on the most common handcrafted filters and machine learning methods will be presented in section 3.5. Deformable and tracking approaches are not part of this investigation, however, further details can be found in [83].
After vessel enhancement, the binarisation step is performed by applying a threshold to the intensity values of the enhanced image. Finally, post-processing procedures can be applied to remove small disconnected vessels which may be caused by noise or errors in the segmentation.

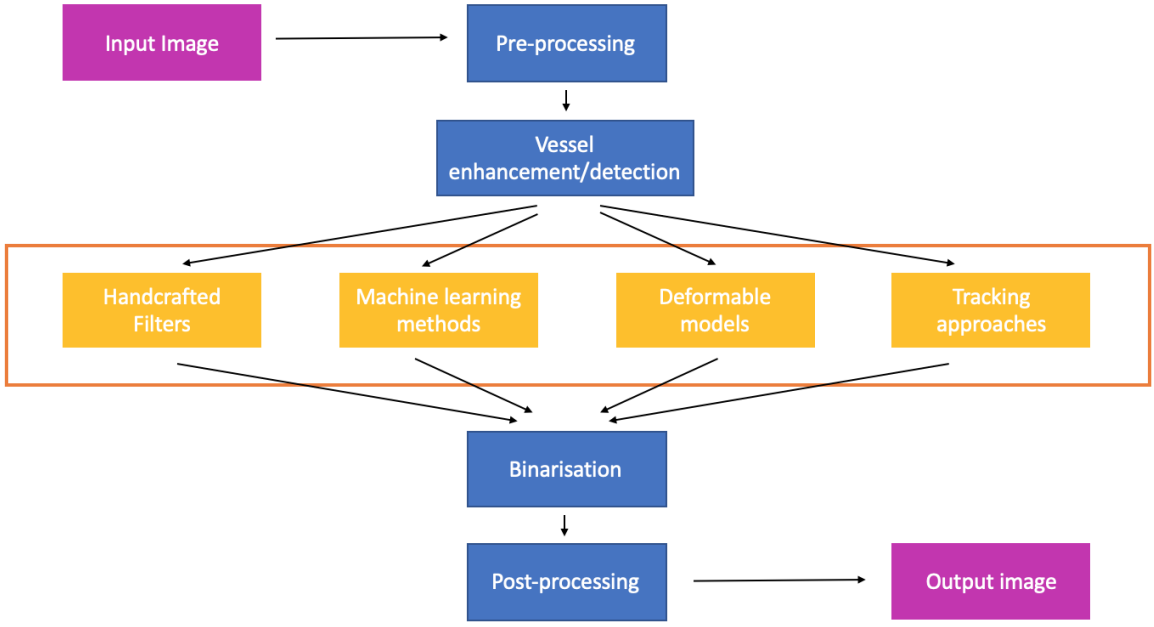

Figure 3.2: Flow chart of blood vessel segmentation pipeline.

3.3 OCT-A segmentation in clinical studies

Clinical studies have been using OCT-A images since the early development of this technology, mainly focusing on the extraction of imaging markers to guide early diagnosis of systemic disease. Segmentation approaches have been based on simplistic pipelines (*e.g.*, global thresholding) or on the most popular methods for anatomical region segmentation (*e.g.*, hessian filters). More recently, new studies on customised and automated OCT-A segmentation approaches have started to emerge. This section summarises segmentation methods used in clinical publications and more recent investigations aimed to propose new OCT-A segmentation approaches.

OCT-A segmentations The majority of OCT-A clinical studies relies on the extraction of retinal measurements from manually traced vessels in a particular region of interest in the OCT-A scans, i.e., the foveal avascular zone. These studies include Alibhai *et al.* (2019) [48], Krawitz *et al.* (2017) [36], De Carlo *et al.* (2015) [84], Takase *et al.* (2015) [51], and Vadalà *et al.* (2019) [67]. Other investigations led by Lee *et al.* (2019) [75] and Corvi *et al.* (2018) [23] were based on metrics computed by built-in software installed in the OCT-A devices which may differ across manufacturers. Thresholding procedures were used as segmentation step in Nesper *et al.* (2017) [41], Onishi *et al.* (2018) [43], and Hwang *et al.* (2016) [49]. Other simple approaches such as intensity contrast-based algorithm and low pass filters were used by Kashani *et al.* (2017) [85] and Reif *et al.* (2012) [86], respectively. More sophisticated approaches for vessel enhancement were used by Kim *et al.* (2016) [50] and Zhang *et al.* (2016) [87] where adaptive thresholding and Frangi filter (see 3.5.1 for details) were applied to the original scans. Other customised procedures were found in Schmidt *et al.* (2019) [88], where frame averaging was used to enhance vessels before applying Sobel filter [89], hysteresis thresholding, and opening and closing procedures for FAZ detection. In Jesus *et al.* (2019) [90], circumpapillary microvascular density was computed as a spline over the local maxima obtained from a third-order median filter of the average intensity vector. A probabilistic segmentation approach based on Markov-Gibbs random field model was proposed by Eladawi *et al.* (2017) [91] to identify retinal blood vessels from background tissue.

Finally, deep learning models were proposed to segment OCT-A images by Prentašic *et*

al. (2016) [92] using a convolutional neural network and by Mou *et al.* (2019) [93], which proposed a new type of architecture, CS-Net, to segment OCT-A retinal scans. Other deep learning approaches were published at the same time as this work by Ma *et al.* (2021) [44] and Li *et al.* (2020) [45].

3.4 Data acquisition and manual segmentation

To assess the best segmentation method for OCT-A images, a ground truth dataset with manually segmented images is required as a benchmark to compare the different approaches. Initial 17 healthy volunteers of the PREVENT study [94] underwent eye examination using the commercial RTVue-XR Avanti OCT system (OptoVue, Fremont, CA). Each of those images was divided into five subimages, one from each clinical region of interest (ROI) according to the *Early Treatment of Diabetic Retinopathy Study (ETDRS)* [46]: superior, nasal, inferior, temporal, and foveal (3.3A). Poor quality ROIs were discarded and the remaining 55 ROIs (belonging to 11 participants) were split into training (30 ROIs) and test (25 ROIs).

3.4.1 OCT-A Retinal Scans and Segmentations (OCTA-RSS): a publicly available open dataset

Manual segmentation is a time-consuming procedure and, in OCT-A images, a highly challenging task. Motions artifacts can arise from unstable scan acquisitions. Moreover, images can suffer from poor contrast, low signal-to-noise ratio, and quilted defects. Vertical and horizontal line distortions are the most common artifacts, as shown in figure 3.3B, and the smallest capillaries are challenging to segment and therefore are affected by subjective interpretation. In previous studies proposing OCT-A segmentation methods, ground truth images were generated by manually continuous delineation of vessels with or without consideration of vessel width ([92] and [93], respectively). This approach can lead to an overinterpretation of vessel connectivity and loss of important clinical information enclosed in the vessel calibre. In this work, a more conservative approach was adopted by performing pixelwise manual segmentation. The entire set of images was segmented by a single rater (Ylenia Giarratano), using ITK-SNAP software [95].

Segmentations were reviewed by an ophthalmologist in training (Eleonora Bianchi), who also performed manual segmentation of a subset of images to assess the repeatability of the process. Intra- and iter-rater variability measurements were computed to assess the degree of agreement in manually segmented images obtained by the two different operators and twice by the same operator. Only images of the superficial capillary plexus with 3×3 mm^2 FOV were included in dataset. Original OCT-A ROIs and ground truth images were collected and published as an open OCT-A dataset (`https://doi.org/10.7488/ds/2729`).

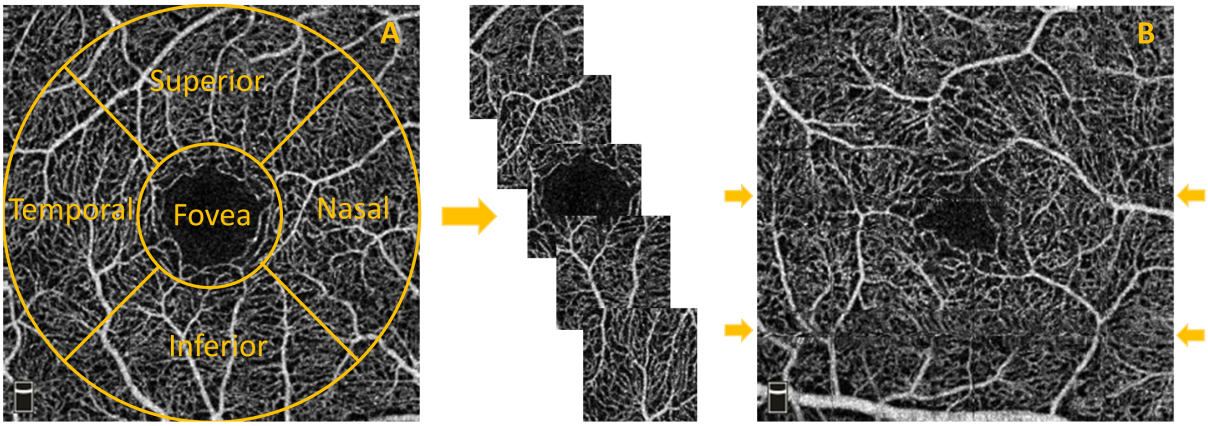

Figure 3.3: (A) Extraction of images from each clinical region of interest: superior, nasal, foveal, inferior, and temporal. (B) Examples (arrows) of horizontal artifacts in OCTA images. Note: reprinted Copyright 2020 Giarratano *et al.* tvst.arvojournals.org [5].

3.5 Vessel segmentation approaches

This section presents popular vessel enhancement methods, handcrafted filters and deep learning architectures, and the binarisation procedure used for the assessment of the best segmentation approach for retinal OCT-A images.

3.5.1 Handcrafted Filters

Frangi filter is a multiscale vessel enhancement filtering method introduced by Frangi *et al.* in 1998 [96]. It is obtained by computing a *vesselness* measure using the eigenvalues of the second-order local structure (i.e., the hessian) of the image of interest. The eigenvalues of the Hessian matrix describe local geometric properties of the surface giving information

about the curvature of the vessel. Briefly, given a vessel scale s, the vesselness measurement, V_o, in a 2-dimensional image, is described by the following formula

$$V_o(s) = \begin{cases} 0 & \text{if } \lambda_2 > 0 \\ \exp\left(-\frac{\lambda_1^2}{\lambda_2^2(2\beta_1^2)}\right)\left(1-\exp(-\frac{(\lambda_1^2+\lambda_2^2)}{2\beta_2^2}\right) & \text{otherwise} \end{cases}, \tag{3.1}$$

where λ_1 and λ_2 are the Hessian eigenvalues ($\lambda_1 < \lambda_2$), and β_1 and β_2 are parameters that empirically regulate the sensitivity of the measure. The final value is then obtained by taking the maximum vesselness across multiple scales,

$$V_o = \max_{s_{min} \leq s \leq s_{max}} V_o(s). \tag{3.2}$$

In this work, parameters are selected using the training set. Different combinations are explored and the set of parameters that achieves the best segmentation metric (*dice* score) is chosen. Using Frangi filter available in MATLAB R2018b (version 9.5) [97], the following configuration is selected, $\beta_1 = 1$, $\beta_2 = 15$, and $s = [0.5, 2]$.

Gabor filter Continuous wavelet transforms have been extensively applied in image processing since their ability to identify edges and texture features in images. Gabor filter is based on the Morlet wavelet (also known as Gabor wavelet), a directional wavelet able to be adjusted according to the desired frequencies to perform vessel enhancement. The implementation of this filter follows the one proposed by Soares *et al.* [98]. Let $f \in L^2$ (the space of square integrable functions) be the image defined in $\mathbb{R}^2$. The continuous wavelet transform $T_\psi(b, \theta, a)$ is defined as:

$$T_\psi(b, \theta, a) = {C_\psi}^{-1/2} \frac{1}{a} \int \psi^*(a^{-1} r_{-\theta}(x-b)) f(x) d^2x, \tag{3.3}$$

where $C_\psi, \psi, \psi^*, b, \theta$, and a, are the normalising constant, the Morlet wavelet, the complex conjugate of the Morlet wavelet, the displacement vector, the rotation angle, and the scale, respectively. In particular the Morlet wavelet is a complex esponential modulated Gaussian, defined as

$$\psi(x) = exp(ik_0x)exp\left(-\frac{1}{2}|Ax|^2\right), \tag{3.4}$$

where j is the imaginary unit, k_0 regulates the frequency, and A is a 2×2 matrix with diagonal elements equals to $\epsilon^{-1/2}$ and 1 that controls the filter elongation. Finally, for each value of the scale, the response with maximum orientation, $M_\psi(b,a) = \max_\theta |T_\psi(b,\theta,a)|$ is chosen. In this work, parameters for this filter are the frequency $k_0 = 5$, the expected elongation $\epsilon = 2$, and the vessel scales ([0.5, 2]).

SCIRD-TS It is an adaptation of the scale and curvature-invariant ridge detector (SCIRD) filter to thin structures [99]. The general idea is to curve a ridge detector using a non linear transformation and to obtain the vessel enhancement by convoluting the image with the second derivative of the multiple curved ridge detectors (filter bank). Briefly, the straight ridge detector is obtained by computing the second derivative (in each direction and summing up all the contributions) of a multivariate zero-mean (n-dimensional) Gaussian filter,

$$G(\varphi,\sigma) = \frac{1}{\sqrt{(2n)^2\prod_{i=1}^{n}\sigma_i{}^2}} exp\left(-\sum_{i=1}^{n}\frac{\varphi_i{}^2}{2\sigma_i{}^2}\right), \tag{3.5}$$

where φ represents a point in the n-dimensional space and σ is the standard deviation. The second derivative with respect the φ_j coordinate is

$$G_{\varphi_j,\varphi_j}(\varphi,\sigma) = G(\varphi,\sigma)\left[\frac{1}{\sigma_j{}^2}\left(\frac{\varphi_i{}^2}{\sigma_i{}^2}-1\right)\right]. \tag{3.6}$$

Finally, the straight support is bent to create a curvilinear detector using the following non-linear transformation $T : \mathbb{R} \longrightarrow \mathbb{R}$ with

$$T(x) = \varphi = (\varphi_1, \varphi_2, ..., \varphi_n),$$

where for $j = 1$, $\varphi_1 = x_1$ and for $2 \leq j \leq n$,

$$\varphi_j = x_j + \sum_{i=1}^{n-1} k_{ji}x_i{}^2. \tag{3.7}$$

Using the transformation 3.7 in a 2-D space on the equation 3.6 the SCIRD-TS filter is obtained

$$F(x,\sigma,k_{21}) = \frac{1}{\sigma^2 Z(\sigma)}\left[\frac{(x_2+k_{21}{x_1}^2)^2}{{\sigma_2}^2}-1\right]\times exp\left(-\frac{{x_1}^2}{2{\sigma_1}^2}\right)exp\left(-\frac{(x_1+k_{21}{x_1}^2)^2}{2{\sigma_2}^2}\right), \quad (3.8)$$

where k_{21} is the curvature parameter, σ_1 and σ_2 are the scales. By rotating the filter according to different angles θ, SCIRD-TS reaches the rotation invariance.

Parameters for this filter include large and small vessel scales ([1,5], [1,2], respectively), curvature range (k = [-0.1, 0.1]), rotation of the filter ($\theta = 20°$), and size of the filter (9×9).

OOF Optimally oriented flux (OOF) is a curvilinear structure detector proposed by Law and Chung (2008)[100]. OOF projects the image gradient along different directions and measures the amount going in and out a local spherical region to optimize the final direction. This procedure has the advantage of limiting the detection to a local region avoiding confusion in closely located vessels. Given a 2-dimensional images, the flux along the direction $\hat{\rho}$ flowing in or out a circle S_r of radius r can be computed as

$$f(x,\rho,r) = \hat{\rho}^T Q_{r,x}\hat{\rho}, \quad (3.9)$$

where $Q_{r,x}$ is a 2×2 matrix with i-th row and j-th column elements equal to

$$q_{r,x}^{i,j} = \int_{\partial S_r}(\nabla G * I)(x+\hat{n}r)n_j dA. \quad (3.10)$$

$\hat{n}$ is the outward unit normal and ∂S_r is the boundary of the circle. Finding the maximum projection of the gradient involves solving the eigenvalue decomposition problem for $Q_{r,x}$, where the eigenvalues extracted correspond to the values of oriented flux along the eigenvectors. This work uses the 2-D OOF implementation proposed by Li *et al.* [101]. Parameters of this filter are vessel scales ([0.5, 2]), and a blurring operator (σ = 0.5).

3.5.2 Deep learning architectures

CNN Convolutional neural networks (CNN) are deep learning architectures popular for their successful applications to many computer vision tasks [102]. These models are

characterised by successions of multiple units made of convolutional layers and maxpooling layers. The CNN designed in this work is based on the one proposed by Prentašic *et al.* [92] to segment OCT-A images. It consists of three convolutional layers with rectified linear unit activation (ReLU), each followed by maxpooling. The risk of overfitting is reduced by using dropout before the last fully connected layer. Adam optimizer and cross-entropy loss function are used to train the model. This CNN architecture is a pixelwise model, meaning that for each image in input, it classifies only the central pixel. This can lead to biased results when the number of pixels representing the vasculature and highly different from the number of pixels identified as background tissue. To overcome this unbalance, the same number of vessel and background pixels is extracted from each image along with their 61×61 neighbourhood (as in [92]) and used as input to the network (figure 3.4A). This architecture contains 663,949 trainable parameters and more than 200,000 patches are used as input during the learning phase. The output of the network is the probability of being a vessel pixel which is used to generate the enhanced grayscale image.

U-Net A more recent type of convolutional neural network, proposed by Ronneberger *et al.* [103] for biomedical image segmentation, is the U-Net. Its name derives from its U-shape obtained by the design of a contracting and an expansive path. This architecture has been proved to achieve accurate results even with small training data. In this work, the encoder (contracting) path consists of modules of two repeated convolutional layers with ReLU activation function followed by maxpooling. The deconder (expansive) path includes modules of an upsample layer and two repeated convolutional layers. The bottleneck between the two paths uses images of 8×8 pixels (figure 3.4B) leading to a total of 470,977 trainable parameters. Finally, stochastic gradient descent (SGD) and cross-entropy are used during the learning process. 1000 patches of size 32×32 are extracted from each ROI for a total of 30,000 training inputs.

CS-Net Similar to the U-Net architecture, CS-Net, proposed by Mou *et al.* [93], is also characterised by a contracting and an expansive path. Its bottleneck is characterised by the presence of two modules: the spatial and channel attention units. Spatial correlation is used in the first module to retrieve global contextual features, whereas changes in intensity

across channels are captured by the channel attention module (figure 3.4C). CS-Net implementation was available on `https://github.com/suyanzhou626/CSNet` and default settings are applied in this thesis. Adam optimizer and mean square error loss function are used during the learning phase. This architecture contains 8,400,545 trainable parameters. Training is performed using the same procedure described for U-Net.

Data augmentation (flipping horizontally or vertically) has been performed in all the three architectures and the 10% of training inputs are used as validation set.

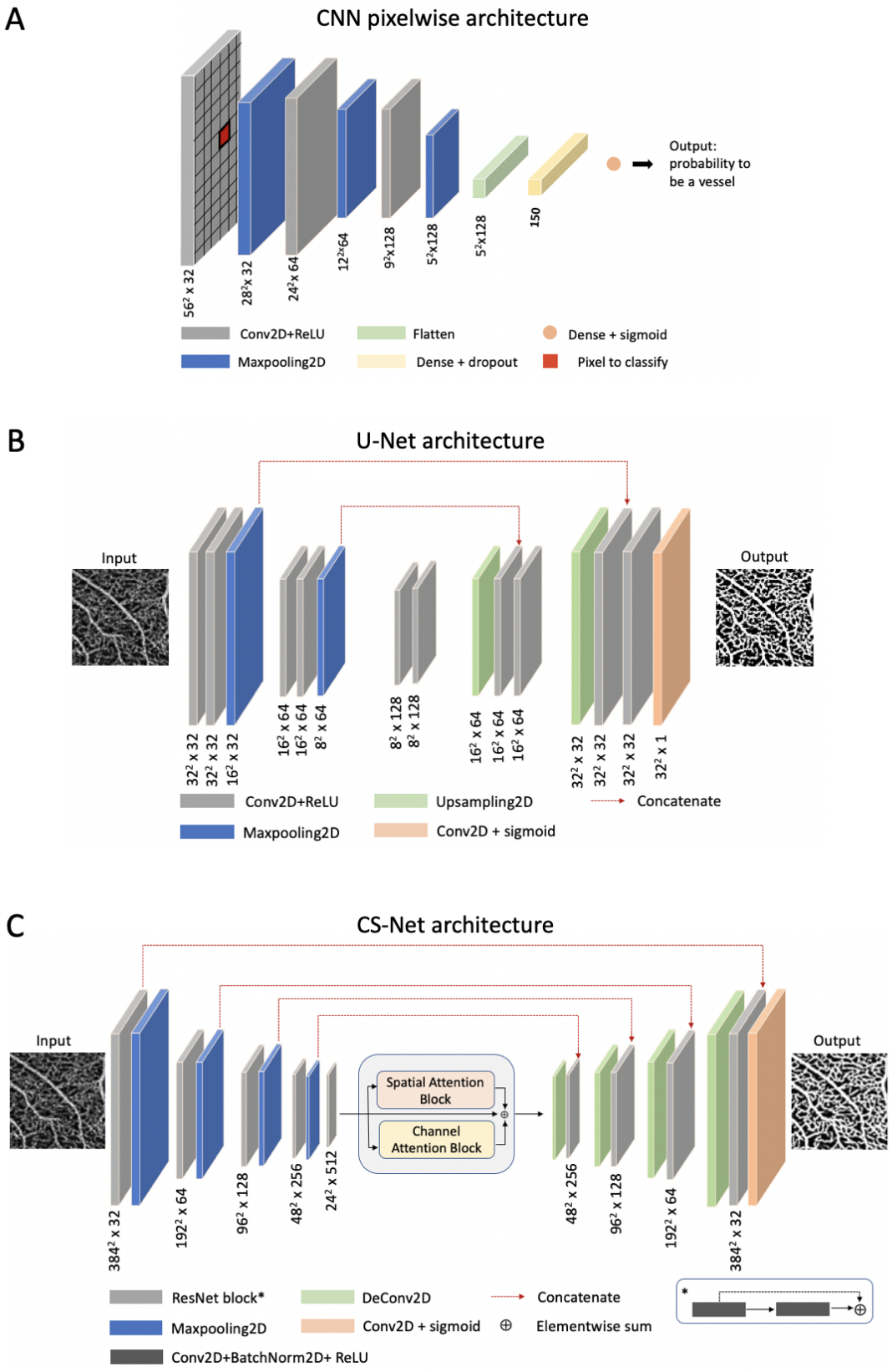

Figure 3.4: Deep learning architectures for OCT-A segmentation.

3.5.3 Binarisation procedures

After vessel enhancement, binarisation is typically achieved by global, local, or a combination of thresholds (*e.g.,* Otsu method [104]). More advanced binarisation algorithms, exploiting machine learning techniques (ML), have been also used to produce binary maps after vessel enhancement. In this work, adaptive thresholding (AT), which applies local thresholding based on spatial variations in illumination [105], is used as baseline binarisation method. AT is benchmarked against different binarisation methods based on ML algorithms such as support vector machines (SVMs), random forest (RF), and k-nearest neighbours (k-NN) to obtain the final binary mask in the case of Frangi, Gabor, SCIRD-TS. Seven features are computed to characterise each pixel in the image: intensity-based features extracted from a 3×3 pixel neighbourhood (intensity value, average, standard deviation, range, and entropy) and geometric features (the local curvature information provided by the hessian eigenvalues) as described in [106]. A double step procedure consisting of a global threshold for large vessels and AT for the small capillaries is used in the case of OOF based on Li *et al.* implementation [101]. Probability maps obtained from the CNN architecture are binarised using a global threshold based on the shape of the pixel intensity histogram. AT is applied to the output of U-Net, and the Otsu method in the case of CS-Net as described in [93]. Post-processing procedures included morphological opening, using MATLAB R2018b (version 9.5) function *bwareaopen* to remove small disconnected pixel structures possibly due to segmentation errors or noise in the image.

3.6 Segmentation evaluation

For each ROI in the test set, common pixelwise segmentation metrics such as accuracy, precision, recall are reported when segmented images are compared to the ground truth manual segmentation (further information can be found in Appendix A).

Cohen's kappa coefficient Inter- and intra-rater variability are computed to assess the quality of the manual segmentation. Cohen's kappa coefficient is a metric that reveals

agreements between operators [107]. It is computed as follow:

$$\kappa = \frac{Pr(a) - Pr(e)}{1 - Pr(e)}, \tag{3.11}$$

where $Pr(a)$ is the accuracy in pixel classification (vessel *vs* background) and $Pr(e)$ is the sum of two addends: the probability that both raters randomly select vessel pixels, and the probability of both raters randomly select background pixels.

Dice score Another reported popular pixelwise segmentation metric is the *dice* score, used to assess the similarity between two samples. Given a boolean classification, *dice* score is defined as

$$Dice = \frac{2TP}{2TP + FP + FN}, \tag{3.12}$$

where TP, FP, FN indicate true positive, false positive and false negative, respectively.

CAL Proposed by Gegundez-Arias *et al.* [108], CAL (connectivity-area-length) metric captures similarities of structural characteristics of the vasculature between pairs of images and it is used as global segmentation quality score. It is the product of three sub-metrics:

- connectivity (C), to quantify the degree of fragmentation between segmentations, and computed as

$$C(S, S_{GT}) = 1 - min\left(1, \frac{|\#_C S_{GT} - \#_C S|}{\#S_{GT}}\right), \tag{3.13}$$

  where $\#_C S$ and $\#_C S_{GT}$ are the counts of connected components in the segmented and ground truth image, while $\#S_{GT}$ is the count of vessel pixels in the mask;

- area (A), to capture the degree of overlapping between the segmented image and the ground truth mask,

$$A(S, S_{GT}) = \frac{\#((\delta_\alpha(S) \cap S_{GT}) \cup (S \cap \delta_\alpha(S_{GT}))}{\#(S \cup S_{GT})}, \tag{3.14}$$

  where δ_α is a morphological dilatation using a disc of radius α and # represents counts;

- length (L), to evaluate the degree of coincidence, computed as

$$L(S, S_{GT}) = \frac{\#((\varphi(S) \cap \delta_\beta S_{GT})) \cup (\delta_\beta(S) \cap \varphi(S_{GT}))}{\#(\varphi(S) \cup \varphi(S_{GT}))}, \tag{3.15}$$

  where φ indicates a skeletonisation procedure and δ_β is a morphological dilatation using a disc of radius β.

OCT-A images can capture extremely dense capillary networks with small vessel width. Hence, parameters of these metrics, α and β, are both set to a minimum value equal to 1. The final CAL product takes values in the range [0,1] with the zero denoting the worst segmentation and 1 the perfect segmentation.

LCC ratio Although CAL contains a connectivity component, its effect is mitigated by the area (A) and length (L) metrics. Therefore, a new metric called the largest connected component ratio (LCC) is proposed in this work to penalise methods that introduce disconnections in crucial points in the vasculature resulting in a smaller vascular network. LCC is defined as:

$$LCC = 1 - min\left(1, \frac{|\#LCC_S - \#LCC_{GT}|}{\#LCC_{GT}}\right), \tag{3.16}$$

where $\#LCC_S$ and $\#LCC_{GT}$ are the number of pixels in the skeleton of the largest connected component in the segmented and ground truth image, respectively. LCC ratio close to 1 indicates a very similar structure in the largest connected components of the two images. Using LCC ratio more information is added to the evaluation process than using the *dice* score solely: a single pixel difference does not influence *dice* score, however, it may dramatically affect the LCC ratio, changing the number of connected components.

Topological similarity score Beyond pixelwise metrics, recent studies have embedded the reconstruction of topological properties of the vascular plexus in the segmentation methods [109]. Hence, a topological evaluation metric is implemented in this study to assess the accuracy of the vascular topology after segmentation. We exploit the concept of persistent homology and Betti numbers for angiograms described in [109] (SI in appendix B). The

topological similarity score (TopS) is introduced as

$$TopS = 1 - min\left(1, \frac{|\beta_{1S} - \beta_{1GT}|}{\beta_{1GT}}\right), \tag{3.17}$$

where β_1 is the first Betti number associated with the image and representing the number of one-dimensional holes (i.e., intercapillary spaces in the vasculature), supplementary information can be find in Appendix B.

3.6.1 Clinical metrics

Since different segmentation methods may affect the computations of relevant clinical metrics, three popular OCT-A imaging measurements, i.e., vessel density, FAZ area, and FAZ acircularity index [36], [41], [43], [48], [50], [68] are computed to explore how the segmentation methods affect those measurements by calculating the relative error against ground truth values. Vessel density is obtained as the number of white pixels over the total number of pixels in the ROIs. To calculate FAZ metrics, the skeleton of the image is converted into a graph object. Then, using the doubly connected edge list (DCEL) data structure (more detail in chapter 4) which identifies all the intercapillary spaces as loops in the network, it is possible to detect the FAZ as the largest intercapillary space. Considering the points describing the FAZ contour, FAZ size is then computed measuring the area enclosed by the points at the boundary. Acircularity is computed as the ratio between FAZ perimeter and the circumference of a circle with size equal to the FAZ area. It should be noted that the algorithm employed for the detection of the FAZ requires a continuous boundary to be identified (loop), therefore an overestimation of this region is obtained in images with disconnected FAZ contour (see example in figure 3.5).

3.7 Results

3.7.1 Inter and intra-rater agreements

Images of the training and test set were segmented by only one operator (rater A, Y.G)). A subset of 20 ROIs was segmented twice by rater A to assess intra-rater reliability. A

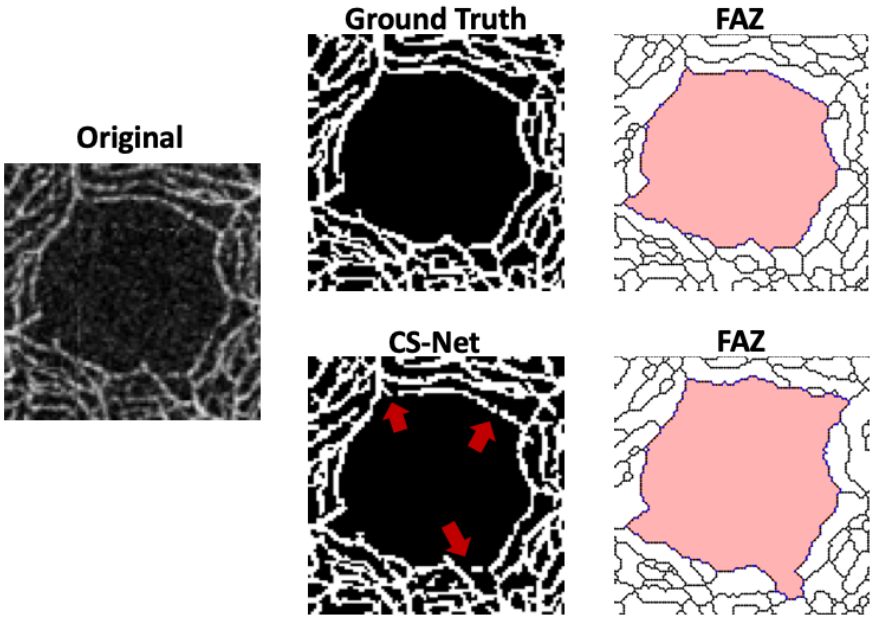

Figure 3.5: Original image, ground truth and CS-Net segmentation, and the corresponding FAZ detection (red regions).

second operator (rater , E.B.) manually segmented a subset of other 20 ROIs to compute the inter-rater agreement. Cohen's kappa coefficient was on average 0.8 for the intra-rater agreement and 0.77 for the inter-rater reliability indicating that the manual segmentation was consistent and reproducible between operators. Figure 3.6 shows an example of an image segmented twice by rater A and an image segmented by the two different operators.

3.7.2 Automated approaches for pixelwise classification

Results of vessel enhancement and binarisation procedures are shown in figures 3.7 & 3.8. Each handcrafted filter exhibits difficulties in retrieving vessels: Frangi filter clusters vessels in close proximity, grouping small capillaries in larger ones. Gabor filter enhances ridges and poorly detects vessel edges. A more regular and equally spaced vasculature can be observed after applying SCIRD-TS, suggesting remodeling of the vasculature. Finally, OOF overenhances noise in the foveal region.

Table 3.1 reports segmentation performances for each of the proposed methods. The best *dice* score (0.89) is achieved by both U-Net and CS-Net which outperform all the other

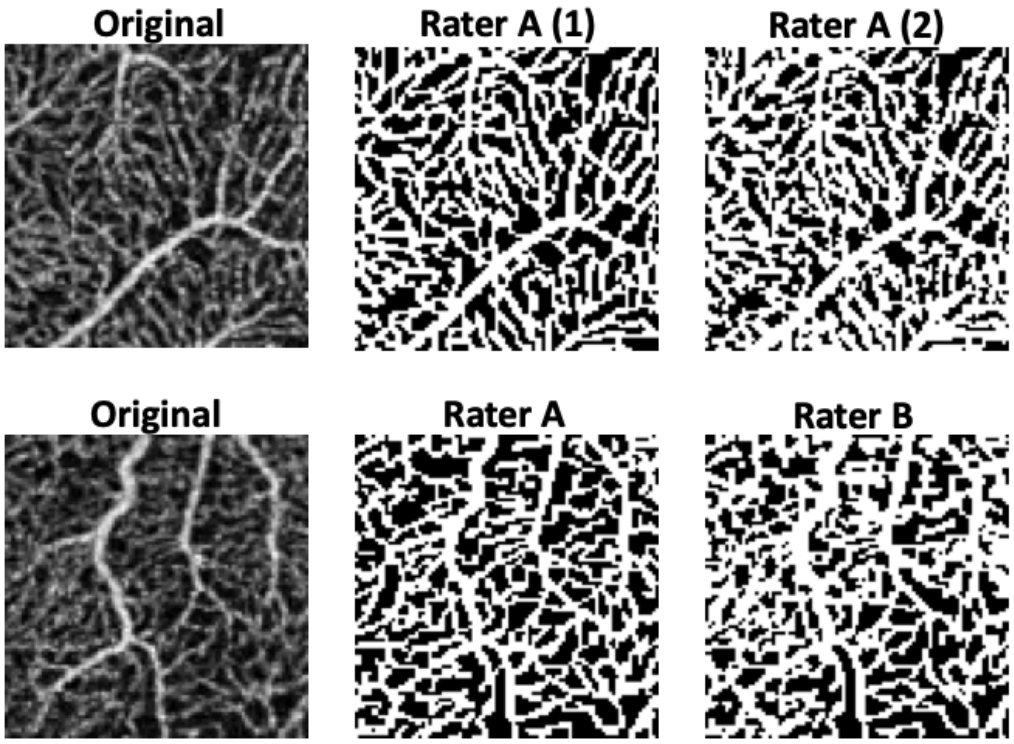

Figure 3.6: Original OCT-A ROIs with examples of two images segmented by the same rater A, and two images segmented by the two different operators (rater A and rater B).

methods. OOF and Frangi reach the best performances among the handcrafted filters with *dice* scores of 0.86 and 0.85, respectively. Adaptive thresholding, the baseline method, achieves a comparable *dice* score of the handcrafted filters, however, unlike Frangi and OOF, it achieves poor performances in retrieving network connectivity as shown by the LCC and TopS metrics. Machine learning procedures after Frangi, Gabor, and SCIRD-TS, improve both pixelwise and network structure evaluation metrics when compared to binarisation obtained by adaptive thresholding.

The highest performance in the network structure metric, LCC ratio, is achieved by deep learning architectures (CNN, 0.94, UNet and CS-Net, 0.93) together with the OOF (0.94). Finally, the best TopS score is reached by the CS-Net and OOF, 0.83 and 0.80, respectively. The same two methodologies also retrieve the most similar vessel density to the ground truth images, obtaining the lowest errors 6% and 10%.

The foveal avascular zone is a region at the center of the retina free from blood vessels.

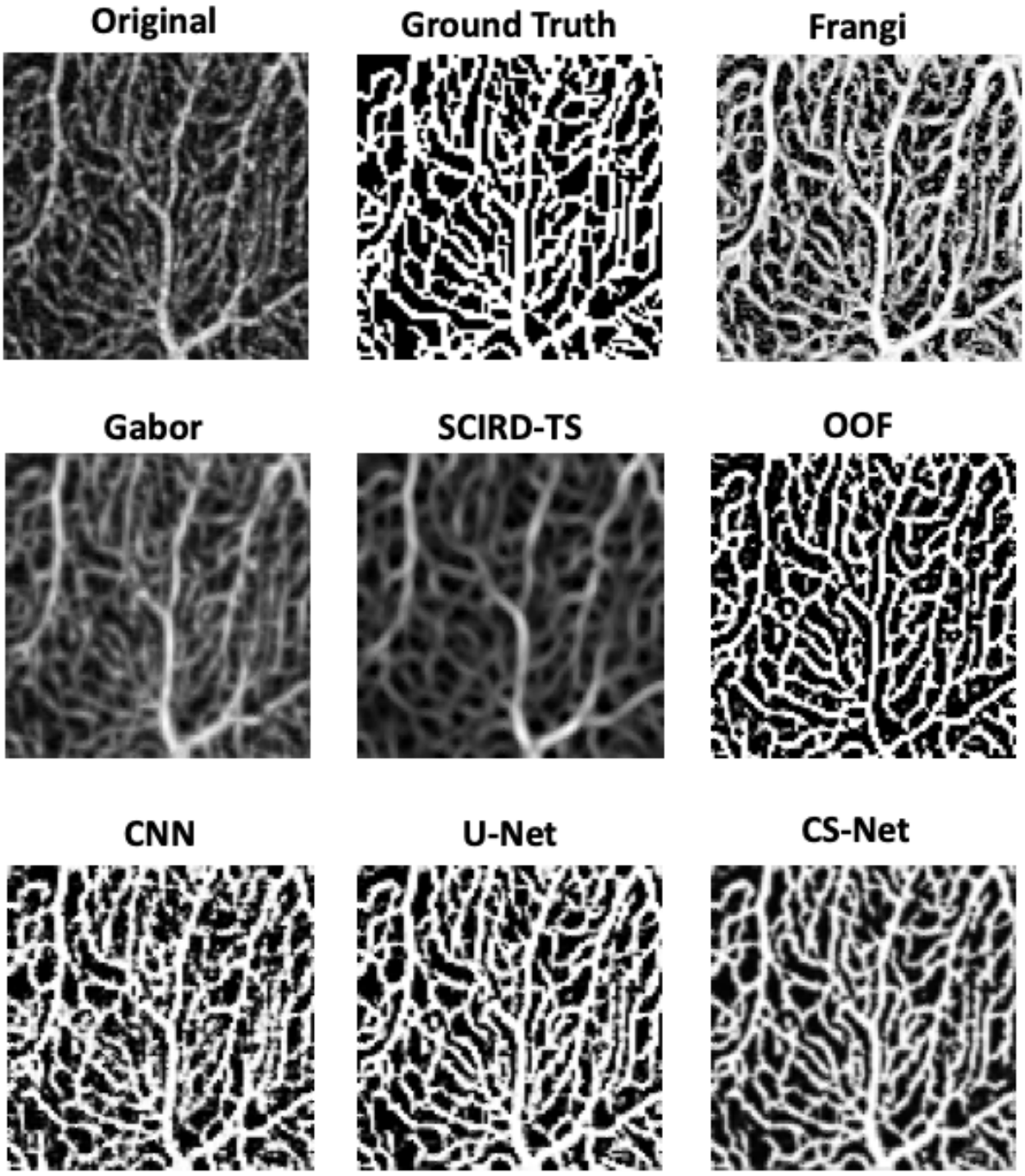

Figure 3.7: Example of vessels enhancement. Original, ground truth and images after vessel enhancement by using Frangi, Gabor, SCIRD-TS, OOF, CNN, U-Net, CS-Net. Note: reprinted Copyright 2020 Giarratano *et al.* tvst.arvojournals.org [5]

ROIs containing this region are more difficult to segment by the handcrafted filters that can overenhance noise and detect vessels at the center of this region. Machine learning

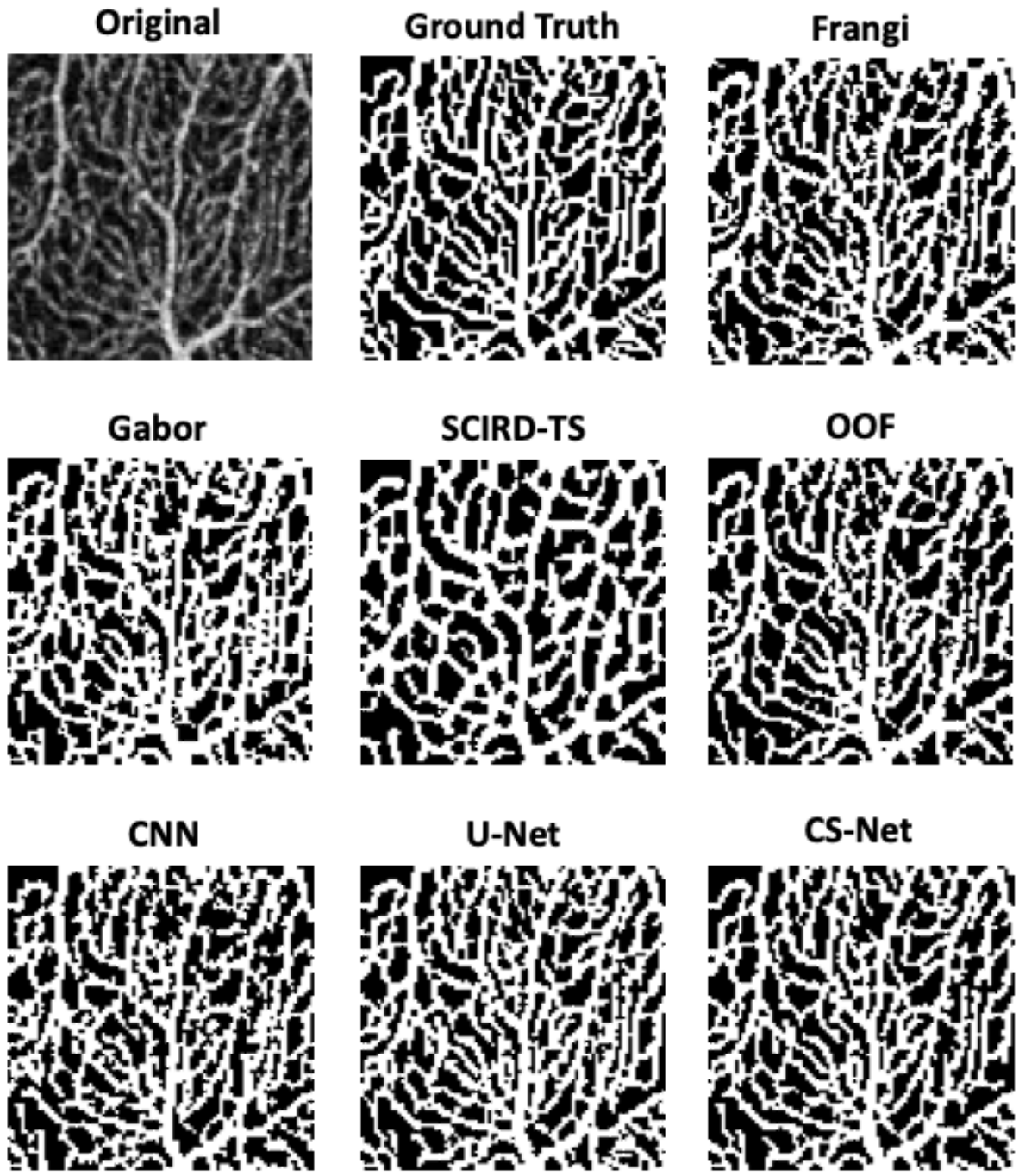

Figure 3.8: Vessel segmentation in superior parafoveal OCTA image. Original, ground truth images followed by binary images after vessel enhancement by using Frangi (+RF), Gabor (+RF), SCIRD-TS (+SVM), OOF, CNN, U-Net, and CS-Net. Note: reprinted Copyright 2020 Giarratano *et al.* tvst.arvojournals.org [5]

methods are less affected by this issue since they use ground truth images during the learning process. Figure 3.9A shows segmentation results in the foveal region after

Method	Dice	Acc	Rec	Pre	CAL	LCC	TopS	VD
Adaptive thres (AT)	0.86	0.89	0.89	0.92	0.83	0.83	0.70	14%
Frangi+AT	0.83	0.86	0.83	0.93	0.83	0.88	0.72	21%
Gabor+AT	0.77	0.81	0.78	0.87	0.75	0.76	0.59	24%
SCIRD-TS+AT	0.71	0.76	0.74	0.82	0.66	0.68	0.46	25%
OOF	0.86	0.88	0.87	0.92	0.85	**0.94**	0.80	10%
Frangi+k-NN	0.84	0.87	0.85	0.91	0.86	0.91	0.59	14%
Frangi+SVM	0.85	0.88	0.85	0.93	0.87	0.94	0.76	15%
Frangi+RF	0.85	0.88	0.86	0.92	0.87	0.94	0.75	13%
Gabor+k-NN	0.82	0.84	0.80	0.92	0.84	0.84	0.37	21%
Gabor+SVM	0.83	0.85	0.78	0.94	0.85	0.84	0.45	24%
Gabor+RF	0.83	0.85	0.80	0.93	0.85	0.87	0.45	22%
SCIRD-TS+k-NN	0.72	0.77	0.76	0.82	0.74	0.90	0.35	19%
SCIRD-TS+SVM	0.75	0.79	0.78	0.84	0.75	0.75	0.54	19%
SCIRD-TS+RF	0.74	0.78	0.77	0.83	0.75	0.80	0.65	19%
CNN	0.83	0.86	0.85	0.91	0.85	**0.94**	0.70	14%
U-Net	**0.89**	**0.91**	0.87	**0.97**	**0.90**	0.93	0.67	17%
CS-Net	**0.89**	**0.91**	**0.91**	0.93	**0.90**	0.93	**0.83**	**6%**

Table 3.1: Segmentation performances (best method per column in bold.)

applying each vessel enhancement method. Furthermore, segmentation performances across the 5 different ROIs are investigated. Results in table 3.2 shows consistently lower *dice score* in the foveal region except for CS-Net. Visual inspection of OCT-A segmentations shows that disconnections at the boundary of the FAZ can dramatically affect FAZ detection, leading to important errors in FAZ area (FazE) and acircularity index (AIE) (figure 3.9B).

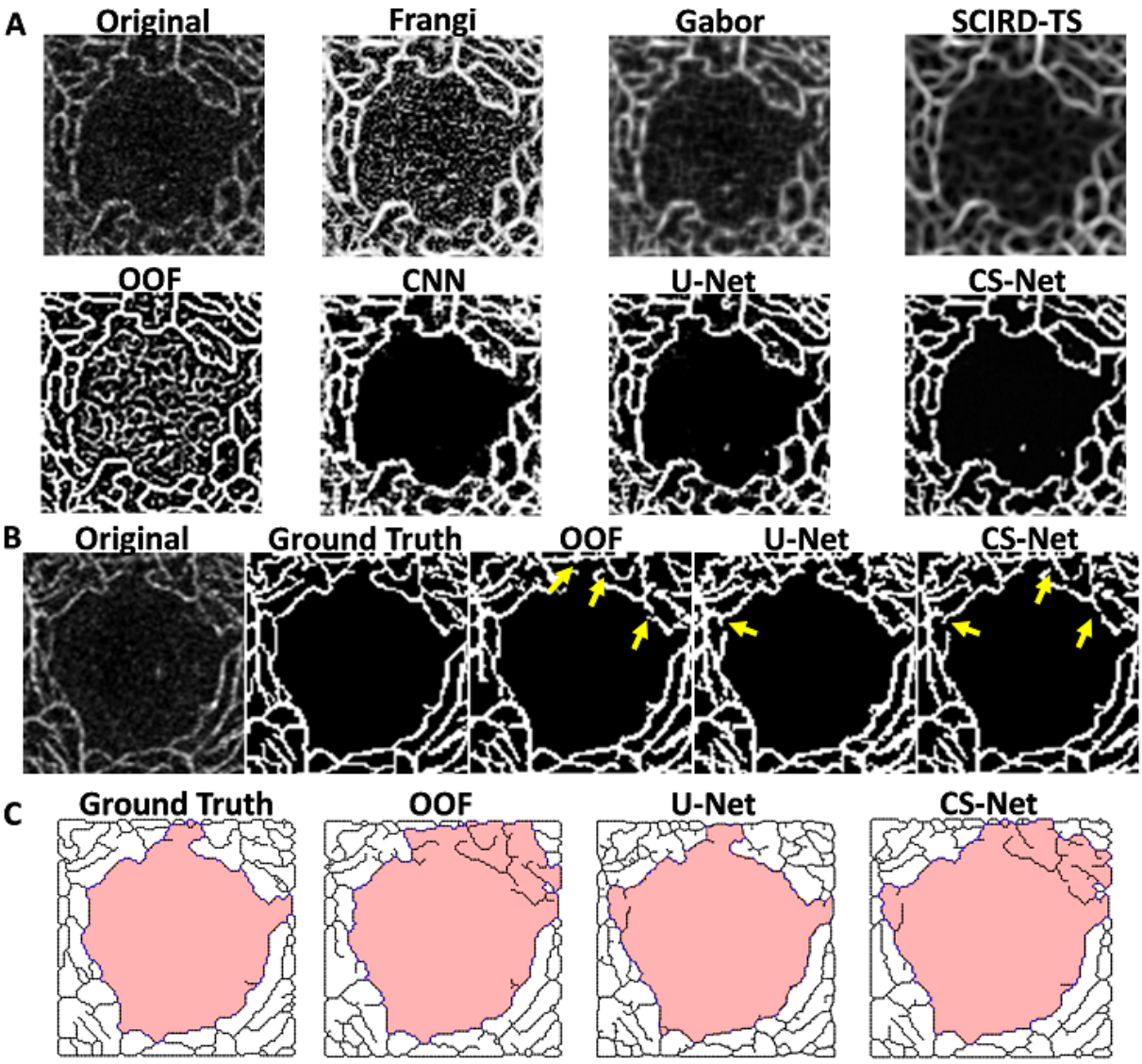

Figure 3.9: Foveal images. (A) Enhancement in the foveal avascular zone. (B) Foveal regions after binarisation: disconnections (yellow arrow) in OOF, U-Net, and CS-Net.(C) Different FAZ detections (red) due to disconnections in the binarisation. Note: reprinted Copyright 2020 Giarratano *et al.* tvst.arvojournals.org [5].

3.8 Discussion

The reliability of clinical metrics and the reproducibility of OCT-A studies crucially rely on the quality of the image segmentation. This chapter has extensively investigated how different automated blood vessel segmentation methods compared to each other when applied to OCT-A images. To benchmark the different methods, the first publicly available open dataset of retinal OCT-A images with ground truth manual segmentations

Method	F	S	N	I	T	FazE	AIE
Adaptive thres (AT)	0.84	0.87	0.88	0.88	0.86	14%	5%
Frangi + AT	0.79	0.86	0.86	0.85	0.85	12%	9%
Gabor + AT	0.75	0.78	0.80	0.75	0.77	13%	10%
SCIRD-TS + AT	0.71	0.73	0.75	0.67	0.71	14%	7%
OOF	0.84	0.86	0.88	0.86	0.85	24%	11%
CNN	0.82	0.84	0.85	0.84	0.83	6%	6%
U-Net	0.87	0.90	0.90	0.90	0.89	**5%**	**4%**
CS-Net	0.89	0.89	0.90	0.89	0.88	14%	5%

Table 3.2: Dice score per ROI (superior (S), nasal (N), inferior (I), temporal (T), and foveal (F)) and FAZ error metrics

(OCTA-RSS) was generated, and the assessment of segmentation quality was evaluated by computing intra- and inter-rater variability. Along with common performance metrics for segmentation, two novel evaluation metrics were introduced to assess the preservation of the network structure (LCC and TopS). These results suggested CS-Net is the best method for OCT-A image segmentation achieving the highest scores in almost all evaluation metrics. U-Net also achieved very competitive performances compared to CS-Net, reaching the lowest errors in FAZ clinical metrics. Among the methods that do not require manually segmented images for training purposes, the OOF reached segmentation performances comparable to the deep learning architectures. Examples of binarisation using the best three segmentation methods on a $3 \times 3\ mm^2$ OCT-A scan is shown in figure 3.10.

This work highlights how segmentation methods can affect clinically relevant metrics extracted from OCT-A images: up to 25% differences in vessel density, and up to 24% difference in FAZ area. These results suggest to pay special attention to the image processing pipeline when comparing results of different studies or reproduce meta-analysis. Limitations of this work included the use of images acquired by a single OCT-A device, the small number of images, and the use of only scans of the superficial capillary plexus. Moreover, OCT-A scans were acquired from volunteers with healthy retinal vasculature while pathological vessels may require additional investigations.

Future works will involve the use of machine learning models to improve poor quality OCT-A images and the assessment of the robustness of the results of this study across OCT-A devices from multiple manufacturers.

After image segmentation, the next chapter moves on to consider the development of the network-based framework for the extraction of microvascular phenotypes from OCT-A retinal images.

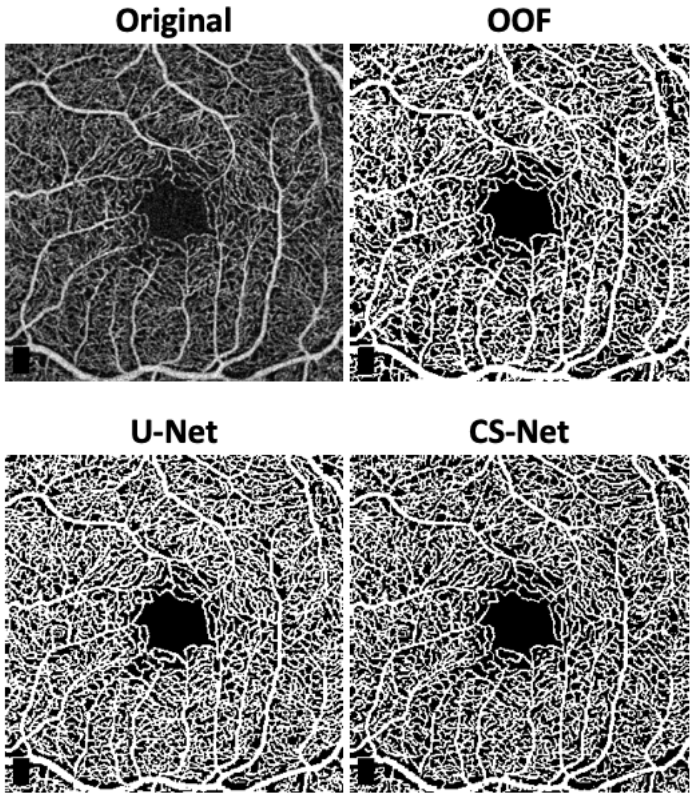

Figure 3.10: Whole image segmentation by using the best three methods, OOF, U-Net, and CS-Net. Optovue RTVue XR Avanti scan logo on the bottom left corner was removed from the original image. Note: reprinted from [5] Copyright 2020 Giarratano *et al.* tvst.arvojournals.org

3.9 Source code and data availability

OCTA-Retinal Scan and Segmentations (OCTA-RSS) dataset is available at `https://doi.org/10.7488/ds/2729`. Handcrafted filters were implemented in MATLAB R2018b (Version 9.5). ML methods were written in Python 3.6.9. CNN and U-Net were implemented in Python using Keras library with Tensorflow backend. CS-Net was

available at `https://github.com/suyanzhou626/CSNet`. Persistent homology library (Gudhi) was used to compute the topological metric [110]. Source code is available at `https://github.com/giaylenia/OCTA_segm_study`.

Chapter 4

Network analysis framework

This chapter describes the OCT-A network analysis framework developed for the extraction of retinal microvascular phenotypes. This represents the second step of the computational pipeline following the OCT-A vascular segmentation previously described. After a first introduction discussing the motivations behind the use of a network analysis approach, the implementation of the framework for the modeling of the microvasculature is presented along with the computations of known and novel vascular metrics based on functional and structural properties of the retinal plexus. Finally, a step forward towards the standardisation of these measurements is reported by investigating the robustness of the developed retinal metrics by analysing their reproducibility across repeated OCT-A scans acquired at three different time points during the same day.

This chapter contributes to the advance of retinal imaging by proposing a novel methodology to investigate OCT-A scans. An automated computational framework is developed to characterise vascular networks, and novel metrics are implemented to capture the wide spectrum of candidate retinal biomarkers. It assumed the reader is familiar with basic concepts of graph theory; if not, please consult Easley *et al.* (2010) [111]. A description of this framework has been published by Springer International Publishing as proceeding of the 7th MICCAI Workshop on Ophthalmic Medical Image Analysis (OMIA7) [6] [1].

[1]The OCT-A network analysis framework has been developed in collaboration with two MSc students at the School of Informatics of the University of Edinburgh, Ian Maudin, Rowan Sudgen, Alisa Pavel and Jie Lian. Students have carried out the implementation of various vascular functions such as graph simplifications and retinal metrics (*e.g.*, tortuosity, graphlets, and random walks).

4.1 Network analysis and vascular networks

Network analysis is part of the mathematical field that defines properties and applications of graphs, also known as *graph theory*. It represents a heterogeneous group of methods widely used to describe technology, internet, transportation, power grids, but also nature and biology, such as water distribution, protein-protein interactions, and neuronal connections [112], [113]. Briefly, a graph is described as a mathematical object $G = (V, E)$, where V is the set of vertices (*nodes*) representing the entities in the system, and E is defined as the set of links (*edges*) connecting two nodes (*endpoints*) and describing the interactions in G. A *directed graph* is represented with directional edges which define an order in the relationship between vertices, whereas a *undirected graph* is characterised by non-oriented edges describing an unordered interaction between nodes. Graphs that can be embedded into a plane without edges crossing each other (i.e., edges intersect only at endpoints) are called *planar* (figure 4.1). The application of network analysis to several technological and scientific disciplines was popularised thanks to the works of Watts and Strogatz [114], and Barabási and Albert [115] which promoted the representation of complex systems as entities (nodes) interacting with each other (edges). For example, in the modern hyper-connected era, the World Wide Web can be represented as a graph where nodes are web pages and hyperlinks are edges; in neuroscience, nodes represent different parts of the brain, and edges describe structural or functional interactions between cerebral regions; in epidemics, the spread of a disease depends not only of the pathogen and its contagiousness but also on the interactions in the population which can be modeled using *contact networks* where a person is represented as a node and an edge is drawn if two people come into contact with each other. Further examples can be found in Easley *et al.* (2010) [111]. Since the ability to characterise systems with entities moving along paths (water, energy, etc..), network analysis has been also used to investigate blood vessels as erythrocytes moving along the vasculature. This work takes advantage of network analysis to create planar undirected graphs that represent the retinal vascular plexus and extract measurements that capture vessel characteristics. The representation of the vasculature using a graph object allows the characterisation of the structural and functional properties of the network, providing a unique way to extract information from the retinal vascular system.

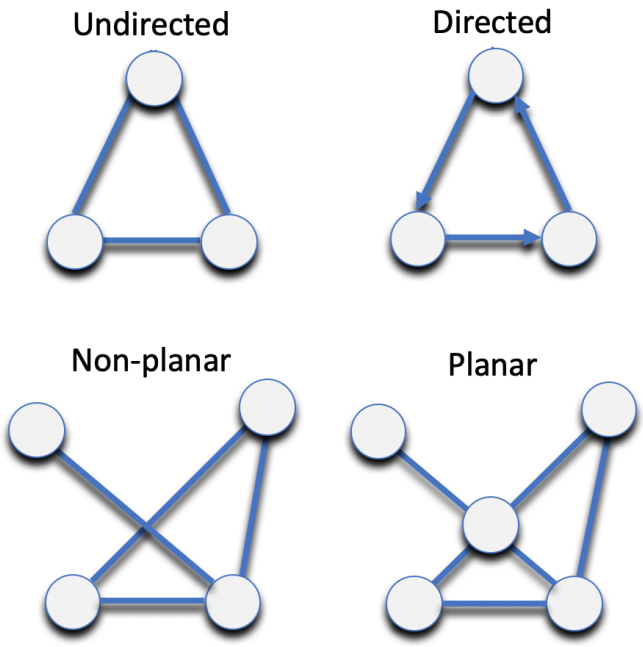

Figure 4.1: Examples of undirected, directed, non-planar, and planar graphs.

4.2 OCT-A and vascular network construction

After vessel segmentation (more details in chapter 3), the binary image is skeletonised using the *bwskel* function in the *image processing toolbox* in Matlab2020b [116]. The retinal vascular network is constructed by using customised functions able to model the microvasculature captured in OCT-A images. Considering the skeletonised image, S, of $n \times n$ pixels, for each row i and column j, the element $s_{ij} \in \{0,1\}$ is associated to the coordinates (i,j). Vertices of the graph are then found as coordinates of the white pixels of the skeletonised image. Each vertex is associated with the radius of the vessel segment at that pixel point. Radius is computed using the distance (in pixels) of the vertex to the nearest background pixel in the original binary image. To construct edges, a customised function (*find_edges*) is implemented to analyse the local region of size 2×2 surrounding each white pixel in the skeleton, and draw connections to vertices in the same neighborhood. This approach leads, in particular pixel configurations, to an overconnected network not representative of the original topological structure (as shown

in figure 4.2A&B). To overcome this issue, when multiple links are possible, the approach prioritises vertical and horizontal connections (figure 4.2 C). This procedure allows us to find edges that preserve the morphological structure of the network avoiding overconnectivity. Finally, using the original pixel size (*pixelPerUm*), the set of nodes, edges, and radii, are embedded into a Euclidean space where original distances are preserved. An overview of the procedure is shown in algorithm 1 which describes an extension to OCT-A images of the approach developed by Lu *et al.* (2017) [117] to analyse the mouse retina. The network stored in a *VTK Polygonal Data* (vtp extension), a format readable in a user-friendly interface software, *ParaView* [118], contains nodes with two attributes, coordinates and radius, and edges with other two attributes, length, computed as Euclidean distance between endpoints, and radius, calculated as the average of the radii of the endpoints. This vascular graph is the input of the network analysis framework written in python using the network analysis library *netxworkx* [119].

Algorithm 1 Graph Construction

```
1: function SKELETONIZETIFFPLEXUSOCTA(pixelPerUm, fileName, image)
2:     skeleton = bwskel(image)                          ▷ Compute skeleton
3:     vertices = find(skeleton>0)                       ▷ Extract non-zero pixels
4:     edges = find_edges(skeleton, vertices)            ▷ Compute edges
5:     plexusBoundary = bwboundaries(image)              ▷ Identify vessel boundaries
6:     radius = find_radius(image, plexusBoundary, vertices);   ▷ Compute radius
7:     VTP_writer(vertices, edges, radius, pixelPerUm, fileName)
```

4.3 Graph simplifications

The framework converts each white pixel in the skeleton into a vertex in the network. Consequentially, the retinal graph contains a large number of non-essential nodes (*e.g.*, vertices making up a straight vessel), affecting the computational cost of many of the vascular metrics. Therefore, different simplifications of the same network are generated with the aim of reducing the computational time in the calculation of several retinal measurements.

Simplification by the largest connected component The vascular plexus captured in OCT-A images can have few disconnected components due to either image quality issues

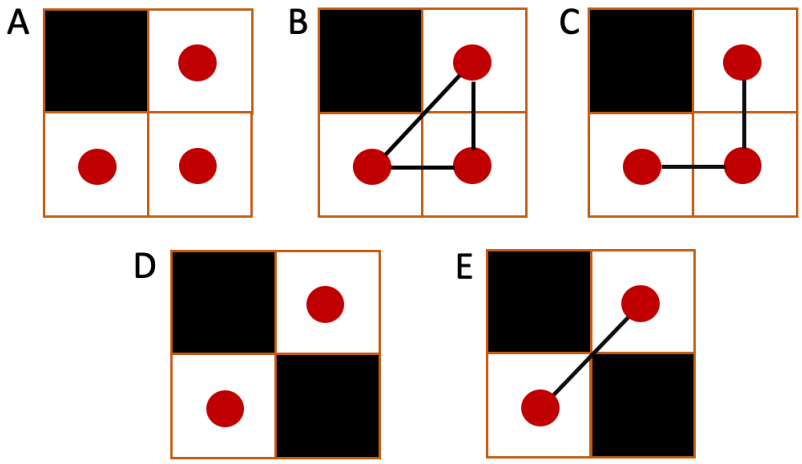

Figure 4.2: Example of connections in the network. Vertices representing white pixels are drawn in red. (A) Example of problematic configuration. (B) All possible edges between two vertices. (C) Output from the algorithm (D) Example of diagonal link. (E) Edges generated by the algorithm.

or errors introduced during the segmentation procedure. The simplification by the largest connected component discards disconnected parts from the network and retrieves the component with the largest number of nodes with degree three (branching points). This simplification is used to compute metrics that require a continuous path in the network (*e.g.,* average path length in the graph). An example of a vascular network simplified by the largest connected components is shown in figure 4.3C.

Simplification by angle Considering the large number of nodes can slow down computations, the simplification by angle removes a node of degree two if the angle between its two outgoing edges does not fall into a customisable range (180 - tolerance, 180 + tolerance). The default value of the tolerance is zero, *i.e,* nodes of degree two are removed when the node is on a straight line (figure 4.3D).

Simplification by degree The simplification by degree removes all the nodes of degree two, leaving the vascular network with only leaf nodes and branching points (figure 4.3E). Information about geometric characteristics of the vasculature is discarded and the vasculature can appear slightly different from the original network. This simplification is used to investigate topological characteristics of the network where information about

structural properties is not required. By removing nodes of degree 2, which consist of the majority of vertices in the network, the final representation is simplified to fewer nodes and edges. This will speed up computations of metrics that traverse the entire network and visit each vertex. An overview of the implementation is shown in algorithm 2.

Simplification by loop Loops in the network represent the intercapillary spaces of the retinal plexus. This simplification removes all leaf nodes and disconnected components to retrieve only the loopy structure of the network to provide information about intercapillary spaces distribution, network nestedness, and complexity (figure 4.3F).

4.4 Regions of interest in the graph

This framework is customised only for OCT-A images of 3×3 mm^2 field of view (but it can be generalised to 6×6 mm^2 scans). The captured retinal plexus can be divided into different regions of interest (ROIs). The foveal region is described by a circle centered at the foveal pit with diameter equal to one millimeter. The parafovea is the external annulus with three millimeters in diameter. Finally, the perifoveal region is the part of the macula outside the parafovea. The region enclosed in the parafoveal ring can be further divided into four parts: nasal (N), inferior (I), temporal (T), and superior (S) as shown in figure 4.4B.

Algorithm 2 Simplify vascular network

```
1: procedure SIMPLIFYGRAPHBYANGLE(G, tolerance)
2:     nodes = get_nodes(G)
3:     for node in nodes do
4:         if degree(node) is 2 then
5:             n1, n2 = get_neighbours(node)
6:             if angle((n1, node), (node, n2)) is less than tolerance then
7:                 remove_node(G, node)
8:                 new_edge = edge(n1, n2)
9:                 add_attribute(new_edge, distance(n1, n2), mean_radius(n1, n2))
```

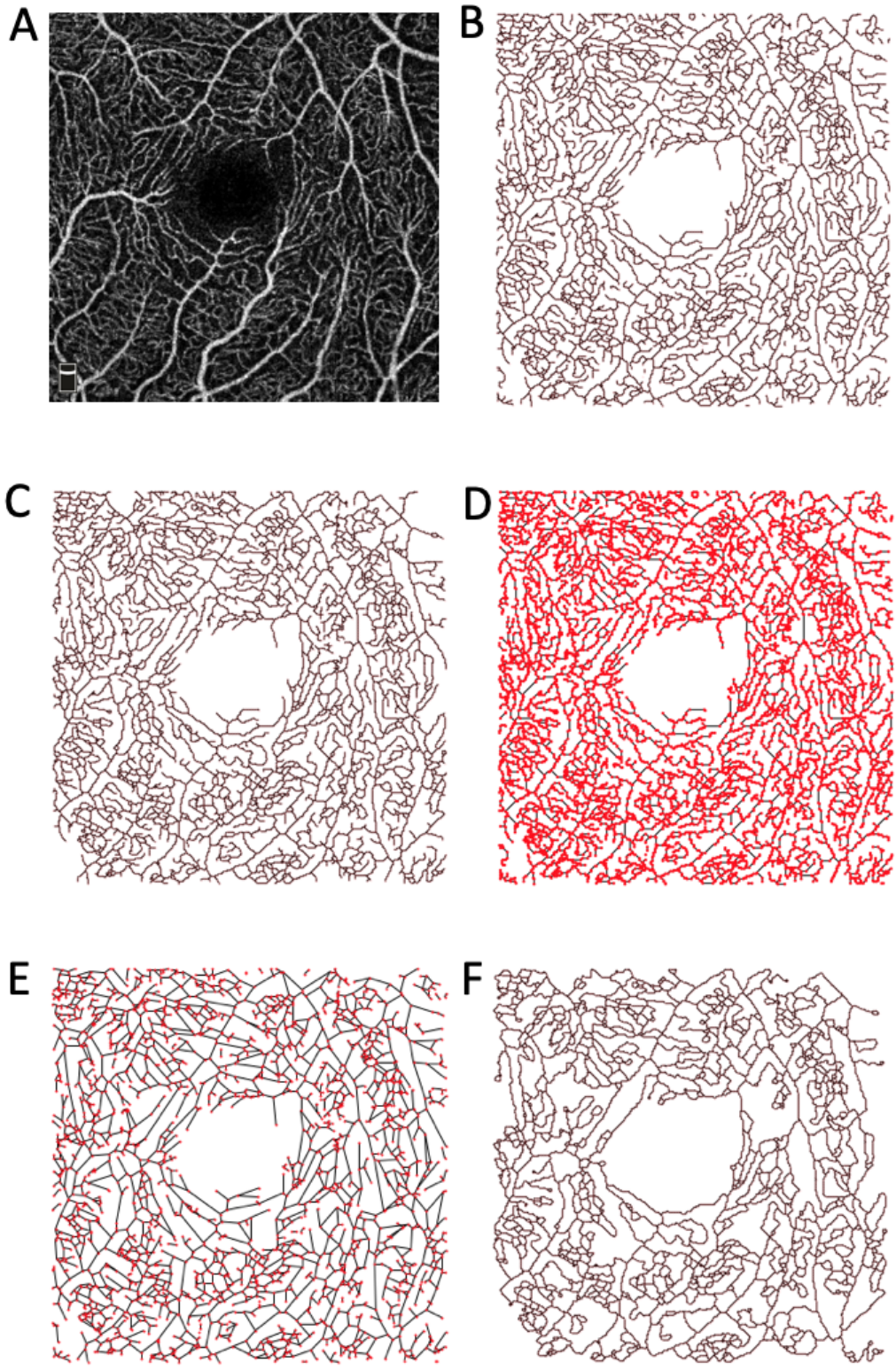

Figure 4.3: (A) Original image. (B) Original graph. (C) Largest connected component (D) Simplified graph using angles. (E) Simplified graph by nodes degree. (F) Loopy network.

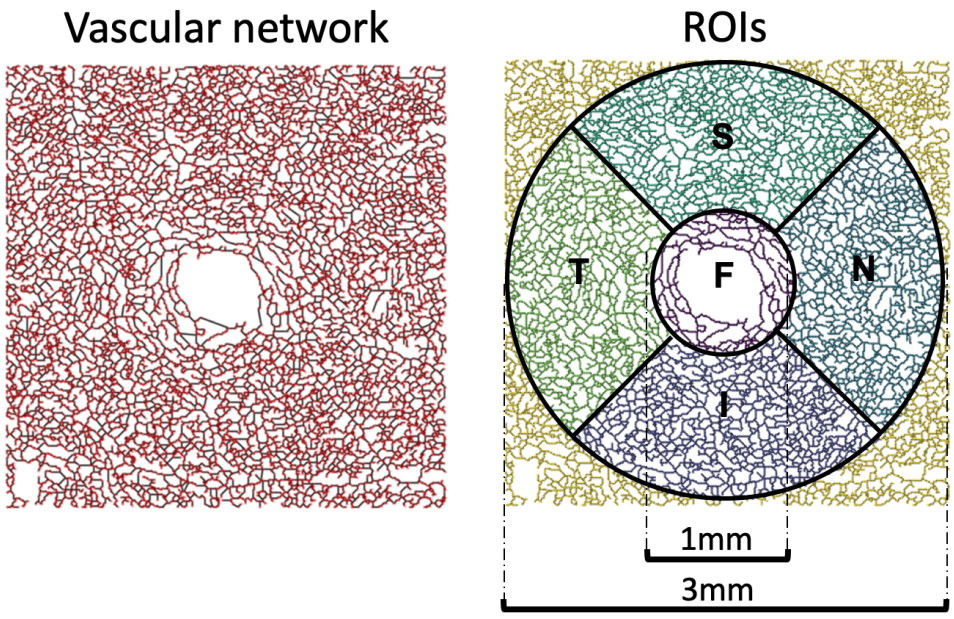

Figure 4.4: (A) Vascular network. (B) Regions of interests: foveal (F), nasal (N), superior (S), temporal (T), inferior (I).

4.5 Retinal vascular feature extraction

4.5.1 Graph-based metrics

Graph-based metrics are measurements borrowed from graph theory. They are used to characterise the span, sparseness, and tightness of the network, and they are used to obtain a global overview of the properties of the vascular plexus. These measurements are implemented in three sets of functions presented below.

Basic network functions

Considering a graph, *G=(V, E)*, besides the number of nodes ($|V|$), edges ($|E|$), leaf nodes, and branching points, the graph diameter and radius are reported. Defining the distance between the two nodes, $u, v \in V$, $d(u, v)$, as the length of the shortest path between them, it is possible to define the eccentricity of a vertex, v, in a connected graph, by finding the maximum of the distances between v, from all the other vertex, u, in G, *i.e.*,

$$ecc(v) \max_{u \in G} d(v, u) \tag{4.1}$$

(see figure 4.5). The diameter of a graph describes the maximum eccentricity of the network, and it is compute as

$$diameter = \max_{u \in G} ecc(v) = \max_{v \in G} \max_{u \in G} d(v, u), \tag{4.2}$$

whereas, the radius corresponds to the minimum eccentricity, defined as

$$diameter = \min_{u \in G} ecc(v) = \min_{v \in G} \max_{u \in G} d(v, u). \tag{4.3}$$

These metrics correspond to global measurements and are calculated to understand general properties such as the extension of the graph. Furthermore, using the network obtained after the simplification by degree, the graph density is computed as

$$density = \frac{2|E|}{|V|(|V| - |1|)} \tag{4.4}$$

and used as a measure of the sparseness of the network. Then, the average clustering coefficient (CC) is calculated as

$$CC = \frac{1}{|V|} \sum_{v \in G} c(v) \tag{4.5}$$

where $c(v)$ corresponds to the clustering coefficient for a node, v, and computed as the number of triangle connected to v over the number of triples (open triangle) centered around v (see figure 4.5). This metric can elucidate information about the global retinal landscape and how closely connected (tightness) are nodes in the network. Finally, considering a complete graph C, (*i.e.*, where every pair of nodes is connected through an edge) the number of non-edges of G, in comparison to C is reported to investigate the degree of connectivity of the network.

Radius network functions

Since each node in the network contains an attribute representing the radius of the vessel, it is possible to compute the distribution of radii in the whole network and across each region of interest. Analysis of vessels at different scales (large and small) can be performed by computing separately the radius distribution of large vessels identified either as vertices

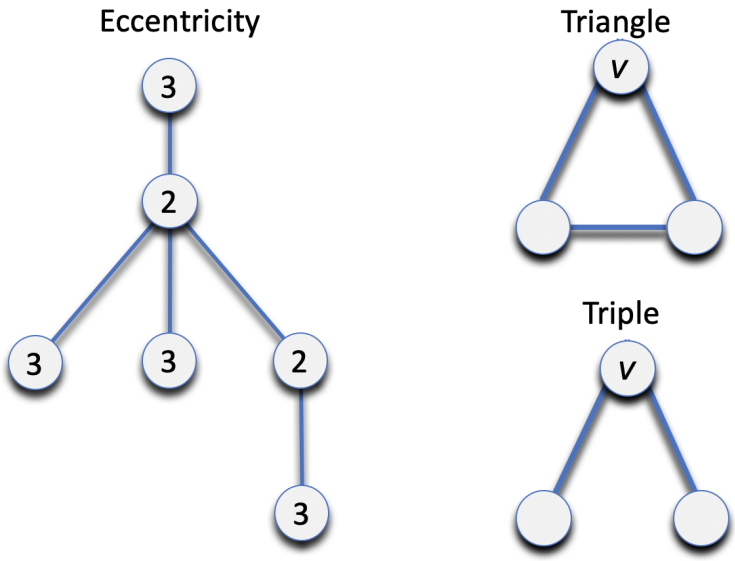

Figure 4.5: Eccentricity for reach node in the graph, and an example of triangle and triple centered at node v.

with radius attribute greater than 15 μm or by creating a binary image mask for large vessels during the binarisation process (example in figure 4.6).

Network paths functions

Using a combination of the simplification by largest connected component and the simplification by degree, the framework reports mean, median, standard deviation, kurtosis, and skewness of the distributions of the shortest paths between any two nodes in the network. By knowing the distribution of shortest paths in the network, it might be possible to infer functional properties of the vascular plexus, such as efficiency or impairment of nutrients transportation in the retinal capillary bed.

4.5.2 Coordinate-based metrics

Coordinate-based metrics are measurements related to the position of each node in the network. They capture geometrical properties of the vasculature and describe retinal measures related to the foveal avascular zone (FAZ), intercapillary spaces, and vessel morphologies.

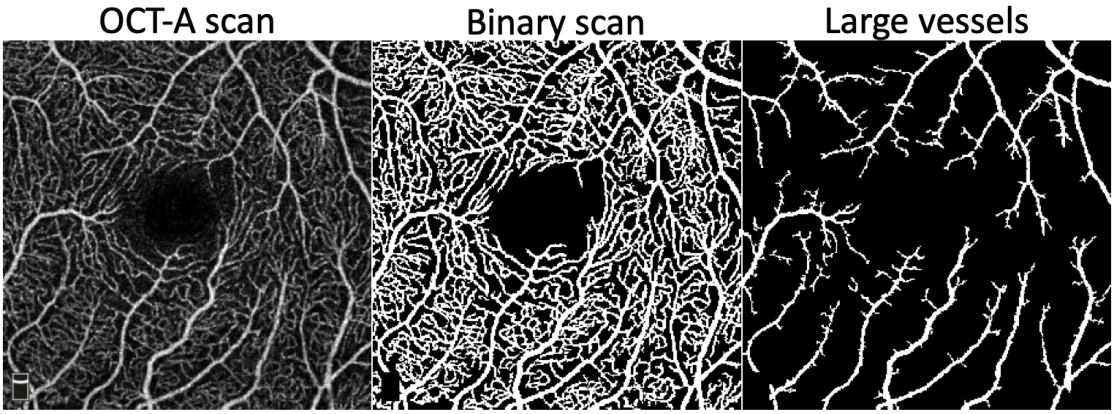

Figure 4.6: Original OCT-A scan, binary image after segmentation, and binarised image with only large vessels.

Foveal avascular zone

Contrarily to the other measurements, all the metrics related to FAZ are calculated using the superimposition of the superficial and deep capillary plexuses (SCP+DCP) to achieve the best visualisation of FAZ boundaries. The detection of this region is obtained by firstly identifying all the intercapillary spaces in the network, and then choosing the biggest among those. A graph data structure called the *doubly connected edge list (DCEL)* is used to detect the intercapillary spaces [120]. The main building block of a DCEL is a list of *half-edges*. Every actual edge, *e*, is represented by two half-edges going in opposite directions, called *twins*. Along the boundary of each intercapillary space, the half-edge is oriented counterclockwise and has exactly one previous half-edge, a next half-edge and a twin. The area enclosed by the half-edge is called *face* and corresponds to a retinal intercapillary space. An example is shown in figure 4.7A. A DCEL stores a list of half-edges, a list of vertices, and a list of faces. The implementation of DCEL to identify faces in the vascular network is based on the algorithm described by Schneider *et al.* (2015) [121]. An overview of the implementation is shown in algorithm 3. This approach has, however, some limitations. It is designed for undirected planar graphs and correctly finds all faces as long as they are simple polygons, *i.e.*, they have a finite area, an equal number of vertices and edges, and each vertex in the polygon has exactly degree equal to two. This means, that leaf nodes need to be pruned from the original network. DCEL method detects also an external face, (also called outer face), which, in this

implementation, is discarded based on a threshold on the size of the intercapillary spaces. Finally, FAZ detection is obtained as the face with the largest area among all detected faces. Once the nodes and edges describing the FAZ boundary are found, it is possible to compute morphological FAZ metrics. The framework calculates the area (A), perimeter (P), barycenter, shortest radius, and longest radius (figure 4.8B). By fitting an ellipse on the points describing the boundary, the major and the minor axis are computed and used to report the axis ratio (figure 4.8A). FAZ shape is characterised by using the acircularity index, computed as $P/(2\pi R)$, where R is the radius of a circle of size equal to the FAZ area, and the circularity index defined as $C = 4\pi A/P^2$. Finally, assuming B, the FAZ boundary, describing a path where an object can move, and each node of coordinate (x_i, y_i) in B as observations of the object taken in constant time intervals, the speed of the object, the curvature (the deviation of a curve from a straight line and using the equation in (4.10)), and the number of turning points (change in sign of the curvature) in the boundary are estimated to characterise the FAZ smoothness.

Intercapillary spaces

Intercapillary spaces can be detected using the DCEL data structure caveat to the algorithm limitations. Once all the faces are detected, average area and acircularity index are computed. Finally, circularity area ratio computed as the quotient between the size of the face and the size of a circle with radius equal to average face radius is reported.

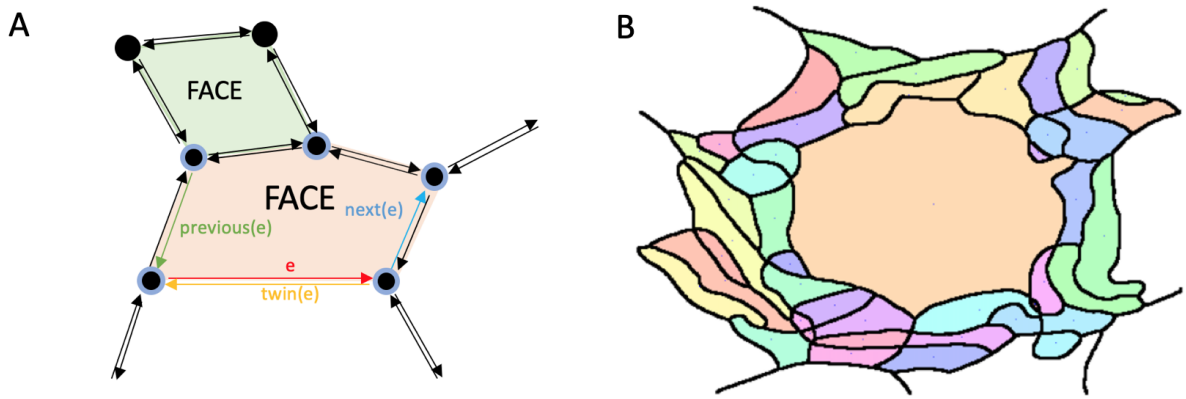

Figure 4.7: (a) Example of DCEL. (b) Faces in the foveal graph displayed in different colours.

Algorithm 3 Finding nodes describing a face

```
1:  function FIND _FACE_FROM_NODE(G, node)
2:      initialise face with one node
3:      while first element in face is not last element in face do
4:          next_node_candidates =get_neighbours(G, node)
5:          if length(next_node_candidates) = 1 then
6:              append node to face
7:          else
8:              next_node = candidate
                    with clockwise orientation
                    forming the minimum angle
9:              if next node is in face then
10:                 return face
11:             else
12:                 add node to face
13:                 node = next_node
```

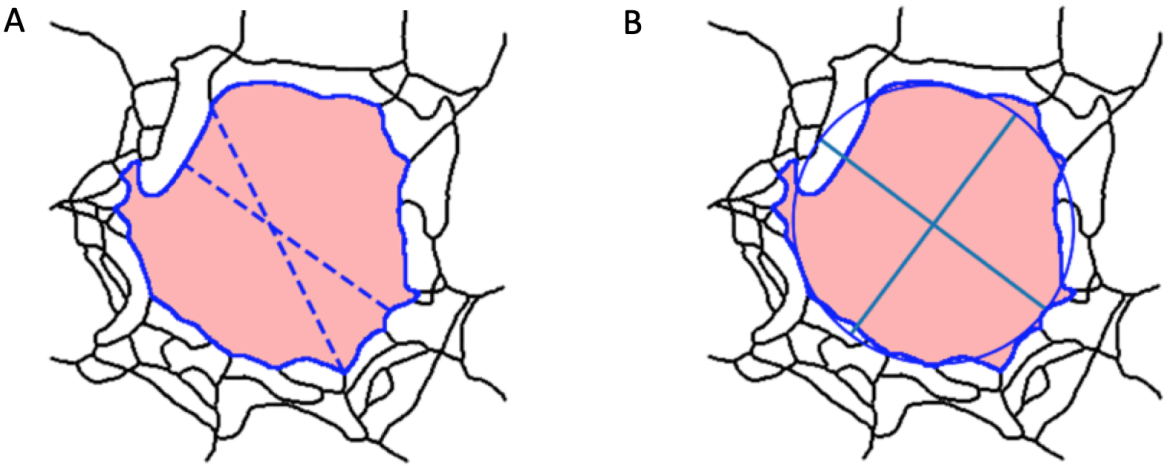

Figure 4.8: Examples of FAZ (red area) measurements. (a) Fitted ellipse with the major and minor axis. (b) Largest and smallest diameters passing through the centroid of the the polygon described by the FAZ.

Vessel Tortuosity

Tortuous blood vessels have been observed in different conditions, such as hypertension [122], diabetes [123], and cardiovascular diseases [124]. However, the concept of tortuosity is not biologically defined and more a subjective clinical judgment (typically on a scale of three to five severity categories). The translation of clinicians' perception of twisted vessels into a mathematical formula is still under investigation. Nonetheless, several properties for

this metric have been proposed. Considering a vessel s, its tortuosity, $\tau(s)$, should satisfy the following properties:

- *rotational and traslational invariance*, rigid transformations do not affect the perception of tortuosity;
- *composition*, given multiple vessel segments s_i for $i = 1, ..., n$ with tortuosity $\tau(s_i)$ the curve defined as the combination $s = s_1 \oplus ... \oplus s_n$ has equal or greater tortuosity than any of the composing vessels, that is

$$\tau(s_i) \leq \tau(s = s_1 \oplus ... \oplus s_n) \quad \forall i = 1, ..., n; \tag{4.6}$$

- *modulation*, it can be assumed that the tortuosity metric increases with the number of twists (changes in the curvature sign), and also with the curve amplitude. Considering φ and α the function counting the twists and the amplitude, respectively, if s_1 and s_2 are two vessels with equal amplitude then

$$\varphi(s_1) \leq \varphi(s_2) \Rightarrow \tau(s_1) \leq \tau(s_2), \tag{4.7}$$

  and if they have the same number of twists, then

$$\alpha(s_1) \leq \alpha(s_2) \Rightarrow \tau(s_1) \leq \tau(s_2); \tag{4.8}$$

- *response to scale*, how tortuosity perception changes with scale is not clear. Previous studies reported tortuosity metrics as invariant to scaling [125], other studies advised that scale affects the tortuosity in a multiplicative manner [126]. Others suggested that this property depends on vessel caliber as well. Hence, it is advisable to compare tortuosity in vessels of the same caliber [127].

In the last decades, several tortuosity measurements have been proposed to characterise the shape of arteries and veins not only in the eye but also in other anatomical regions [128], [129]. The following section summaries the most common measurements found in

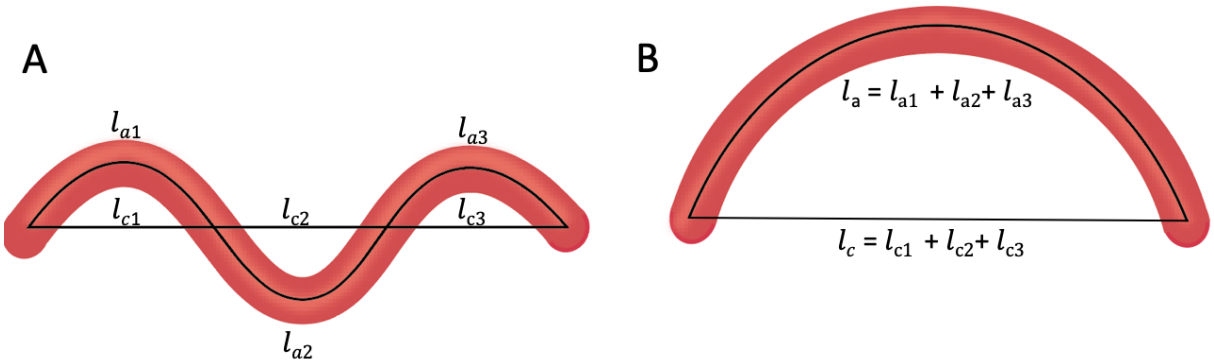

Figure 4.9: Two different blood vessels with equal τ_{DM}.

literature and computed on the skeleton of the vascular tree. They can be distinguished into three main groups: distance metrics, curvature approaches, and mixed methods.

Distance approach Distance metrics are the oldest approaches to compute blood vessel tortuosity. In particular, the *arc over the chord ratio* (τ_{DM}) is the most widely used tortuosity metric. It was proposed for the first time by Hart *et al.* (1999) [126] and it is based on a previous work of Lotmar *et al.* (1979) [130]. It is defines as

$$\tau_{DM} = \frac{L_a}{L_c}, \tag{4.9}$$

that is the ratio of the curve length (arch length L_a) and the euclidean distance (chord length, L_c) between the vessel endpoints (figure 4.10A).

Curvature approach Distance metrics have the disadvantage of assigning to very different curves the same tortuosity value as shown in the figure 4.9. Therefore, more sophisticated measurements to quantify the twistedness of vessels were proposed based on the concept of curvature. Among those, the most popular are *Hart's curvatures*. Given a vessel, s, consisting of the following points $[(x_1, y_1), ..., (x_n, y_n)]$, using Cartesian coordinates $t = (x(t), y(t))$, the curvature at point t is defined as,

$$k(t) = \frac{x'(t)y''(t) - x''(t)y'(t)}{[y'(t)^2 + x'(t)^2]^{3/2}}, \tag{4.10}$$

where x', x'', y', y'' represent the first-order and the second-order derivatives of x and y. The total curvature and the squared curvature are defined as

$$\tau_t = \int_{t_0}^{t_n} |k(t)|\, dt, \tag{4.11}$$

$$\tau_{st} = \int_{t_0}^{t_n} |k(t)|^2\, dt. \tag{4.12}$$

These measurements can be normalised using either the arch length, L_a, or the chord length, L_c. Another curvature-based method is the *sum of angles metric* (τ_{SOAM}) which is defined as the sum of angles between the tangent to the vessel s in a point i and a reference axis over the total chord length. Proposed Smedby *et al.* (1993) [131] and reused by Bullitt *et al.* (2003) [128] (figure 4.10B), it is calculated as

$$\tau_{SOAM} = \frac{\sum_i \alpha_i}{L_c}, \tag{4.13}$$

where α_i are the angles computed at each point, and L_c is the path length.
Based on (4.10), Trucco *et al.* (2010) [127] proposed a curvature metric that also takes into account the vessel caliber. Starting from an adaptation of Hart's curvature,

$$\tau = \left(\sum_j |k_s(j)|^p \right)^{1/p}, \tag{4.14}$$

where p is a positive integer chosen empirically [127] and s represent the skeleton of the vessel, the curvature is computed by identifying the vessel boundaries, B_1 and B_2 and calculated as

$$\tau_{Trucco}(k_{B_1}, k_{B_2}, p) = \left(\sum_j \frac{|k_{B_1}(j)|^p + |k_{B_2}(j)|^p}{2} \right)^{1/2}. \tag{4.15}$$

Finally, another tortuosity metric based on the curvature concept is the *slope chain code* (SCC) method. It was proposed by Bribiesca (2013) [132] and is based on converting the continuous curve into a sequence of straight line segments of constant length with

endpoints touching the curve and calculating their slope a for each of the n segments

$$\tau_{SCC} = \sum_{i}^{n} |a_i|. \tag{4.16}$$

Mixed approaches Different methods take advantage from both distance and curvature metrics. The *inflection count metric* (τ_{ICM}) considers the change in sign of the curvature and is defined as the distance metric multiplied by the number of inflection points (n_s) in the vessel s (figure 4.10C) [128],

$$\tau_{ICM} = n_s \frac{L_a}{L_c}. \tag{4.17}$$

Similarly, in *Grisan's curvature* (τ_{Grisan}), each vessel is divided into n segments based on the number of points where the curve changes sign and it is defined as follows

$$\tau_{Grisan} = \frac{n-1}{n} \frac{1}{L_c} \sum_{i=1}^{n} \left[\frac{L_{ai}}{L_{ci}} - 1 \right]. \tag{4.18}$$

Tortuosity measures integration It should be noted that a tortuosity value is obtained for each vessel in the vascular network. This leads to a distribution of tortuosity values for each retinal image. Studies have reported different ways to combine these measurements. Taking the average of τ is the simplest and widest used solution. However, recent studies have also proposed the following weighted formula to compute the total tortuosity:

$$\tau = \frac{\sum_i^n L_{ai} \tau_i}{\sum_i^n L_{ai}}, \tag{4.19}$$

where L_{ai} is the arch length of vessel s_i with $i = 1, ..., n$ making up the vascular tree [133]. Hence, some tortuosity measures are dimensionless, and other are considered as density with unit measure 1/length.

Tortuosity and curvature in OCT-A vascular network In the OCT-A network analysis pipeline, vessel tortuosity is measured based on the simplest metric previously reported in equation (4.9). Given a vessel segment, s, $\tau(s)$ is computed as the ratio between the graph

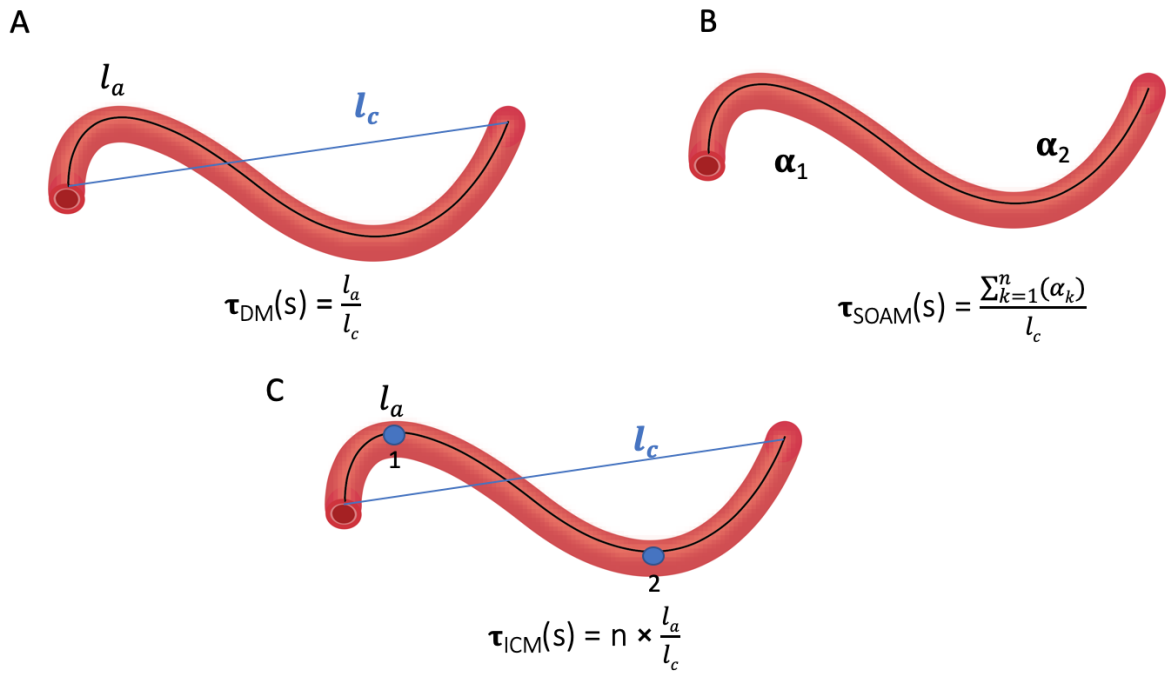

Figure 4.10: (A) Tortuosity as distance metric. (B) Tortuosity computed using sum of angles metric. (C) Tortuosity considering the inflection counts.

distance (arc length) and the euclidean distance between its endpoints. The way in which the network is constructed (one node for each pixel in the skeleton) leads to multiple nodes of degree two between bifurcations or leaf nodes. Hence, to compute the graph distance between two consecutive nodes of interest (i.e., vessel endpoints), a dictionary containing all the nodes in the path is created such that for each couple of endpoints it is possible to calculate their graph distance (arc length) as the sum of the euclidean distances of the nodes of degree two that are contained in that path (algorithm 4). Figure 4.11 shows an example of how to compute the tortuosity ($\tau_{N_0N_n}$) of the vessel with endpoints N_0 and N_n,

$$\tau_{N_0N_n} = \sum_{i=1}^{n} \frac{d_{N_iN_{i-1}}}{d_{N_0N_n}}. \tag{4.20}$$

As previously discussed, this metric does not take into account changes in the sign of the curve, hence, among the coordinate-based metrics, the framework reports also vessel curvature as described in equation (4.10). It is worth noting that recent studies have reported significant changes in tortuosity between arteries and veins [124], however since

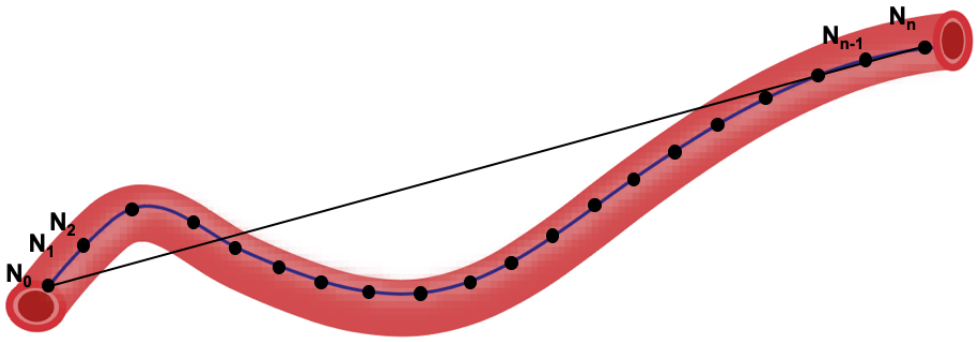

Figure 4.11: Example of tortuosity calculation in a vessel of the vascular network in the OCT-A network analysis framework.

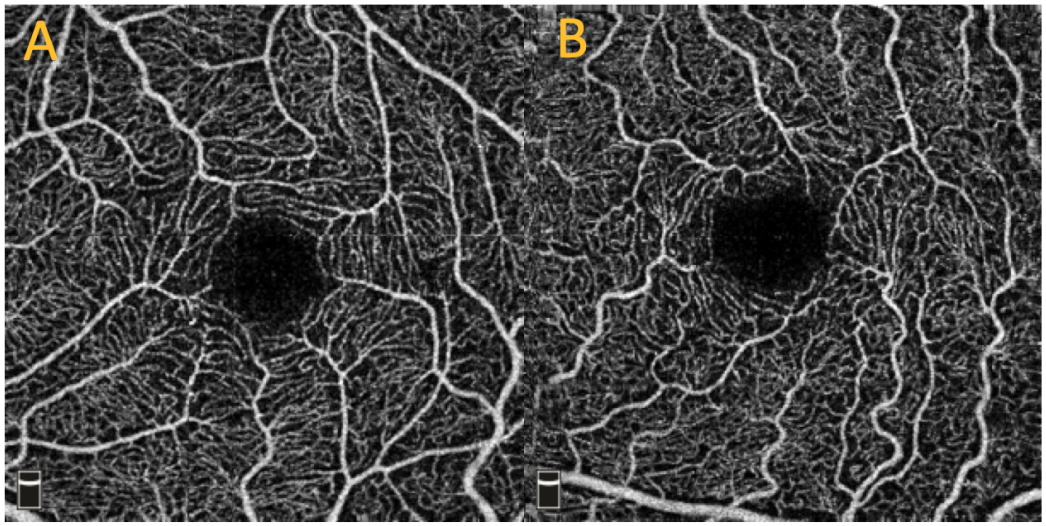

Figure 4.12: (A) Example of retinal vasculature in a normal eye. (B) Retinal vasculature of a patient suffering from chronic kidney disease and presenting highly tortuous large vessels.

the classification of vessels in OCT-A images is still an open problem, tortuosity and curvature are currently reported as the average measure across all vessel segments. Moreover, since caliber might play a role [127], the framework allows the computation of these measurements also for the largest vessels in the image (figure 4.12). Finally, the tortuosity of paths in the network is also reported by computing the shortest path between two random nodes in the network and reporting the distance between each node along the path and the straight line connecting the initial random nodes. The process is repeated 50 times to report the basic statistics on the tortuosity distribution.

Algorithm 4 Compute tortuosity

```
1:  procedure GET TORTUOSITY DISTRIBUTION(G)
2:      S = SimplifyGraphByDegree(G)                    ▷ to retrieve vessels endpoints
3:      function NODESONPATH(G, S)   ▷ Create dictionary with nodes on endpoints path
4:          for node in nodes(S) do
5:              neighbours = find_neighbours(node)
6:              if (neighbours, node) not in dictionary then
7:                  add endpoints as key in dictionary
8:          for key in dictionary do
9:              dictionary[key] = nodes_on_paths(G, key)
10:             return dictionary
11:     for endpoints, node_on_path in the dictionary do
12:         chord_length = chord distance(endpoints)
13:         arc_length = arc distance (nodes_on_paths)
14:         tortuosity_endpoints = arc_length / chord_length
15:         add tortuosity_endpoints to tortuosity
16:     return tortuosity
```

4.5.3 Topology-based metrics

Graphlets and network motifs

Geometric measurements may not be entirely exhaustive in capturing network properties or can be computationally intractable in the case of large and complex networks. Therefore, sensitive measures of local similarities to characterise networks structure and comprehend relationships between large and complex graphs have been proposed. Described for the first time by Pržulj *et al.* (2004) [134], graphlets have been widely used to analyse similarites between biological networks such as protein-protein and cellular interactions shedding light on functional and molecular processes of the biological systems [135], [136]. Consider a graph, G, a subgraph, S, of G is defined as a network whose nodes and edges belong to G. If S contains all the edges that are in G for each pair of nodes, then S is called *induced subgraph*. *Graphlets* are non-isomorphic classes of small connected induced subgraphs of a larger network that can characterise repeated structures in large and complex networks. Figure 4.13 shows 2-, 3-, and 4-node graphlets. To characterise similarities between networks, two main approaches have been developed: the *relative graphlet frequency distance* [134] based on the counts of appearance of 3-5 node graphlets, and the *graphlet degree distribution agreement* which consider all the counts a node touches all 2-5 node graphlets to construct a signature vector for each network (further details can be found in [135]). The OCT-A network analysis framework takes advantage of the definition of graphlets and creates network motifs (which differ from graphlets for their induced property) and uses the frequency count of 2-4 node graphlets to characterise patterns in the retinal plexus. The computational time is reduced by using the simplification by degree with discard geometric properties of the network. For each node in the graph, a sub-area of up to 4-step neighbours is selected to explore and identify the network motifs containing that node. Graphlets counts and statistics about the length and radius are reported. Examples of graphlets detection in simple networks and in a foveal region are shown in figure 4.14.

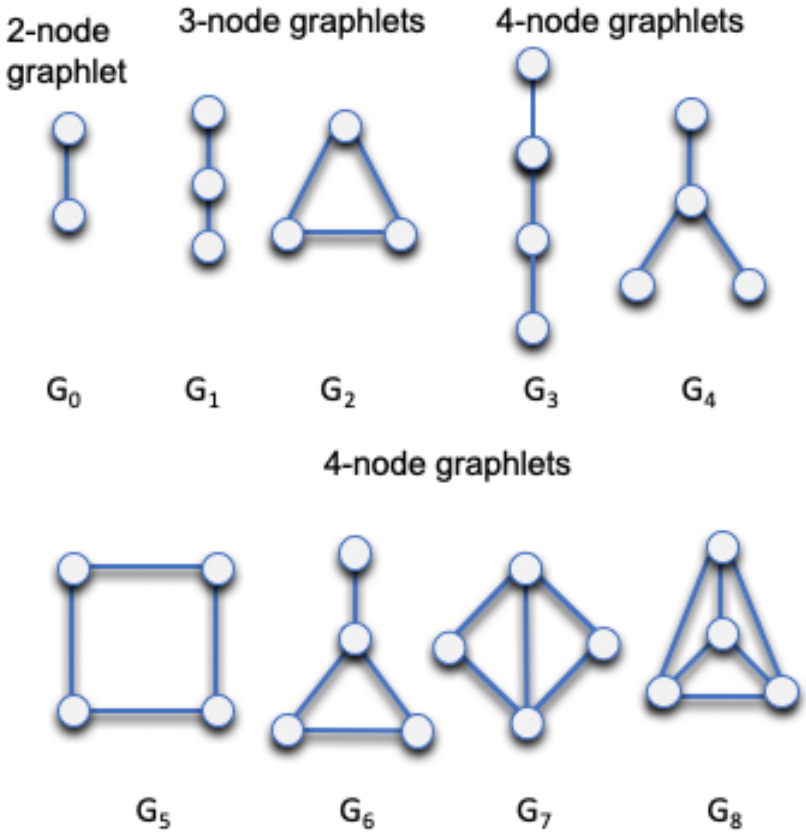

Figure 4.13: Graphlets up to four nodes.

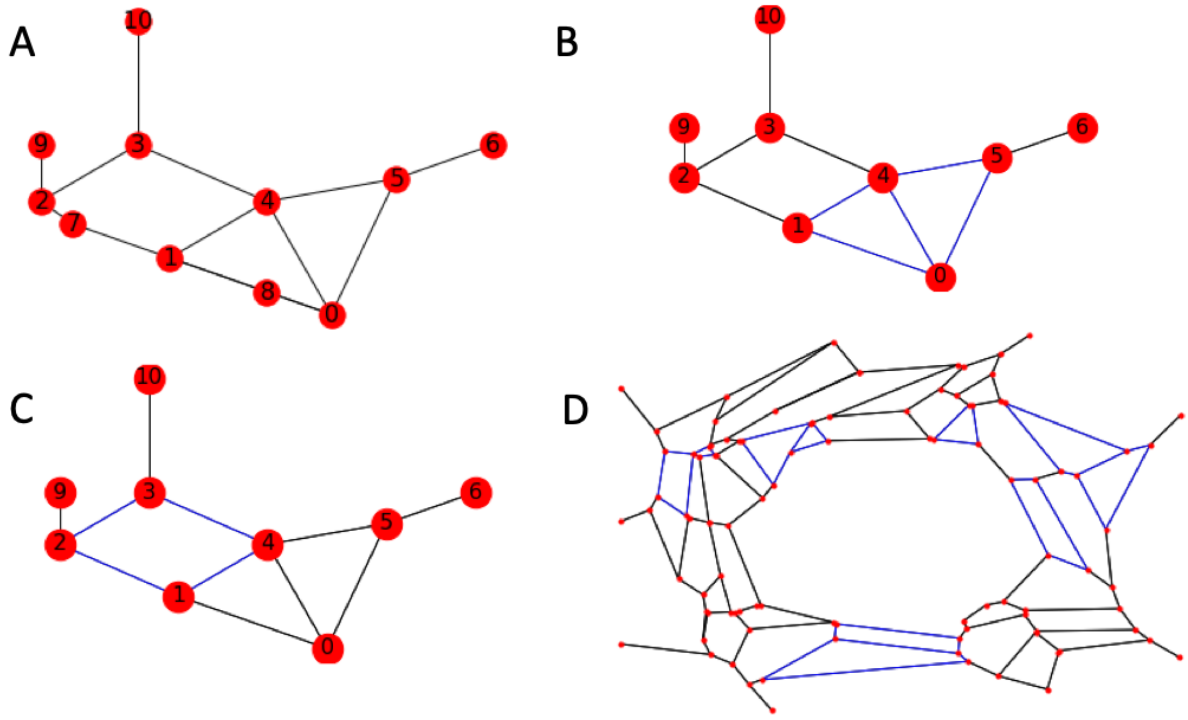

Figure 4.14: (A) Example of an undirected planar graph. (B) Detection of graphlet G7 in the example graph. (C) Detection of graphlet G5 in the example graph. (D) Detection of graphlet G5 in a simplified network modeling the vasculature in the foveal region (the central part of the vascular network).

Binary Tree

The retinal capillary bed is a network of intertwined vessels. Understanding the degree of complexity of this graph can reveal valuable insight into disease detection and progression. The study of the complexity of large and intertwined biological systems can, however, be challenging. Therefore, previous works have proposed a simplification of this problem by mapping the loopy network into a simpler binary tree structure and investigating the characteristics of this new graph. [137]. Binary trees are graphs in which each node has at most two children. They are well-characterised data structures in graph theory and several metrics capturing tree properties have been already developed. The proposed approach maps all faces in the vascular graph into leaf nodes of the binary tree. Then, according to a previously selected rule, when an edge of the original network is removed, two faces join to form a larger one. This leads to the creation of a parent node in the binary tree from the two leaves representing the initial two faces. By progressively

eliminating edges in the vascular network, parent nodes are added to the binary tree. This process is outlined in figure 4.15. The implementation for OCT-A network structures requires the following steps: (i) starting from the network obtained using the simplification by degree nodes of degree one are pruned to obtain a final network containing only loops (i.e. faces), (ii) DCEL data structure is applied to detect all the faces in the network which will represent the leaf nodes of the binary tree, (iii) the tree root is enforced by creating a pseudo loop surrounding the initial network as shown in figure 4.16, (iv) progressively, edges are removed according to the smallest attribute (either width or length), and smaller loops join to create a bigger loop.

Tree metrics Once the binary tree is built, it is possible to investigate metrics such as the *tree depth*, as the average of the number of edges from the root to each leaf node and representing the homogeneity of the distribution of the intercapillary spaces over the network structure, *tree altitude*, as the length of the longest path from the root to the deepest node, indicating the level of nestedness of the network, and tree asymmetry as defined by Katifori *et al.* [137], as a measure of the deviation from a perfect binary tree and a measure of the homogeneity of the intercapillary spaces in the retinal plexus.

Horton-Strahler branching ratio Tree shape can be characterised by using the Horton-Strahler branching ratio (HS) described by Horton *et al.* (1945) [138]. It is calculated by giving a hierarchical ordering (HS number) to each edge of the binary tree. The HS algorithm starts by assigning order one to each edge with a node of degree one (also called, external edges). If a parent edge has at least two children of order i, then its order is $i+1$, otherwise remains i (figure 4.17). The HS branching ratio is obtained for each order in the hierarchy i and is computed as

$$HS_i = \frac{n_i - 1}{n_i}, \tag{4.21}$$

where n_i is the count of edges of order i. The overall HS ratio can be obtained as average over all HS_i. Finally, external edges (HS number equal to one) can be further divided into either external- external (EE), if the sibling edge is also external or external-internal (EI)

otherwise. The counts of EE, EI, and their normalisation with respect to the total number of leaves are reported as features of the vascular network.

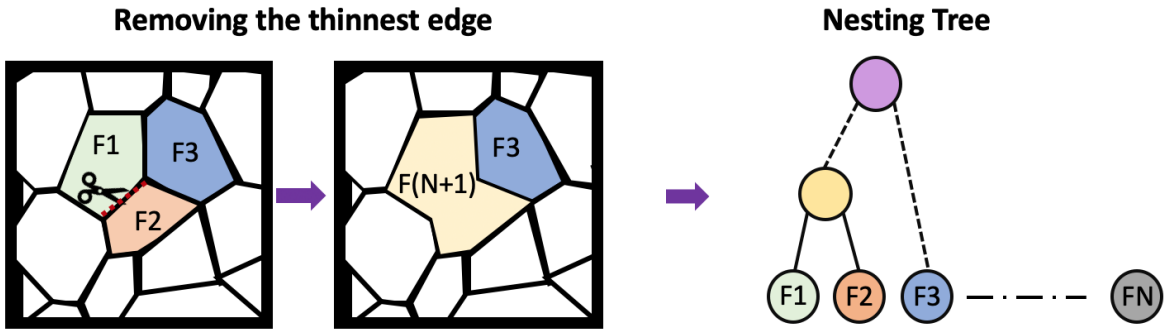

Figure 4.15: Overview of the algorithm into map loopy network in a binary tree.

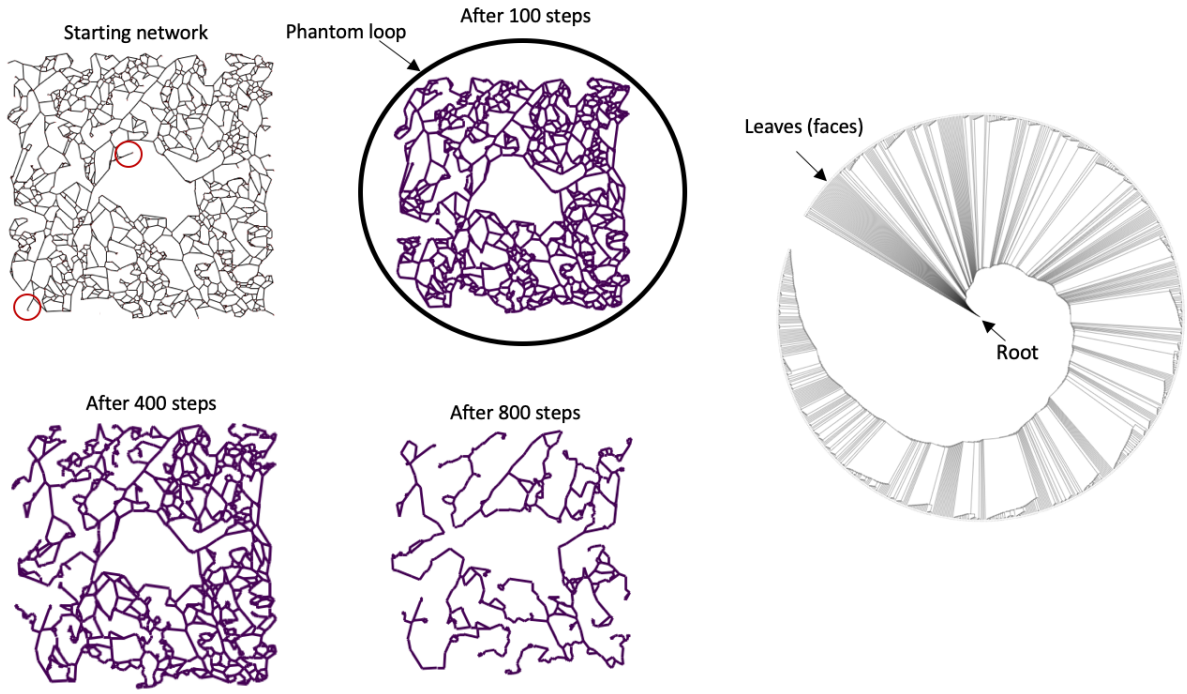

Figure 4.16: Example of progression of the binary tree construction. Red circles are places on leaf nodes to remove before the starting of the algorithm, then a phantom loop is created. At each step an edge is removed. Finally a binary tree (with circular layout) is displayed.

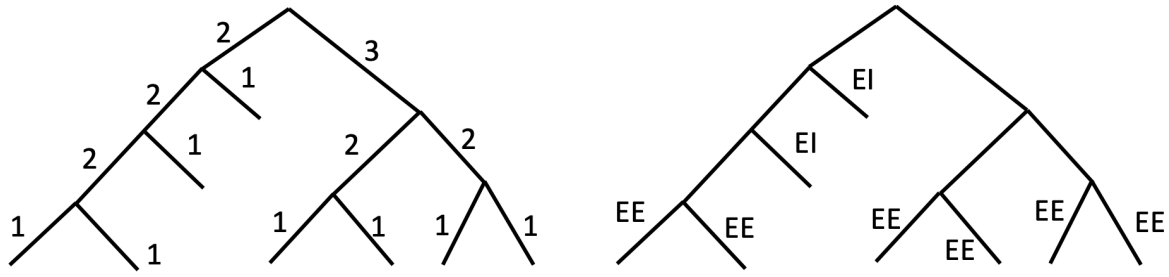

Figure 4.17: (A) Example of HS branching ordering. (B) Identification of EE and EI edges.

Random walks

Random walks are stochastic processes that can reveal information about functional (diffusion) and structural (heterogeneity) properties of a network. A random walk in a tight and dense structure is expected, with a high probability, to remain inside the same community. Using this property in OCT-A vascular networks, it is possible to capture global features of the network, such as density and sparseness of the network. In this work, default parameters are 1000 walks of length 300 nodes. All walks start from a randomly selected node. Then the length of the walk is compared to the euclidean distance between the start and end node.

4.5.4 Flow-based metrics

Previous studies have reported a measurement called flow index associated with OCT-A images computed by using an average of the decorrelation value obtained from the B-scans creating the OCT-A volume. However, not all OCT-A devices allow access to the volumetric data. Therefore, in this framework, two metrics are implemented to assess functional characteristics of the retinal plexus and gain insights into the vasculature haemodynamics only using 2D OCT-A images.

Vessel resistance

Vessel resistance is computed using Poiseuille's law which states that the resistance, defined as a function of pressure and flow, can be also estimated by knowing the length and the radius of the vessels under the assumption of cylindrical shape. In particular, given a vessel

s, its resistance R_s can be defined as

$$R_s(l, r) = \Delta P / Q = 8\eta l / \pi r^4, \tag{4.22}$$

where ΔP is the pressure difference between the two endpoints of the vascular segment and Q is the flow rate. In the OCT-A vascular networks, the length (l) corresponds to the edge connecting two bifurcation points (or leaf nodes) and the radius (r) is the attribute of the edge computed as the average radius of its endpoints. Therefore, the resistance at each vessel segment can be computed by assuming a constant blood viscosity. In this work, η is set to $2.084 \times 10^{-3} Pa \cdot s$ [139].

Vessel capacity and intercapillary space

Blood vessels carry oxygen and nutrients for the surrounding tissues. Considering the area of an intercapillary space (which corresponds to a face in the graph) and the capacity of the vessels making up its boundary (under the assumption of cylindrical shape), a novel metric called area to vessel capacity flow ratio (a2f) is proposed. This measure may elucidate areas in the retina deprived of nutrients and oxygen, and at high risk of ischemia. Figure 4.18 shows an example of a2f metrics computed in the intercapillary spaces surrounding the FAZ in the foveal region.

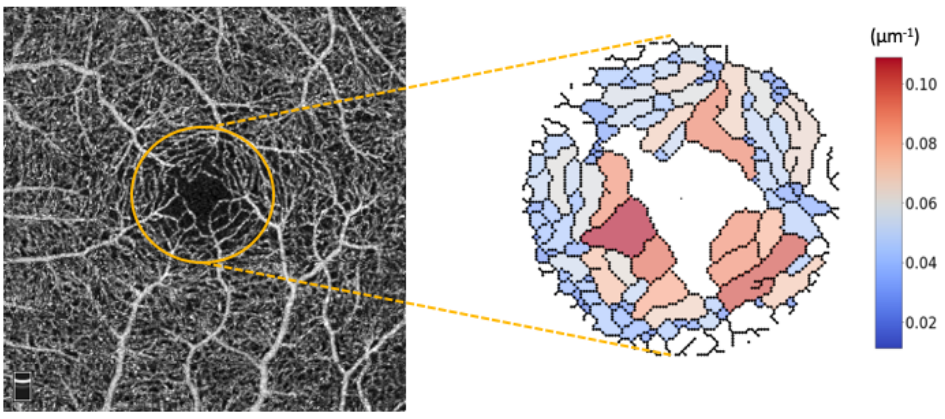

Figure 4.18: Examples of a2f value computed in the intercapillary spaces in the foveal region defined as the circle of 1 *mm* diameter centered at the FAZ.

4.6 OCT-A retinal phenotypes and challenges in predictive models

This framework proposes hundreds of retinal features to characterise structural and functional properties of vascular networks that can be used to train machine learning models for patient classification. Nonetheless, large sets of retinal features can have a potential downside when predictive methods for clinical investigation are applied. Indeed, OCT-A is a fairly recent technology and current datasets are limited to a few hundred or even less images. Hence, the ideal relation between the number of samples and the number of features is reversed in these investigations. This can cause what is known as *peaking phenomenon*: a disproportion between the number of samples and the number of features leading to poorer classification performances [140]. A common approach to solve the peaking phenomenon is to perform feature selection.

Many methods have been developed to perform a selection when a large number of potential features are available. **Supervised** methods are based on apriori decisions such as well-known clinical biomarkers. **Unsupervised** methods can be divided in *embedded (or intrinsic) methods*, where feature selection is part of the chosen model, such as in logistic regression with lasso regularisation, *wrapper methods*, where the selection depends on the given model and the best subset of features is selected according to the model evaluation, examples are the recursive forward elimination (REF) and backward elimination, and *filter methods*, which are independent of the predictive models and select features according to structural rules, such as mutual information (see appendix A, statistical tests, relief [141], minimum redundancy maximum relevance mRMR [142]. An overview of the feature selection methodologies is shown in figure 4.19 These methods can help in retrieving only the informative features and achieve better classification performances. Some of these methods will explore in the next chapters along with applications of the OCT-A computational framework.

4.7 Robustness of OCT-A microvascular phenotypes

Standardisation of OCT-A processing is a crucial point for the reproducibility of studies and the reliability of meta-analysis. This means that a better understanding about the

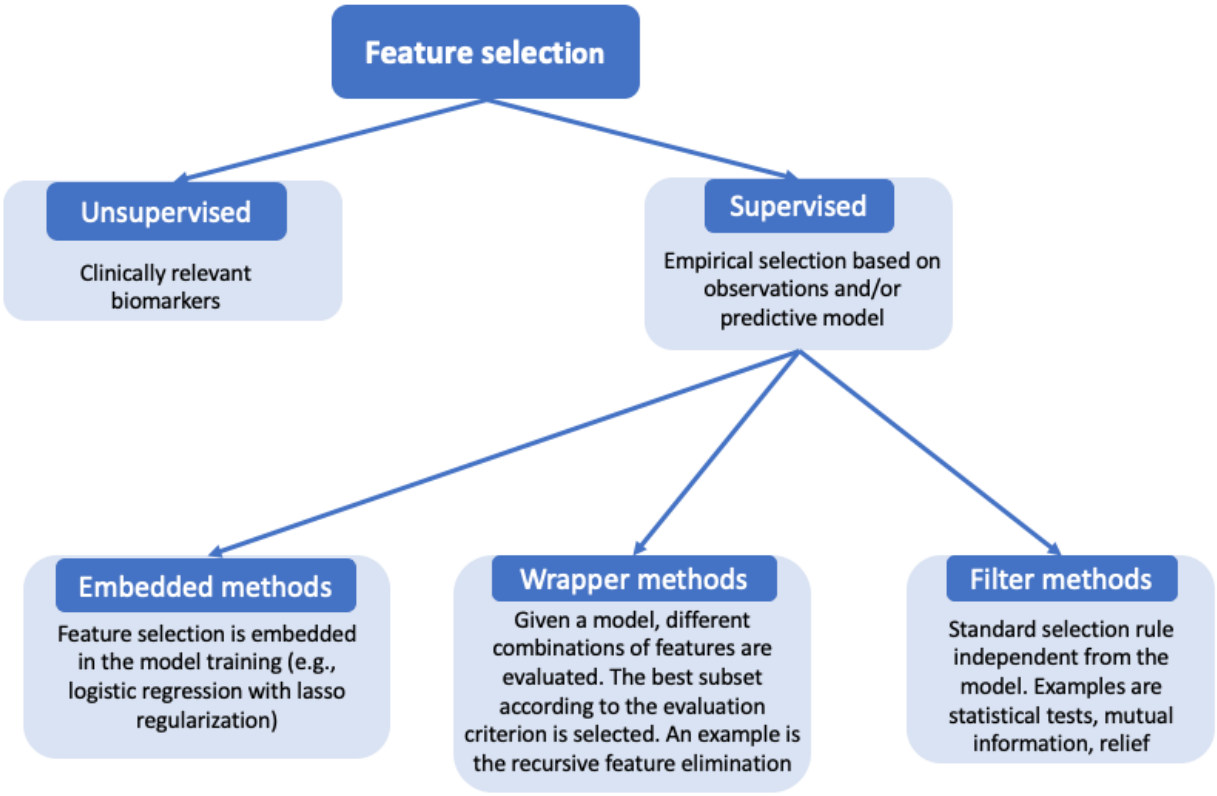

Figure 4.19: Overview of feature selection methods.

sensitivity of the extracted OCT-A features to the image quality is required. Differences in OCT-A retinal phenotypes from multiple scans can arise from several sources. Image quality is affected by the experience of the operator, by patient motion, and possibly by time of acquisition (before or after meals), caffeine intake, and medications. Segmentation errors can be introduced by the image processing, *e.g.*, low signal to noise ratio can create disconnections in the vasculature, affecting potentially retinal measurements.
In the following paragraphs, the robustness of the implemented retinal phenotypes is investigated by acquiring repeated OCT-A scans at multiple time points. Statistical tests were used to assess if the difference in the value of the retinal features across scans was either negligible or significantly different. If values were inconsistent across repetitions, features were assumed to be sensitive to the image processing and possibly not reproducible.

4.7.1 Repeated OCT-A scans

OCT-A scans of 18 healthy volunteers at three time points during the same day (0900, 1200, 1600) were acquired at the Queen's Medical Research Institute, Edinburgh, using an RTVue-XR Avanti (Optovue, Inc., Fremont, CA) device. An example of repeated OCT-A scans in the same participant is shown in figure 4.20. Only images on the right eye (OD) and free from any observable artifacts such as vertical and horizontal line distortions, quilt defects, and not-centered scans (figure 4.21) were included in the analysis. Finally, since the framework automatically centers the image at the foveal barycenter, OCT-A registration was not performed.

4.7.2 Statistical analysis

Difference between repeated measurements were assessed by assuming the 0900 scan as the baseline value, and the two repetitions as independent follow up measurements. For each retinal feature, the standard error is computed as defined in the following formula

$$err_{std} = \frac{p_{followup} - p_{baseline}}{p_{baseline}}, \tag{4.23}$$

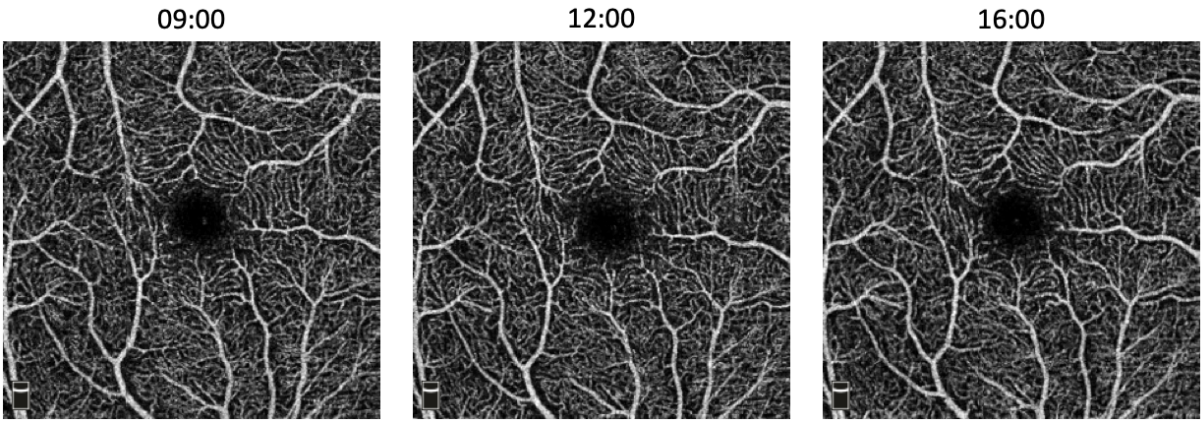

Figure 4.20: OCT-A of the SCP layer of the same eye captured at three different time points during the same day) 9:00, 12:00, and 16:00).

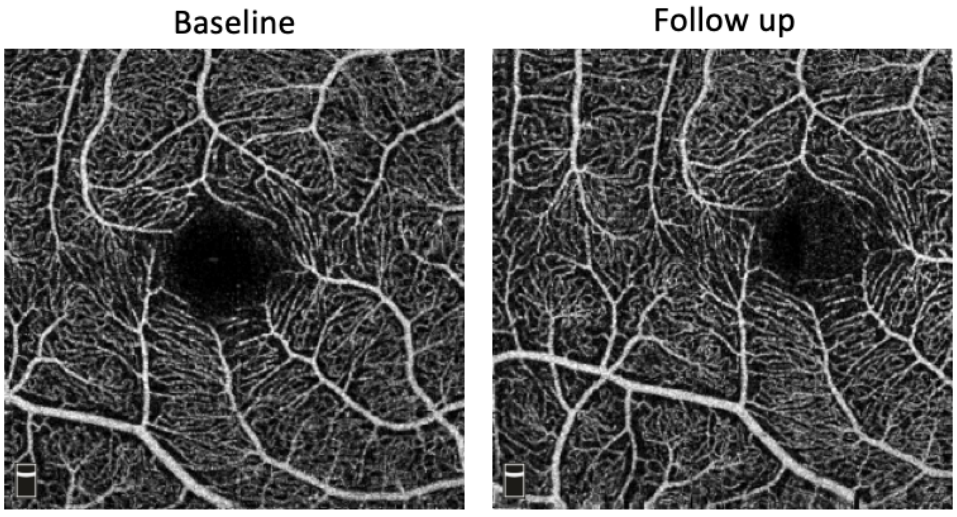

Figure 4.21: Example of discarded OCT-A images because repetition is not well-centered around the foveal region.

where $p_{followup}$ and $p_{baseline}$ are the retinal phenotypes in the follow up scan (either at 12 or 16 to increase the sample size) and at baseline, respectively. The distribution of errors is then analysed using statistical tests. If changes in any phenotype are distributed around zero (one-sample *t*-test or Wilcoxon-Mann-Whitney test (depending on data normality), It is assumed that the differences seen are due to imaging artefacts but free from any increasing/decreasing trend that could be associated with time. Otherwise, it is concluded that structural/functional changes (i.e., reduced/impaired blood flow in the vasculature) have occurred between visits.

4.7.3 Results

Among a total of 641 phenotypes, only the standard errors of 52 measurements were not distributed around zero ($p<0.05$). Five unstable phenotypes belonged to the graph-based metrics, 21 to the coordinate-based metrics, 4 to the flow-based metrics, and 22 to the topology-based. A table with those retinal phenotypes and p-values can be found in Appendix C. Figure 4.22 shows the distribution of errors in six stable retinal phenotypes, number of nodes in the graph, FAZ area, FAZ acircularity, tortuosity in the whole (W) network, HS branching ratio, and vessel resistance in the foveal region (F). Figure 4.22 reports the distribution of other six phenotypes that are unstable across repetitions, graph diameter in the superior region (S), mean face areas (F), mean tortuosity in the inferior region (I), graphlets 5 count in the nasal region (N), mean random walk length (W), kurtosis resistance (I). This is the first step towards a better standardisation of retinal vascular phenotypes.

Future work will involve the investigation of the source of high variability in measurements, low signal strength on the OCT-A scan, segmentation approaches, and graph construction, and the study of image processing techniques such as frame averaging across OCT-A scans which as a possible approach to reduce the source of variability of OCT-A scans and resolve binarisation uncertainties [88].

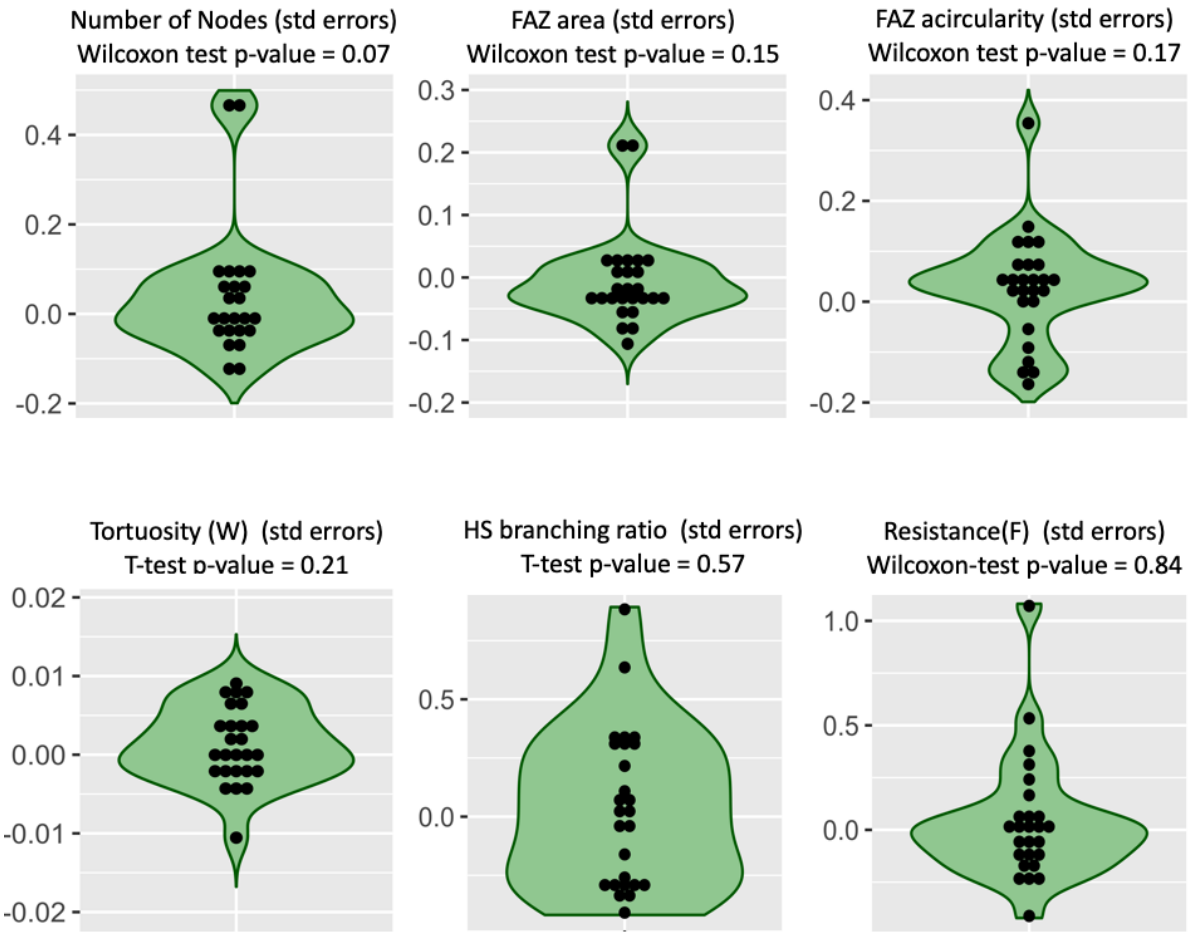

Figure 4.22: Example of phenotypes with standard errors distributed around zero: nodes in the graph (W = whole image), FAZ area, FAZ acircularity, tortuosity (W), HS branching ratio, vessel resistance (Foveal).

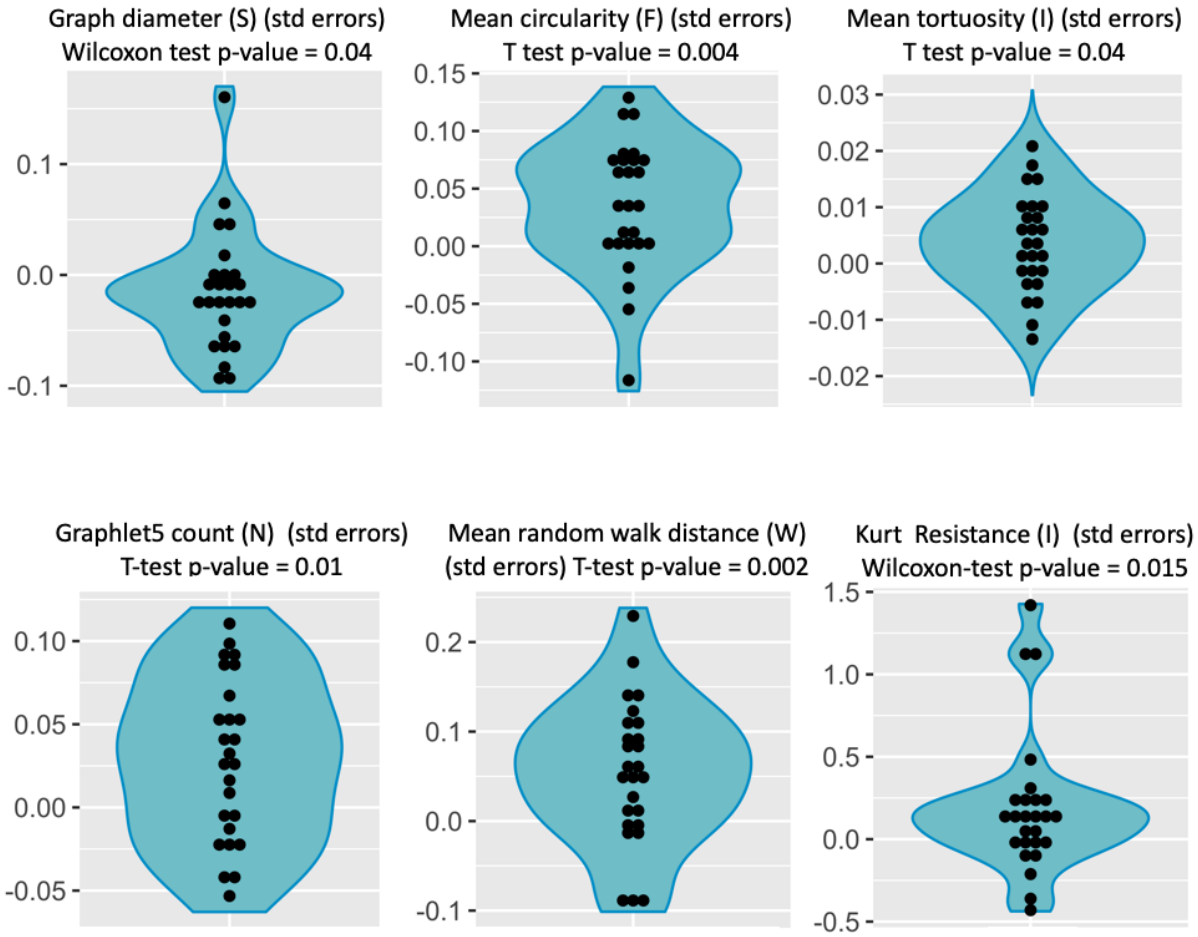

Figure 4.23: Example of phenotypes with standard errors not distributed around zero: graph diameter (Superior), mean face areas (F), mean tortuosity (I), graphlets 5 count (Nasal), mean random walk length (W), kurtosis resistance (Inferior).

4.8 Discussion and future work

This chapter described the implementation of the network analysis framework for the extraction of functional and structural metrics able to characterise the microvasculature in OCT-A images. Novel retinal vascular phenotypes were implemented to unravel information about geometric and topological properties of the network addressing the problem of limited and not sufficient microvascular phenotypes to cover the wide spectrum of retinal candidate biomarkers. This will allow the hypothesis-free discovery of retinal phenotypes associated with diseases and the possibility to clinically interpret retinal features to elucidate biological mechanisms and characterise disease progression.

The robustness of these phenotypes was tested by comparing measurements across multiple repeated OCT-A scans in healthy volunteers. Results showed 589 stable retinal features and 52 unstable phenotypes over time. The possible sources of variability in OCT-A scans and the challenges in using a high number of retinal features to predictive patient status were discussed. Limitations of this analysis include the small sample size and the high number of tests performed. Since hundreds of retinal phenotypes are analysed, the possibility of obtaining false negative results (Type II error) is inflated [143]. Hence, future work should investigate the robustness of these phenotypes on a larger number of images, and explore the use of statistical correction (*e.g.*,Bonferroni and false discovery rate) to account for the large number of tests.

Limitations of the framework include computational costs and customisation to a single OCT-A imaging device. Running time depends on multiple factors which relate to the machine (*i.e.*, single vs multiprocessor) and to the image itself (*i.e.*, vessel density). The first sequential steps of the computation framework *i.e.*, image processing and network modelling, can take up to 20 minutes for a single image. Whereas the computation of retinal features, which can be performed in parallel, varies according to the specific metric of interest. For example, graphlets metrics can require up to 3 hours for a single image. Furthermore, the OCT-A framework implementation is solely based on images acquired using one OCT-A device and on images with $3 \times 3\ mm^2$ field of view. Hence, future works will involve further optimisations to speed up computations and the generalisation of this framework to images captured using different devices and with larger field of view. Moreover, implementation of further retinal metrics such as branching angles, more

efficient tortuosity metrics, and fractal dimension will be developed. Novel approaches for the classification of arteries and veins in OCT-A images will be investigated, and different feature selection methods will be explored to cope with the large number of extracted phenotypes. In the next chapter, the first application of this framework is presented to investigate retinal changes in a diabetic cohort.

Chapter 5

OCT-A analysis framework in diabetic retinopathy

5.1 Diabetic retinopathy and OCT-A

Diabetes is a lifelong condition characterised by chronic high levels of glucose in the blood leading to microvascular and macrovascular alterations. Diabetic retinopathy (DR) is a complication of diabetes that affects potentially all people with diabetes resulting in visual impairment or blindness [144]. Thanks to the ability to capture images of the microvasculature in the eye in a fast and non-invasive way, OCT-A technology has recently emerged as an advantageous device to investigate DR. Previous studies have demonstrated the potential of this technology on diabetic cohorts by assessing associations between retinal phenotypes, such as vessel density (VD), fractal dimension (FD) and foveal avascular zone (FAZ) area, with DR severity. Kim *et al.* (2016) [50] reported a negative correlation between VD and FD with disease progression. De Carlo *et al.* (2015) [84] and Takase *et al.* (2015) [51] showed an enlargement of FAZ area in diabetic participants regardless of the presence of retinopathy. Krawitz *et al.* (2017) [36] found an increase in the FAZ acircularity index between controls and DR patients (further details in chapter 2). Albeit promising, these studies were based on a limited number of retinal phenotypes which are not representative of the full spectrum of retinal vascular morphometric characteristics that could be exploited for clinical diagnosis.

More recent studies have further used those retinal measurements to train machine learning models for the automated classification of DR severity. Aslam *et al.* (2020) [79]

proposed a random forest model to distinguish between healthy controls and diabetic patients. To achieve the same classification task Alam *et al.* (2020) [80] and Sandhu *et al.* (2018) [81] used a support vector machine classifier. Finally, a deep learning architecture with a transfer learning approach has been recently proposed by Le *et al.* (2020) [82] to predict diabetic retinopathy patient status from OCT-A images without the requirement of feature engineering. However, despite the popularity of deep learning methods, a drawback is often represented by the impossibility of a straightforward interpretation of results. Therefore, in this work a feature engineering approach is adopted instead.

This chapter's contributions include the first application of the fully automated OCT-A computational framework for the discovery of retinal biomarkers in OCT-A images. The investigation of the reproducibility of previously reported results and the proposal of novel candidate metrics able to capture changes due to diabetes. Machine learning models are implemented for the automated classification of OCT-A images according to disease status. Furthermore, the best classifier built on interpretable retinal vascular characteristics is benchmarked against a deep learning architecture previously proposed for OCT-A classification [82]. The OCT-A computational framework lays out the foundation of future investigations to enable deep microvascular phenotyping and realising the full potential of OCT-A technology. The main findings of this work have been published by Springer International Publishing as proceeding of the 7th MICCAI workshop on Ophthalmic Medical Image Analysis (OMIA7) [6][1].

5.2 Demographics and clinical information

The NHS Lothian cohort is part of an ongoing study at the Royal Infirmary in Edinburgh that aims to characterise the progression of DR in patients with Type 1 diabetes. Participants are divided into three groups according to the type of treatment for diabetes: *basal bolus* is the group of patients taking injections to maintain the blood glucose levels stable, *insulin pump* represents the group of participants using an electronic device to regular the release

[1]This work has been developed in collaboration with Rayna Andreeva and Alessandro Fontanella, DTP students at the School of Informatics of the University of Edinburgh, who have carried out the implementation of the deep learning model VGG16 for OCT-A image classification, and Shareen Forbes and Laura Reid from the Royal Infirmary Diabetes Clinics in Edinburgh, who have designed the cohort study, recruited participants, and collected data for this study.

of insulin in the blood, and *islet transplant* is the group of patients who underwent a surgical procedure to implant healthy beta cells in the pancreas for the production of insulin. A total of twenty-six participants was recruited for the study at the time of the analysis. Retinal fundus photography was used as a diagnostic tool to assess the severity of retinopathy. Table 5.1 shows a summary of the NHS Lothian cohort participants divided by groups and DR diagnosis.

Twenty-five healthy volunteers without ocular diseases were also recruited at the Royal Infirmary in Edinburgh as a control group to assess retinal measurements in the healthy population.

Treatment	Num. of participants	DR
Basal Bolus	5	2
Insulin Pump	16	10
Islet Transplantation	5	1

Table 5.1: Overview of the NHS Lothian cohort.

5.3 Materials and methods

5.3.1 Study protocol

All participants of the NHS Lothian cohort underwent blood testing and eye examinations. HbA1c levels (a blood biomarker for glucose) and blood pressure were annotated. Images of the eye were acquired using fundus photography, OCT, and OCT-A technologies in a quiet, temperature-controlled room in the Queen's Medical Research Institute, Edinburgh using RTVue-XR Avanti (Optovue, Inc., Fremont, CA). Only one eye, randomly chosen between right (OD) or left (OS) to avoid potential laterality confounders [145], was included in the study. Information about treatment was discarded for the purpose of this work, and participants were divided in two groups, diabetic patients without retinopathy (NoDR), and diabetic patients with retinopathy (DR). An overview of the demographic data and OCT-A scans can be found in table 5.2.

	Controls	NoDR	DR
Age (mean ± SD)	46.2 ± 10.7	42.8 ± 10.3	49.3 ± 15.5
Gender (M/F)	13/12	5/7	9/5
Eye (OD/OS)	13/12	8/4	7/7

Table 5.2: Demographic information.

5.3.2 Image processing

OCT-A vessel segmentation was performed using the U-Net neural network architecture which has been proven to achieve the best segmentation performance (*i.e dice score*) and the lowest error in retrieving the FAZ area, as previously shown in chapter 3. Segmentation and binarisation were performed on the maximum projection (*enface*) obtained using the superficial vascular plexus (SCP) and deep capillary plexus (DCP) scans, and the SCP image, separately. Skeletonisation was then performed to obtain the final vascular networks (as described in chapter 4). Finally, the *enface* vascular graph was used for FAZ detection and the SCP vascular graph was divided into the five regions of interest (ROIs), foveal, nasal, inferior, temporal, superior, to extract the retinal phenotypes. Figure 5.1 outlines the image processing pipeline.

5.3.3 Statistical analysis

Hypothesis tests are statistical tools widely used for assessing whether there is an association between two or more variables. They have been extensively applied to investigate retinal phenotypes in many systemic diseases including comparisons between diabetic and control groups [48], [51], [84] (see section 2.7.1). In this study, one-way analysis of variance (ANOVA) was firstly used to investigate the three groups comparison in variables normally distributed. Whereas the non-parametric Kruskal-Wallis test was applied in variables not satisfying the Shapiro-Wilk normality test. Then, pairwise comparisons (DRvsH, NoDRvsH, and NoDRvsDR) were also performed using either *t*-test or Mann-Whitney-Wilcoxon test according to the distribution of each variable to explore in detail difference between groups. Bonferroni correction was applied to account for multiple comparisons. Statistical analysis was implemented in R version 3.6.3 (2020-02-29).

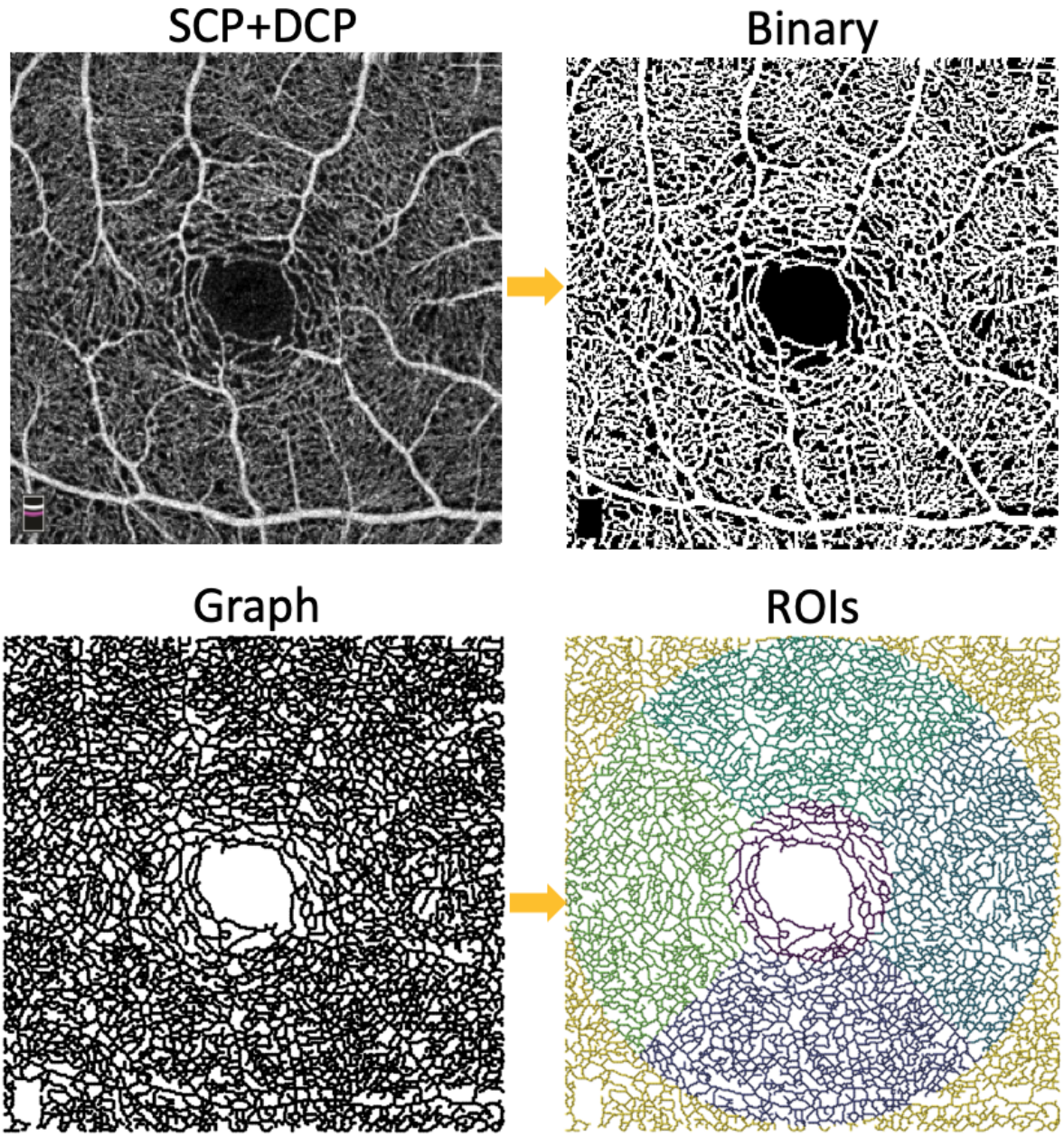

Figure 5.1: Image processing pipeline for the OCT-A scan obtained as maximum projection of the SCP and DCP scans (different layers are marked in the scan logo at the bottom of the image).

5.3.4 Predictive models

After removing highly correlated metrics, different prediction models were compared to establish the best classifier among logistic regression (LR), *k*-nearest neighbors (*k*-NN), support vector machine (SVM), and random forest (RF). An initial analysis was performed using all retinal features extracted using the OCT-A network analysis framework to train each machine learning model. However, considering the large number of features and the small sample size of the study, a second analysis was carried out by performing feature selection, using a smaller subset of features (~5% of the starting variables) to limit the *peaking phenomenon* discussed in chapter 4. Mutual information (MI), a filter method for feature selection (see appendix A, was used to retrieve the 30 most informative retinal phenotypes. Given the small sample size and the requirement of the models for hyperparameter tuning, nested cross-validation (CV) was employed to allow the calibration of hyperparameters preventing leakage of information from the test set. A ten-fold CV was used as outer loop and a five-fold CV as inner loop inside the *GridSeach* algorithm to find the optimal hyperparameters for each model. An overview is shown in figure 5.2. Finally, the best classifier was compared to the deep learning approach based on OCT-A images for DR classification: a convolutional neural network VGG16 for OCT-A classification proposed by Le *et al.* [82]. Transfer learning was used to overcome the small sample size issue. This approach involves the pretraining of the network with images from a different dataset (ImageNet [146]) to retrieve weights of the bottom layers and the re-training only of the last convolutional layers to achieve faster learning. Only the last seven layers convolutional were fine-tuned as in Le *et al.* (2020) [82]. Root mean square propagation (RMSprop) optimizer was used during the learning process. VGG16 was evaluated on the same set of OCT-A images using the same ten-fold CV approach. Data augmentation (selected zoom in the range [0.8, 1.2] and rotations up to 40°) was used to achieve better performances (further details can be found in [147]). Finally, accuracy, sensitivity, specificity, and area under the receiver operating characteristic (ROC) curve (AUC) were reported for performance evaluation as the average of the scores in each fold. Python 3.6.9 was used to build ML methods.

5.4 Results

5.4.1 Replication of previous results and novel biomarkers

Statistical analysis showed that among the 744 retinal candidate biomarkers 189 were statistically significant considering all pairwise group comparisons. The majority of features, 79, were graph-based, followed by 67 topology-based, 28 coordinate-based, and 15 flow-based (figure 5.8). Figure 5.3A-C displays three retinal features of interest previously reported [50], [51]: number of nodes, which is a surrogate to the previously reported vessel skeleton density metric (since nodes represent pixels in the skeleton); the number of intercapillary spaces and their average size. These metrics capture global features of the retinal plexus and can be used for initial clinical inspections. Interestingly, these three metrics showed monotonic trends (either decrease or increase) going from Controls to NoDR, and eventually DR. These network properties highlight how NoDR appears as an intermediate stage between Controls and DR. Figure 5.4A-C shows local structural features potentially helpful in identifying differences between healthy controls and NoDR. The shape of intercapillary space in the nasal segment, the newly proposed flow metric, $a2f$, which describes the ratio between intercapillary space areas and the capacity of the vessels surrounding them, and the size of the intercapillary spaces around the FAZ, may be features able to characterise first changes in the vasculature due to diabetes and early onset of retinopathy. Finally, despite the FAZ area and the acircularity index were increased (as previously reported [36], [41], [48]), along with the overall tortuosity, after the Bonferroni correction, the adjusted p-values were not statistically significant (figure 5.5A-C). Tables with significant p-values can be found in Appendix D.

5.4.2 Predictive models identify DR status

Table 5.3 shows the performances obtained for each class of this cohort, Control, NoDR, DR, using all retinal phenotypes. Models showed similar trends in performances. All classifiers consistently achieved the best accuracy and AUC score in predicting participants with DR, suggesting that changes in the retinal microvasculature were more prominent in DR participants. Whereas, NoDR patients were the most challenging to identify. Models performed poorly in this class, highlighting the challenge in detecting

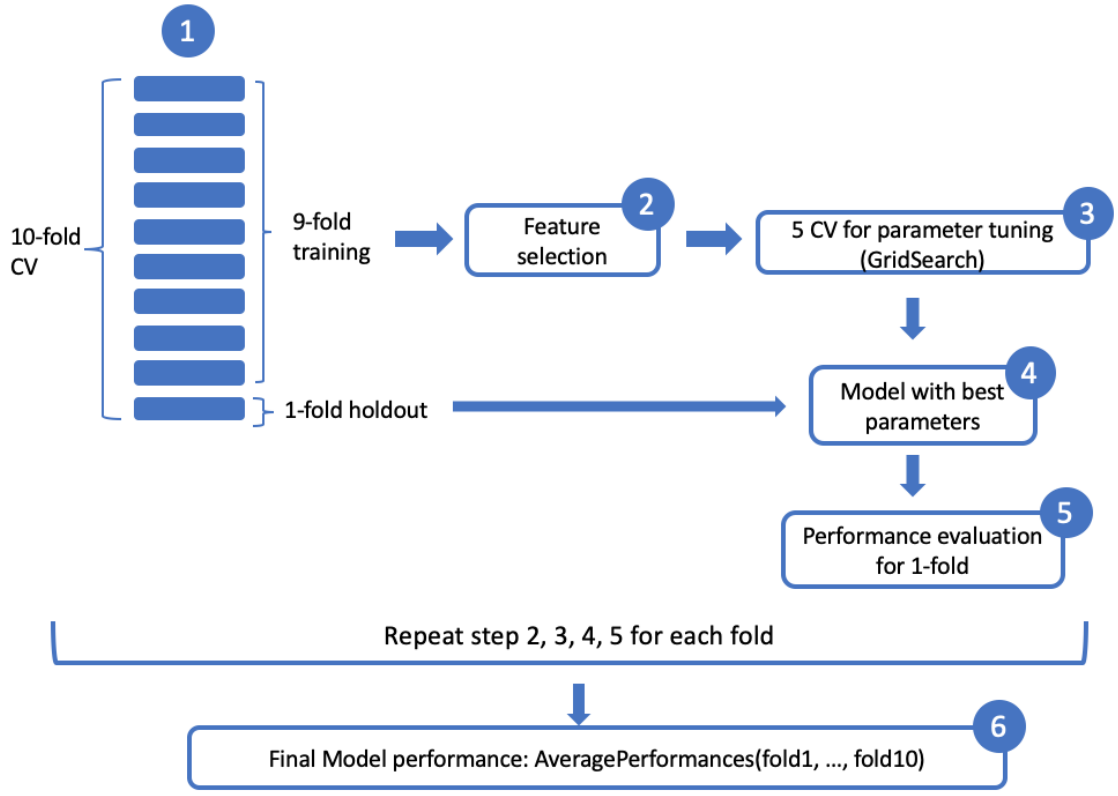

Figure 5.2: Overview of the nested cross-validation and performance evaluation.

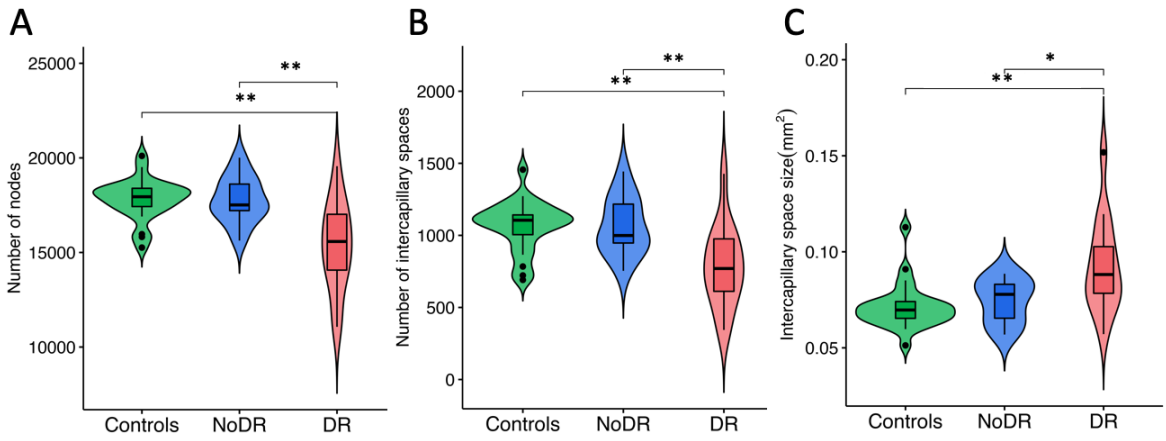

Figure 5.3: Violin plots of significant retinal features between healthy and DR, and NoDR and DR (*:p-value<0.01, **:p-value<0.001). (A) number of nodes, (B) number of intercapillary spaces, (B) size of intercapillary spaces in the vascular network.

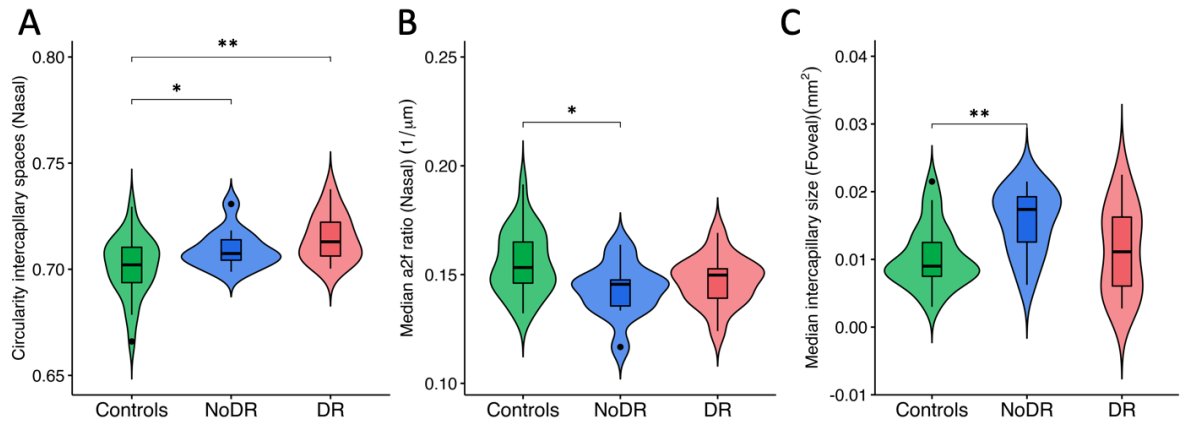

Figure 5.4: Violin plots of significant retinal features between healthy and NoDR (*:p-value<0.01, **:p-value<0.001). (A) circularity of intercapillary spaces in the nasal segment, (B) area to perimeter flow ratio (a2f) in the nasal segment, and (C) size of intercapillary spaces in the foveal region.

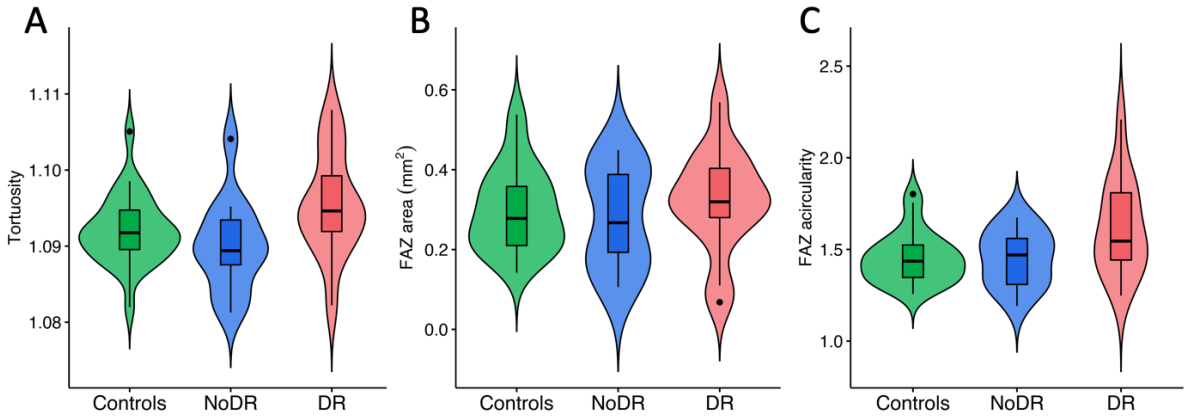

Figure 5.5: Violin plots of features that were not significant after the Bonferroni correction. (A) tortuosity, (B) FAZ area, and (C) FAZ acircularity.

Class	Score	k-NN	LR	SVM	RF
Control	**ACC** (mean ± SE)	0.51±0.06	**0.72±0.05**	0.59±0.06	**0.72±0.03**
	SEN (mean ± SE)	0.51±0.05	0.66±0.05	0.53±0.07	**0.65±0.03**
	SPE (mean ± SE)	0.20±0.08	**0.50±0.08**	0.30±0.07	0.48±0.06
	AUC (mean ± SD)	0.61±0.13	0.70±0.14	0.70±0.16	**0.77±0.09**
DR	**ACC** (mean ± SE)	0.76±0.06	0.84±0.04	0.84±0.03	**0.86±0.09**
	SEN (mean ± SE)	0.30±0.15	0.55±0.15	0.50±0.16	**0.60±0.14**
	SPE (mean ± SE)	0.95±0.05	0.96±0.03	**1.00±0.00**	0.96±0.03
	AUC (mean ± SD)	0.70±0.30	**0.84±0.23**	0.72±0.32	0.80±0.27
NoDR	**ACC** (mean ± SE)	0.71±0.03	0.73±0.03	0.67±0.04	**0.79±0.03**
	SEN (mean ± SE)	0.00±0.00	0.10±0.09	0.00±0.00	**0.2±0.12**
	SPE (mean ± SE)	0.93±0.04	0.93±0.04	0.88±0.05	**0.98±0.02**
	AUC (mean ± SD)	0.50±0.25	0.52±0.37	0.25±0.25	**0.51±0.36**
	Overall AUC	0.67	0.75	0.72	**0.80**

Table 5.3: Table of classification performances for each model using all retinal features.

participants with diabetes without overt retinopathy signs. Among all models, RF classifier achieved the best accuracy in each of the classes and the best overall AUC score (0.80). LR reached nearly-comparable performance achieving AUC score equal to 0.75. SVM and *k*-NN models yielded good accuracies in DR classification, however, poor performances were obtained in the classification of the other two classes. ROC curves and AUC scores for each of the methods are shown in figure 5.6.

5.4.3 Feature selection and interpretability

In the second analysis, feature selection was applied prior to training. All classifiers achieved similar or better performances than models trained using all the extracted retinal features (table 5.4). Albeit DR class remained the class with the highest accuracies, using feature selection, an improvement in performances of each classifier was also reached in the Control and NoDR classes. *k*-NN and LR reach similar performance in each group, whereas RF achieved slightly better accuracies than SVM, and the highest AUC score (0.84). Figure 5.7 shows the ROC curve for each class by using the different models.

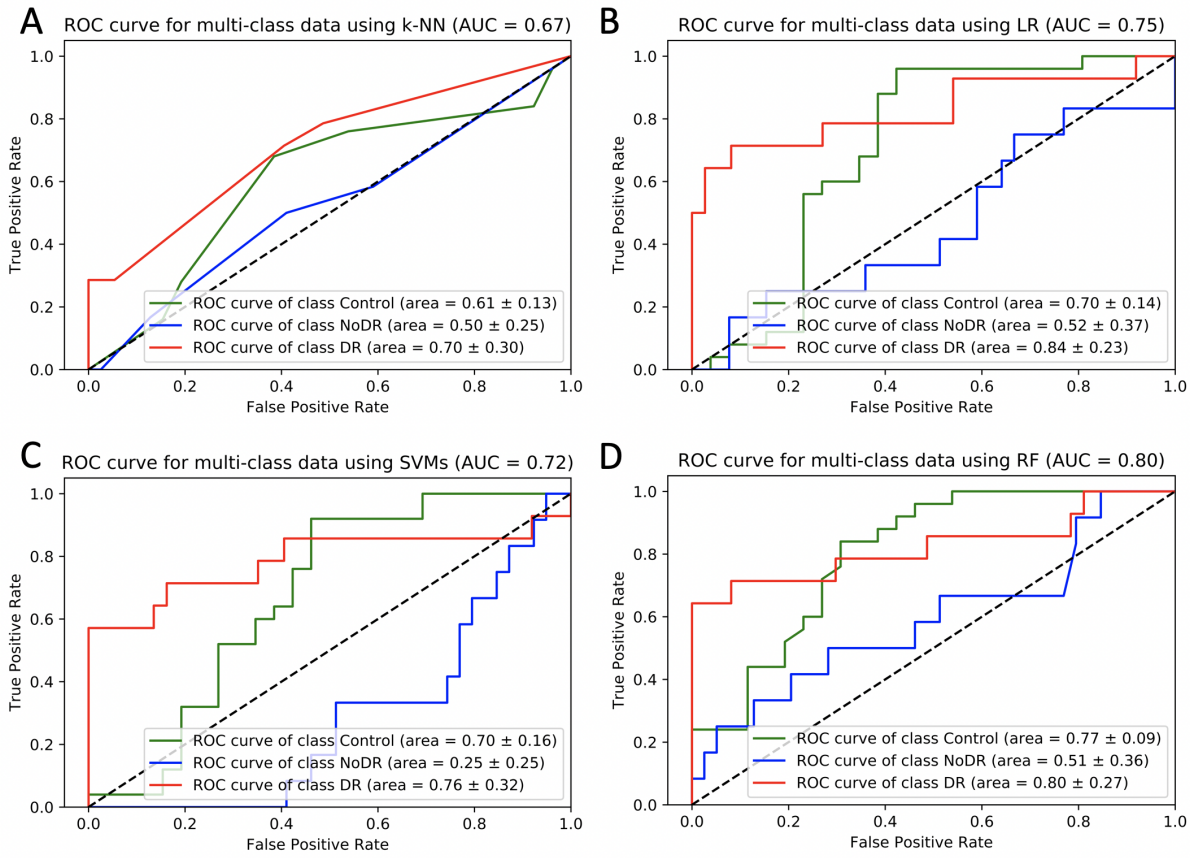

Figure 5.6: ROC curves for each class using (A) *k*-NN, (B) LR, (C) SVM, and (D) RF.

Class	Score	k-NN	LR	SVM	RF
Control	**ACC** (mean ± SE)	0.65±0.05	0.64±0.05	0.73±0.04	**0.80±0.07**
	SEN (mean ± SE)	0.62±0.07	0.63±0.05	0.68±0.05	**0.79±0.08**
	SPE (mean ± SE)	0.53±0.07	0.45±0.11	0.58±0.06	**0.77 ± 0.08**
	AUC (mean ± SD)	0.60±0.23	0.62±0.16	0.69±0.14	**0.90±0.11**
DR	**ACC** (mean ± SE)	0.81±0.05	0.76±0.04	**0.84±0.06**	0.82±0.06
	SEN (mean ± SE)	0.55±0.16	0.45±0.13	**0.60±0.16**	0.55±0.19
	SPE (mean ± SE)	**0.98±0.02**	0.88±0.04	0.95±0.03	0.88±0.05
	AUC (mean ± SD)	0.76±0.22	0.70±0.37	0.71±0.33	**0.81±0.12**
NoDR	**ACC** (mean ± SE)	0.70±0.05	0.73±0.04	**0.77±0.05**	0.75±0.08
	SEN (mean ± SE)	0.28±0.12	0.05±0.05	0.25±0.13	**0.30±0.10**
	SPE (mean ± SE)	0.81±0.07	**0.93±0.05**	0.90±0.05	0.88±0.05
	AUC (mean ± SD)	0.63±0.25	0.50±0.40	0.59±0.37	**0.67±0.37**
	Overall AUC	0.68	0.69	0.74	**0.84**

Table 5.4: Table of classification performances in DR study using feature selection.

Table 5.5 reports the most frequent features selected for each fold of the CV by using the mutual information criterion. The majority of features were coordinate-based metrics which describe structural characteristics of the microvasculature. Topology-based features such as graphlet counts and random walk distance were also frequently selected, along with graph density and edges radius, part of the graph-based metrics. Only two of the flow-based metrics, mean resistance in the inferior segment and the median value of the area to capacity flow ratio (a2f), were included.

Finally, the best classifier among the machine learning models previously evaluated was compared to the deep learning architecture VGG16 with transfer learning. Using the same set of images and CV approach for model evaluation, the results showed that the best model, the RF classifier, trained on interpretable retinal features, achieved better performances for each class than the neural network approach (table 5.6).

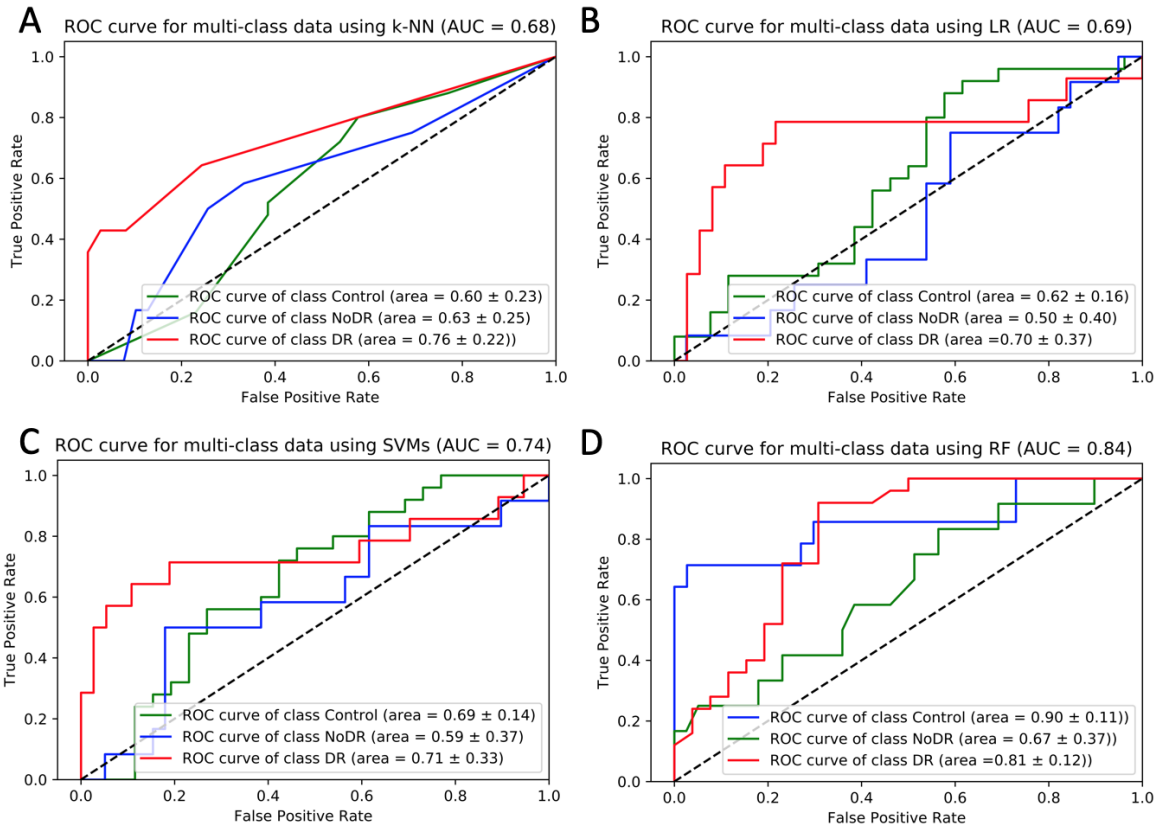

Figure 5.7: ROC curves for each class using (A) k-NN, (B) LR, (C) SVM, and (D) RF.

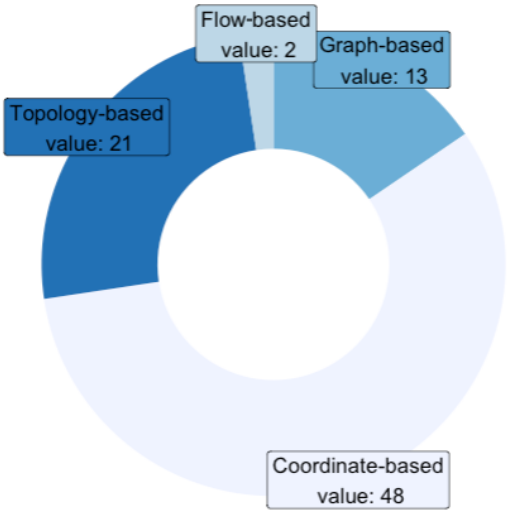

Figure 5.8: Classes of features selected for classification.

Retinal phenotype	frequency (CV)
Number of intercapillary spaces (S)	10/10
Median perimeter space (I)	10/10
Graph density (S)	10/10
Kurtosis curvature (N)	10/10
Mean path tortuosity (T)	10/10
Std path tortuosity (T)	10/10
Mean perimeter spaces (S)	9/10
Std intercapillary space area (S)	9/10

Table 5.5: Most frequent selected features using mutual information criterion within each fold of the 10-fold cross validation.

Class	Score	RF	VGG16
Control	**ACC** (mean ± SE)	0.80±0.07	0.78±0.05
	SEN (mean ± SE)	0.79±0.08	0.90±0.05
	SPE (mean ± SE)	0.77±0.08	0.67±0.11
	AUC (mean ± SD)	0.90±0.11	0.90±0.15
NoDR	**ACC** (mean ± SE)	0.75±0.08	0.72±0.04
	SEN (mean ± SE)	0.30±0.10	0.20±0.13
	SPE (mean ± SE)	0.88±0.05	0.88±0.05
	AUC (mean ± SD)	0.67±0.37	0.67±0.28
DR	ACC (mean ± SE)	0.81±0.05	0.76±0.04
	SEN (mean ± SE)	0.55±0.16	0.45±0.13
	SPE (mean ± SE)	0.98±0.02	0.88±0.04
	AUC (mean ± SD)	0.76±0.22	0.70±0.37
	Overall AUC	*0.84*	0.79

Table 5.6: Comparison of random forest classifier and VGG16+TL.

5.5 Discussion

OCT-A technology is predominately emerging as a retinal imaging modality for many ocular diseases. Among those, diabetic retinopathy, a complication of diabetes mellitus, has been the centerpiece of the many OCT-A based studies with the aim of investigating retinal microvascular changes to provide a non-invasive alternative to characterise vascular dysfunctions and gain valuable insights for clinical practice. This chapter proposed the first application of the OCT-A computational framework for the characterisation of the retinal vasculature in patients with diabetes. Associations between changes in retinal measurements and disease severity were explored to validate previously reported results, such as the decrease of vessel skeleton density, and to report novel candidate biomarkers that can help in clinical applications. Furthermore, several machine learning models were trained to identify patient status based of the retinal features extracted using the OCT-A computational framework. The problem of “peaking phenomenon" was addressed by comparing models with and without feature selection.

Finally, results showed that the best model, the RF classifier, outperformed the deep learning architecture, VGG16, without compromising features interpretability.

Limitations of this study include the small sample size and the use of OCT-A images with $3 \times 3\ mm^2$ field of view which capture only a small portion of the retinal landscape. It is worth mentioning that this work does not investigate early signs of retinopathy since DR severity is not used to classify participants. Furthermore, changes captured using OCT-A technology and associated with DR are not adjusted for possible confounding factors. It is also acknowledged that whereas there is overlap between the manifestations of diabetic retinopathy in the retina and the characteristics that OCT-A may acquire, the coincidence is not complete. Indeed, DR diagnosis is currently based on damage observed in fundus images (*e.g.*, cotton wool spots, further details in 2.7), which might not be captured by OCT-A scans.

Future work should investigate more advanced feature selection approaches, such as wrapper methods or genetic algorithms, to leverage the large number of biomarkers [148]. Further analysis of the NHS Lothian cohort will involve the inclusion to common risk factors for the progression of DR, *e.g.*, duration of diabetes, age, high blood pressure, poor glycaemic control and microalbuminuria, and the further analysis based on the three different types of treatment. Despite the small sample size of this dataset, the OCT-A framework demonstrates great potential in identifying novel retinal biomarkers for onset of diabetic retinopathy. Early identification of these alterations can contribute to timely target patients at risk and effectively monitoring disease progression. The chapter that follows presents a second application of this framework to a systemic disease with a retinal vascular footprint: chronic kidney disease.

Chapter 6

OCT-A analysis framework in chronic kidney disease

6.1 Chronic kidney disease and OCT-A

Chronic kidney disease (CKD) describes a group of conditions characterised by the progressively decline in kidney function. It has been estimated that it affects the ~10% of population worldwide and this number is forecast to increase [2]. Its aetiology is still under investigation, however, preliminary studies have reported that vascular alterations, caused by endothelial dysfunction, hormonal imbalance, and oxidative stress may play a crucial role in CKD pathology [66], [149], [150]. Moreover, evidence suggests that prolonged kidney dysfunction may affect also extra-renal vasculature, increasing the risk of cardiovascular disease, a leading cause of mortality in patients with CKD [151], [152]. Retinal imaging offers a unique opportunity to visualise the cardiovascular system *in vivo* and investigate early changes in the vasculature that may contribute to prognostic indications on the progression of CKD and timely target patients at higher risk of cardiovascular disease. The kidney and the eye share remarkably similar microvascular structures and physiological mechanisms. Diseases of the two organs have been closely linked [153]. Earlier studies have reported changes in the vasculature of the eye captured using fundus imaging: focal arteriolar narrowing, decrease in fractal dimension, arteriovenous nicking and opacification. [154], [155]. However, changes at the capillary level have been underexplored. With the advent of OCT-A technology, a growing number of publications focusing on microvasculature changes in patients with CKD have emerged.

Wu *et al.* [69] reported a decrease in vessel density (VD) in the superficial capillary plexus (SCP) in patients with CKD. Similar results were found by Yeung *et al.* [68] and in both SCP and deep capillary plexus (DCP), and an increase in foveal avascular zone (FAZ) acircularity index in subjects suffering from CKD compared to healthy subjects. Vadalà *et al.* [67] showed reduced VD in both foveal and parafoveal regions of the retina in patients with hypertension and kidney impairment. These promising results are, however, based on the most common retinal OCT-A measurements and changes in these metrics are shared by many comorbidities (hypertension, diabetes, etc,..).

This chapter proposes the application of OCT-A network analysis framework to investigate changes in retinal vascular phenotypes in patients suffering from CKD with the aim to unravel novel CKD-targeted candidate biomarkers. Contributions of this chapter include the investigation of retinal microvascular changes in patients with CKD, and the classification, for the first time, of participants suffering from CKD using machine learning methods and OCT-A retinal features. The main findings of this work have been published by Springer International Publishing as proceeding of the 7th MICCAI workshop on Ophthalmic Medical Image Analysis (OMIA7) [6][1].

6.2 Materials and methods

6.2.1 Study Protocol and clinical information

Participants with CKD were identified from the Royal infirmary of Edinburgh department of nephrology between 01/01/2017 and 01/03/2020. CKD was defined according to the Kidney Disease Outcome Quality Initiative (K/DOQI) classification [156]. Age- and sex-matched healthy volunteers without comorbidity were recruited from the community. Participants with current or pre-existing eye disease, eye surgery, diabetes mellitus, and body mass index (BMI) >35 kg/m^2 were excluded.

Twenty-five patients with CKD and twenty-five healthy controls were included in the study. Table 6.1 shows demographic information of participants in this cohort. OCT-A

[1]This work has been developed in collaboration with Rayna Andreeva and Alessandro Fontanella, DTP students at the School of Informatics of the University of Edinburgh, which have carried out the construction of the deep learning model VGG16 for OCT-A image classification, and Neeraj Dhaun, Dan Pugh and Tariq Farrah, from the Department of Renal Medicine, Royal Infirmary of Edinburgh who have designed the cohort study, recruited participants, and collected data for this study.

images were acquired in a quiet, temperature-controlled room in the Queen's Medical Research Institute, Edinburgh, using RTVue-XR Avanti (Optovue, Inc., Fremont, CA). Systolic and diastolic blood pressure, height, and weight were also recorded. Creatinine clearance was used as an estimate of the glomerular filtration rate GFR calculated according to the Chronic Kidney Disease Epidemiology Collaboration (CKD-EPI) equation. Where possible, at least 24 hours were given to participants to consider the study information prior to providing informed consent. Ethical approval was provided by the South East Scotland Research Ethics Committee and the study is registered on clinicaltrials.gov (NCT02132741).

	Controls	**CKD**
Age (mean $\pm$ SD)	46.2 ± 10.7	49.4 ± 13
Gender (M/F)	13/12	13/12
Eye (OD/OS)	13/12	13/12

Table 6.1: Demographic data.

6.2.2 Image processing and statistical analysis

Similar to the procedure described in section 5.3.2, OCT-A images of only one eye, randomly chosen to avoid laterality confounders, were analysed. SCP and *enface* scans were segmented using a U-Net deep neural network architecture. After skeletonisation and graph construction, the OCT-A computational framework was utilised to extract the four types of retinal features characterising the vascular network (as described in chapter 4). Statistical tests were employed to discover associations between retinal vascular phenotypes and patient status. Pairwise comparisons were performed using either a Student's *t-test* or Mann-Whitney-Wilcoxon test according to the distribution of each variable.

6.2.3 Predictive models

Machine learning (ML) models were applied to identify patient status. Four predictive models, logistic regression (LR), *k*-nearest neighbors (*k*-NN), support vector machine

(SVM), and random forest (RF) classifiers were investigated to assess the best method to detect patients with CKD. To reduce the large amount of variables, before training the models, highly correlated features were removed (Pearson correlation coefficient greater than 0.95) metrics. Ten-fold cross-validation (CV) was performed to evaluate model performance. Given the large amount of features and the small number of data points, to avoid the *peaking phenomenon*, feature selection (FS) was performed using a filter method based on the p-values of the statistical tests previously described. FS was carried out in each fold of the cross-validation to avoid leakage of information from the holdout set. Hyperparameter tuning was performed using the *GridSeach* algorithm which exploits different combination of parameters and chooses the configuration that achieves the best accuracy score in a inner five-fold cross-validation. Finally, a comparison between ML classifiers, built using the extracted retinal features, and the deep learning model, VGG16, previously used to classify diabetic retinopathy (see chapter 5.3.2), is presented. Further details about the deep learning architecture can be found in section 5.3.4. accuracy, sensitivity, specificity, and area under the receiver operating characteristic (ROC) curve (AUC) scores were reported for performance evaluation as average of the scores in each fold.

6.3 Results

Statistical analysis reported 43 retinal significant features ($p<0.05$), including 10 graph-based metrics, 20 coordinate-based metrics, 10 topology-based metrics, and 3 flow-based metrics (figure 6.5). Among those, novel metrics previously unexplored were reported in patients with CKD. This group of participants showed high variability in the curvature of FAZ contour (figure 6.1A), larger values of vessel radius in the temporal region (figure 6.1B), and lower area to flow capacity ratio (a2f) in the same region, a newly proposed metrics, underlining the strong connection between structural and functional changes (figure 6.1C). Although not statistically significant, in line with other studies [67], [68], a reduction in vessel skeleton density (number of nodes in the graph) and an increase in FAZ area and acircularity index were found in patients with CKD (figure 6.2A-C). A decrease in the number of intercapillary spaces in the whole image, an enlargement of

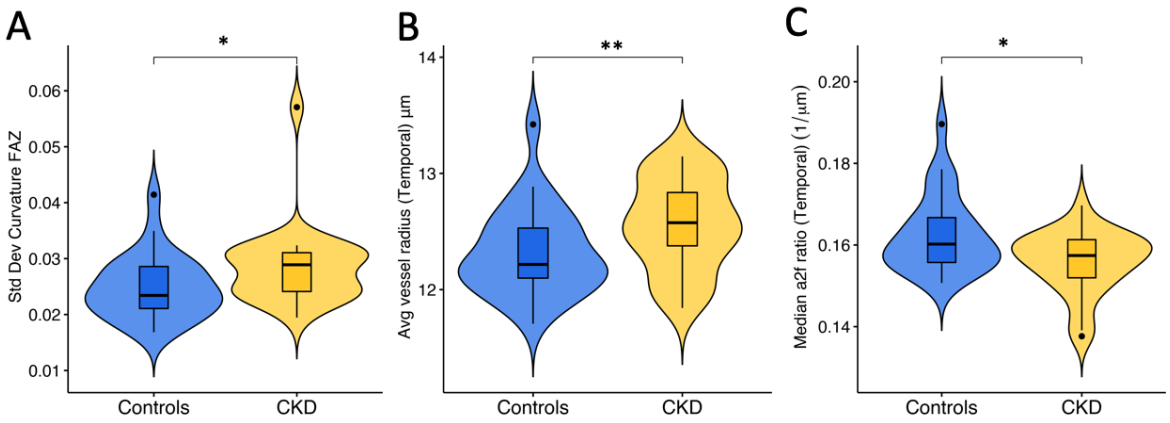

Figure 6.1: (A) Standard deviation of FAZ contour curvature. (B) Vessels radius (T). (C) Area to flow capacity ratio (T).

intercapillary spaces in the foveal region, and an increase in the curvature in the whole vascular network were also reported (figure 6.3A-C). Accuracy, sensitivity, and specificity for each model are reported in table 6.2. Performances of each predictive model presented high variability across folds of the cross-validation (figure 6.4). LR, RF, and *k*-NN classifiers achieved AUC scores slightly above classification by chance. Both SVM and VGG16, the best classifiers, performed poorly in the classification task, achieving the same AUC score (0.62), confirming the difficulty in identifying patients with CKD. This highlights that the detection of patients with disease that affects undirectly the eye is a more challenging classification task and retinal changes could be perceived clinically as much more subtle. Investigating features selected in each fold of the cross-validation, a high number of both coordinate-based and topology-based features were selected, 33 and 28, respectively. Graph-based metrics, including average nodes degree and edges radius, were also often chosen. Finally, 6 flow-based metrics involving vessel resistance and the area to flow capacity ratio were among the features most used by classifiers (table 6.3).

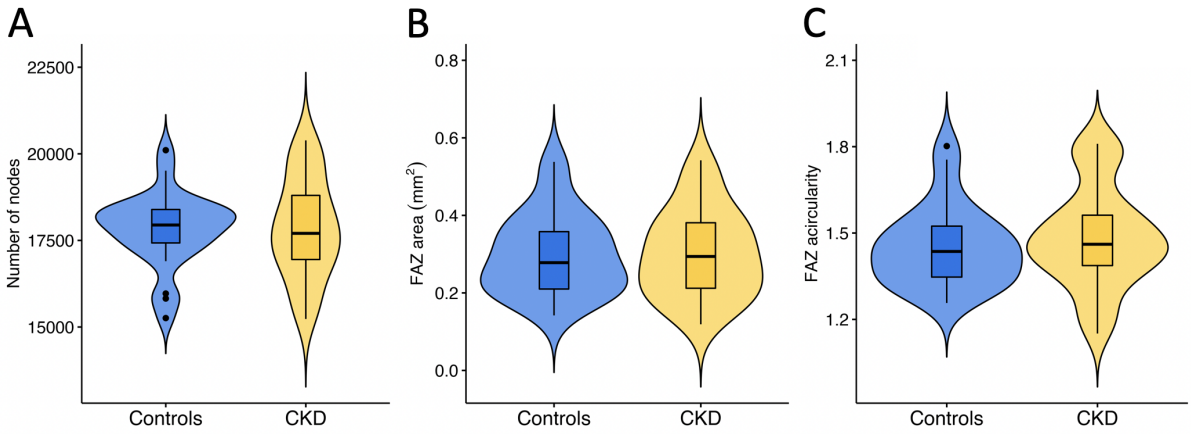

Figure 6.2: (A) Number of nodes in the network. (B) FAZ area. (C) FAZ acircularity.

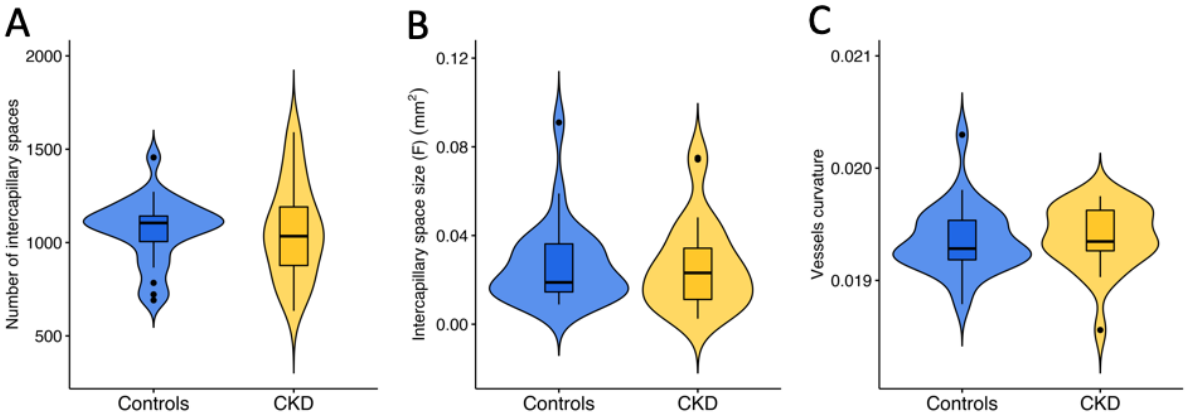

Figure 6.3: (A) Number of intercapillary spaces. (B) Average intercapillary space size in the foveal region. (C) Vessel curvature (whole image).

Classifier	Accuracy	Sensitivity	Specificity	AUC
KNN	**0.56±0.06**	**0.72±0.08**	0.45±0.08	0.60±0.19
LR	0.46±0.06	0.55±0.12	**0.58±0.13**	0.58±0.13
RF	0.54±0.06	0.63±0.11	0.48±0.10	0.52±0.20
SVMs	0.52±0.09	0.58±0.14	0.47±0.15	**0.62±0.29**
VGG16	0.48±0.08	0.61±0.09	0.38±0.12	**0.62±0.37**

Table 6.2: Table of classification performances in CKD study.

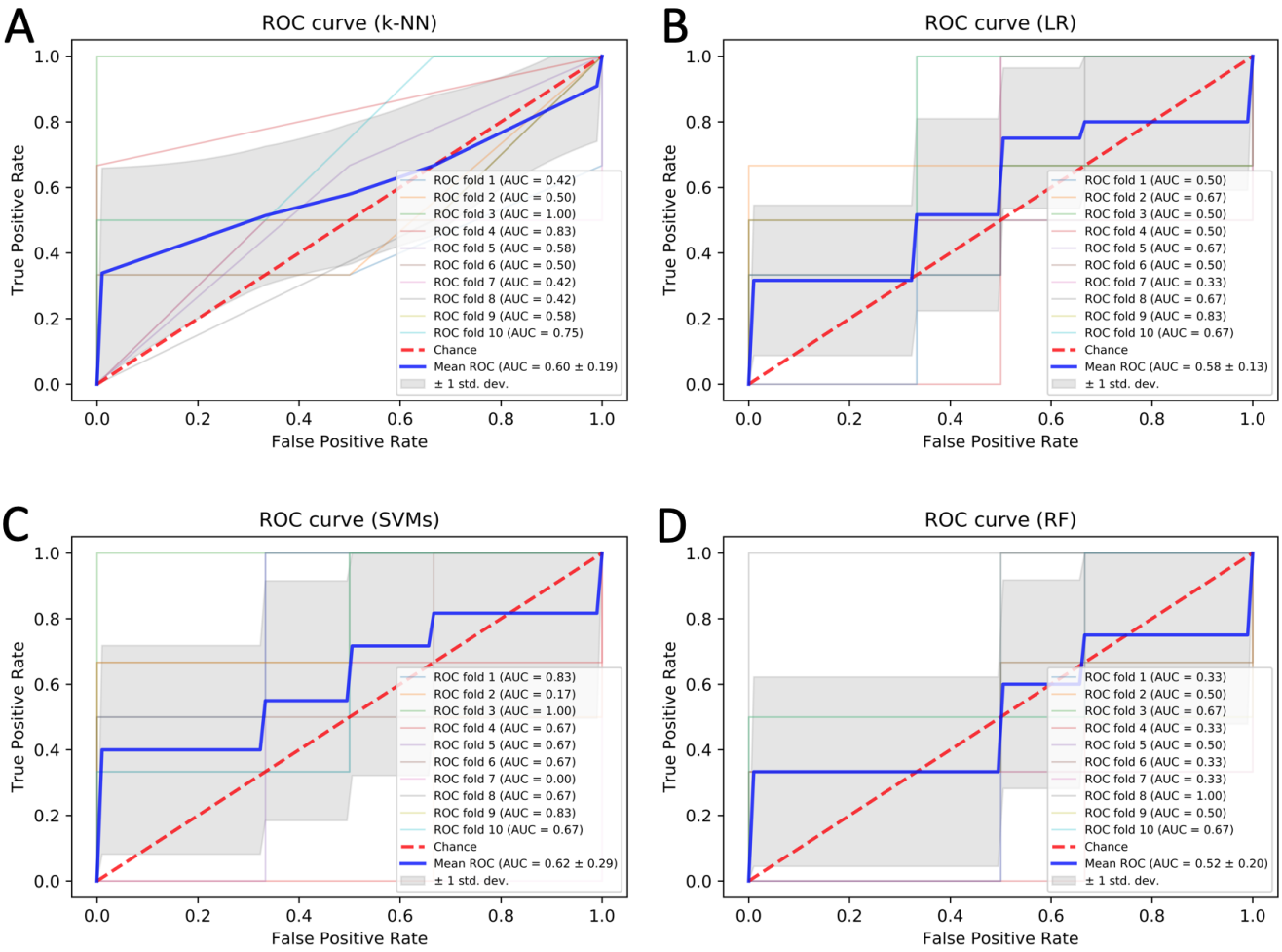

Figure 6.4: ROC curves for each fold of the CV using (A) k-NN, (B) LR, (C) SVMs, and (D) RF.

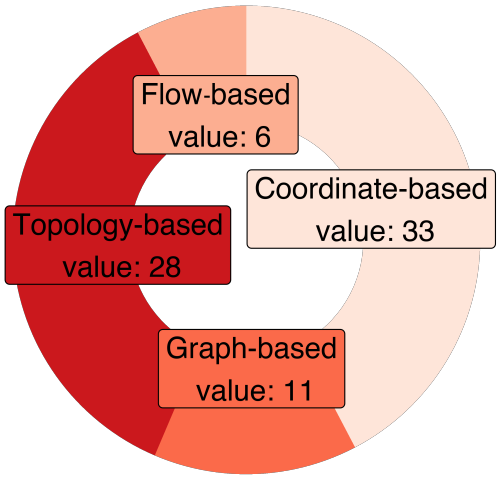

Figure 6.5: Classes of features selected for classification.

Retinal phenotype	frequency (CV)
Std dev tortuosity (W)	10/10
Std dev random walk lengths (W)	10/10
Skw circular areas ratio (T)	10/10
Median a2f (T)	10/10
Std dev circular areas ratio (S)	10/10
Std dev FAZ curvature	10/10
Std tortuosity (I)	10/10
Intercapillary space count (F)	10/10
Graphlet 7 count (F)	10/10

Table 6.3: Most frequent selected features using statistical tests within each fold of the 10-fold cross-validation (std dev: standard deviation, skw: skewness.

6.4 Discussion

Chronic kidney disease is a condition with a retinal vascular footprint. Previous studies have linked the eye and the kidney by reporting ocular damages in patients with CKD [153]. This chapter described the application of the OCT-A computational framework for the extraction of candidate biomarkers able to characterise retinal microvascular changes in patients with CKD. Previously reported results, such as decrease in vessel skeleton density and increase in FAZ area and acircularity, although not statistically significant, were found in the CKD group compared to healthy subjects. High variability in the FAZ contour, increase vessel radius in the temporal region, and functional changes in the newly proposed area to flow capacity ratio were also found in patients with CKD. Both ML models and the deep learning architecture performed poorly in each evaluation metric, suggesting that automated identification of patients with diseases affecting undirectly the eye using retinal phenotypes is a more complicated task than diabetic retinopathy shown in chapter 5. Limitations of this study include the small sample size, the use of OCT-A images acquired by a specific device and with 3×3 mm^2 field of view. Furthermore, associations are not taking into account important covariates such as age, sex, and blood pressure. Future works will involve the validation of these results on larger cohorts, the

correction of statistical analysis by possible confounding factors, and the exploration of cutting-edge methods to perform feature selection and exploit the potential of novel retinal phenotypes. The next chapter continues investigating CKD and the application of retinal phenotypes for risk assessment in living kidney donors.

Chapter 7

Long-term risk assessment of kidney donation

7.1 Chronic kidney disease and kidney donation

In the previous chapter, chronic kidney disease (CKD) has been described as the condition where the normal function of the kidney is impaired. It may gradually lead to end-stage kidney disease (ESKD), when the clinical biomarker of kidney function, the estimated glomerular filtration rate (eGFR), drops below the 10%. A transplant is generally accepted as the optimal treatment option since its association with better quality of life, longer survival rate, and reduced medical costs compared to a lifetime of dialysis. In 2008, the World Health Organization (WHO) has estimated that 46% of worldwide kidney transplants are from living donors [157]. This has brought attention to the importance of rigorous guidelines for the selection of candidate donors and the investigation of better evaluation methods for long-term risk assessment in kidney donation. Currently, no clear consensus has been found in the literature, and concerns on the long-term risks of living kidney donation have been raised. Indeed, earlier studies have reported no difference in survival rate and risk of ESKD between donors and the healthy population [158], [159], suggesting no medical repercussion for those who have donated a kidney. Contrarily, more recent works have shown evidence of increasing ESKD and cardiovascular risks [160], with first changes in blood biomarkers 15 years after donation [160], [161], when changes in lifestyle and early treatments may be too late. To date, it is not clear how to predict lifetime risk of a kidney transplant and identify those donors at risk. This may

have a significant impact on the long-term risk assessment of kidney donation. As previously described in chapters 2 and 6, the eye shares similar structural and genetic pathways with the kidney, and malfunctions of the latter can manifest as ocular dysfunctions [2]. Hence, in this chapter, it is hypothesised that after nephrectomy, donors may present similar microvasculature changes as patients suffering from CKD and retinal imaging may be a candidate diagnostic tool to gain insights into the timing of vascular changes. This chapter contributes to the advance of our understanding of long-term risk assessment in kidney donation. For the first time, cross-sectional and longitudinal analyses of OCT-A microvascular phenotypes are proposed to characterise changes in living kidney donors. Although preliminary and part of an ongoing study, this research is a first step towards the revealing of the potential of retinal biomarkers in the risk-benefit assessment of kidney transplantation and in targeting donors at risk[1].

7.2 Materials and methods

7.3 Study protocol and data demographics

The same scanning protocol was used for both cross-sectional and longitudinal studies. OCT-A images were acquired at the Queen's Medical Research Institute, Edinburgh, using RTVue-XR Avanti (Optovue, Inc., Fremont, CA). Systolic and diastolic blood pressure, height, and weight were recorded. Creatinine clearance, as an estimate of glomerular filtration rate (GFR), was computed according to the Chronic Kidney Disease Epidemiology Collaboration (CKD-EPI) equation. Ethical approval was provided by the South East Scotland Research Ethics Committee and the study is registered on clinicaltrials.gov (NCT02132741). Thirty kidney donors and thirty patients with CKD were identified from the Royal infirmary of Edinburgh department of nephrology. CKD was defined according to the Kidney Disease Outcome Quality Initiative (K/DOQI) classification [156]. Overall, kidney donors did not have eGFR impairment diagnostic of CKD, or overt cardiovascular disease (CVD). Thirty age- and sex- matched healthy volunteers were recruited from the community. Patients with current or pre-existing eye

[1]This chapter is part of an ongoing research developed in collaboration with Neeraj Dhaun, Dan Pugh, and Tariq Farrah from the Department of Renal Medicine, Royal Infirmary of Edinburgh, Edinburgh, UK.

disease, previous eye surgery, diabetes mellitus, and body mass index (BMI) $> 35kg/m^2$ were excluded from each group. Ten prospective kidney donors were identified prior to elective kidney transplantation at the Royal Infirmary of Edinburgh between 01/10/2017 and 01/03/2020. Baseline scans were carried out at any point in the month preceding kidney donation. Follow-up scans were carried out in tandem with clinical appointments at any time up to 15 months post-donation. An overview of data demographic for the cross-sectional study is shown in Table 7.1 (further details are reported in appendix F).

	Controls	**CKD**	**Donor**	***p*-value***
Age(mean $\pm$ SD)	48$\pm$9	49$\pm$13	52$\pm$12	0.72
Gender (M/F)	16/11	14/16	17/13	0.80
eGFR (mean $\pm$ SD)	96$\pm$11	35$\pm$29	63$\pm$16**	0.72
Smoking (Y/N)	9/21	8/12	1/29	0.82
Hypertension	0	19	-	

*: *t*-test was performed between Controls and CKD
**: post-donation values

Table 7.1: Demographics (cross-sectional study.

7.3.1 Cross-sectional study

OCT-A images of one eye (either left or right, randomly chosen) with 3$\times$3 mm^2 field of view were analysed to extract retinal metrics as previously described in sections 5.3.2 and 6.2.2. OCT-A scans with observable artifacts (for example, vertical, horizontal, quilt defects) were discarded. A multivariate analysis was performed using only patients with CKD and healthy controls to unravel associations between retinal phenotypes and renal disease. A linear regression model corrected by gender and age was built for each retinal feature. Statistically significant phenotypes were further analysed to retrieve only uncorrelated retinal variables by selecting a threshold on the distance between features based on Pearson correlation coefficient. The final set of uncorrelated significant features was used for exploratory data analysis by using principal component analysis (PCA). By projecting healthy controls and patients with CKD in a two-dimensional space, separability between classes was assessed by clustering participants into two groups using

k-means algorithm. Using the same set of retinal features, kidney donors were projected onto the CKD-Control plane. K-means clustering was applied to assess the disposition of donors in the space. Associations of the first PCA component in the donors group (the one with the highest variability) with possible covariates (*i.e.,* time since donation and eGFR) were explored.

7.3.2 Longitudinal study

The right eye of 10 donors was analysed with the OCT-A computational framework to extract retinal phenotypes similar to the cross-sectional analysis. Changes over time of the two most common CKD-related vessel morphometrics reported in previous investigations [67], [68], *i.e.,* vessel density and foveal avascular zone (FAZ) area, and the significant features obtained in the case-control study, were analysed. Differences in retinal phenotypes were calculated and compared to baseline measurements as previously shown in section 4.7.2. Standard errors were computed assuming pre-donation scans as baseline. If changes in any phenotype were distributed around zero (one-sample t test or Mann-Whitney-Wilcoxon test depending on data normality), it was assumed that the differences seen were due to imaging artifacts. Otherwise, it was concluded that structural/functional changes (*i.e.,* reduced/impaired blood flow in the vasculature) had occurred between visits. Table 7.2 reports clinical information of participants of the longitudinal study.

	eGFR	Number of participants	p-value*
Pre-donation	96 ± 13	10	-
1st follow-up**	65 ± 7	10	<0.001
2nd follow-up ***	68 ± 13	6	<0.01

*: paired *t-test* using pre-donation as baseline
**: up to 3 months post-donation
***: up to 15 months post-donation

Table 7.2: eGFR values pre-post donation.

7.4 Results

7.4.1 Living kidney donors phenotypically align with CKD

Multivariate analysis reports twenty retinal features statistically significant in the CKD and Control groups comparison. Figure 7.1 shows the heatmap of the significant features according to their correlation values. By setting the threshold to the maximum distance between features to 0.95, only 5 uncorrelated retinal phenotypes are selected (according to the minimum p-value in the multivariate analysis). PCA on the remaining uncorrelated features (Figure 7.2A) shows separability between groups quantified using k-means in 77% of accuracy (Figure 7.2B). The projection of donors in the same two-dimensional space places participants across the plane with the majority of donors falling in the CKD group when clustering is applied (Figure 7.3A & B). Finally, the spatial distribution of donors in the plane does not show any association with the covariates age, time since donation, and eGFR (Table 7.3), confirming that the proximity of living kidney donors in the 2-dimensional space to either healthy controls or patients with CKD was not influenced by recognised risk factors for CKD or CVD. Further investigations on the stability of these clusters using three principal components and linear discriminant analysis can be found in appendix F.

	R	p-value
Age	-0.05	0.65
Time since donation	-0.17	0.12
eGFR	0.07	0.53

Table 7.3: Associations between the first principal component, PC1, and covariates.

7.4.2 Retinal vascular phenotypes associated with CKD evolve over time in living kidney donors

Follow-up measurements of all significant retinal features in the cross-sectional study, in addition to vessel density and FAZ area, are analysed and compared to baseline measurements. Repeated scans of kidney donors show significant temporal changes ($p<0.05$) in six retinal phenotypes previously reported to be stable in healthy controls

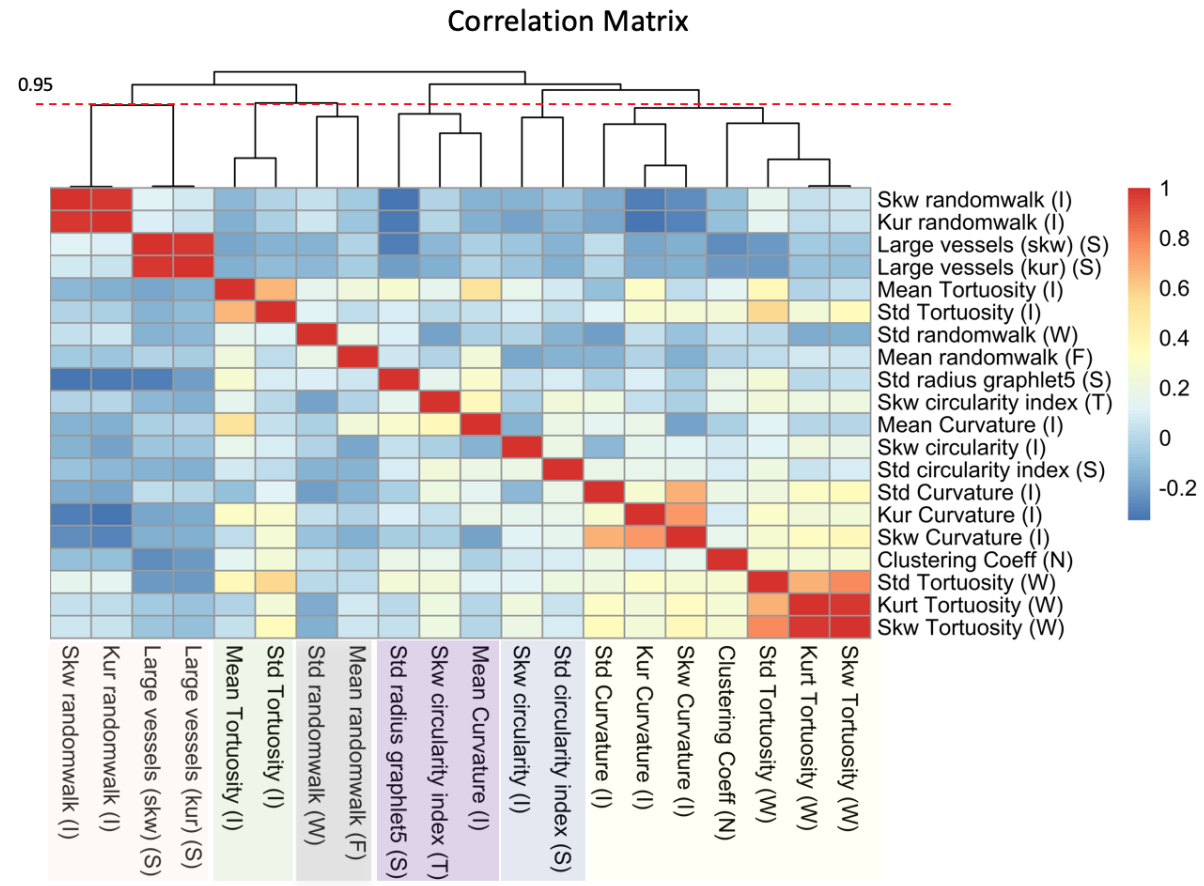

Figure 7.1: Heatmap of correlations between retinal phenotypes.

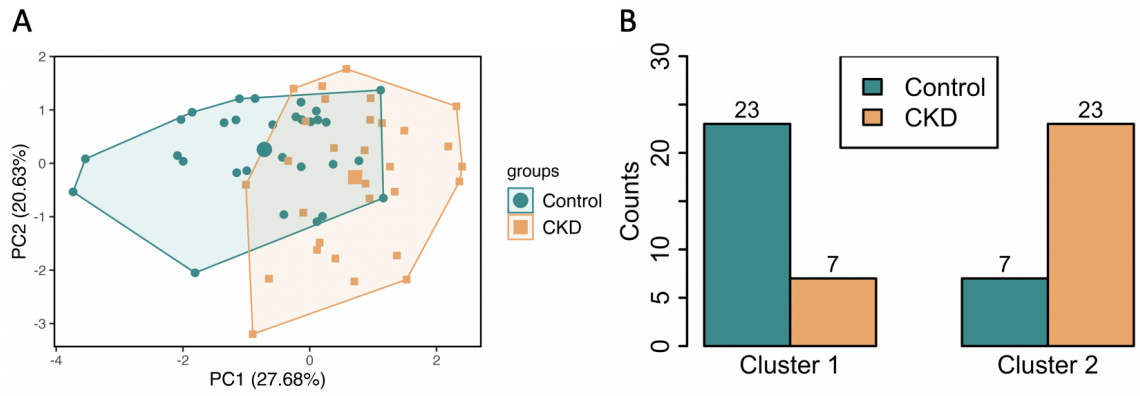

Figure 7.2: (A) PCA of CKD and control groups (B) Histogram of number of CKD and control participants in each cluster.

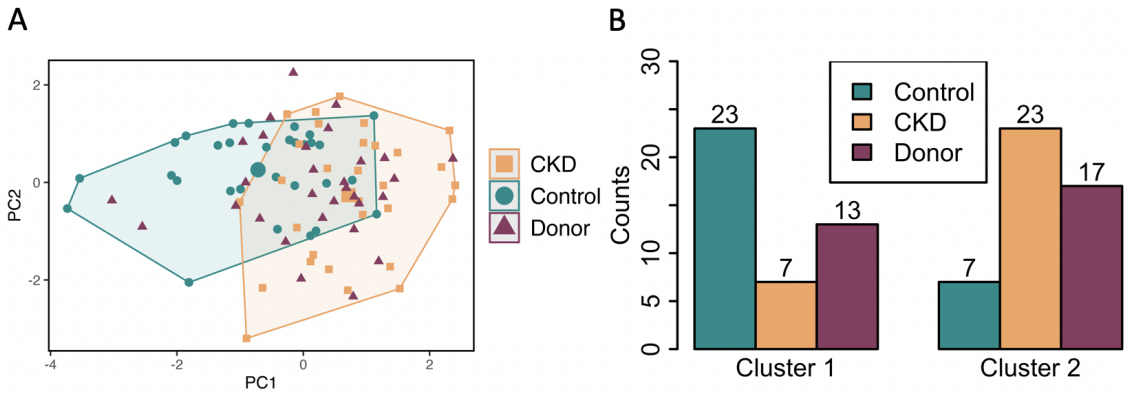

Figure 7.3: (A) PCA of control, CKD, and donor groups. (B) Histogram of number of CKD, control, and donor participants in each cluster.

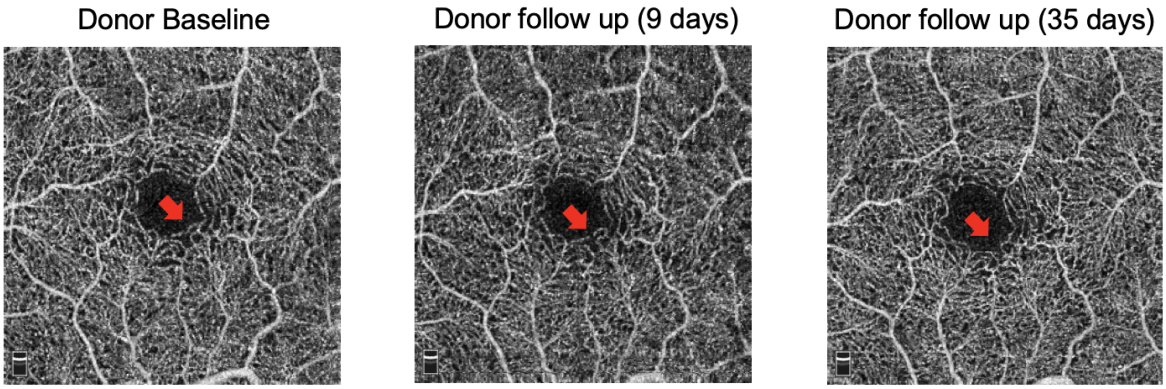

Figure 7.4: Changes in FAZ area across OCT-A repetitions in a living kidney donor.

(section 4.7.2). Among those, an increase in FAZ area and a decreased asymmetry in the distribution of shapes of the inter-capillary spaces (skewness of circularity index measure) are reported (see figure 7.5). An example of changes in vessels around FAZ across repeated acquisitions is shown in figure 7.4. Finally, as donors lose a percentage of their overall eGFR following kidney donation, associations between these retinal changes and eGFR values are explored (Figure 7.5 & 7.6). Interestingly, from the six phenotypes discovered, only the increase in FAZ area showed a moderate-to-high degree of correlation (R=0.54, p=0.03) whereas the remaining five could not be explained by changes in eGFR post-donation (p>0.05). These data suggest that retinal OCT-A might provide additional information to that obtained from standard clinical measures.

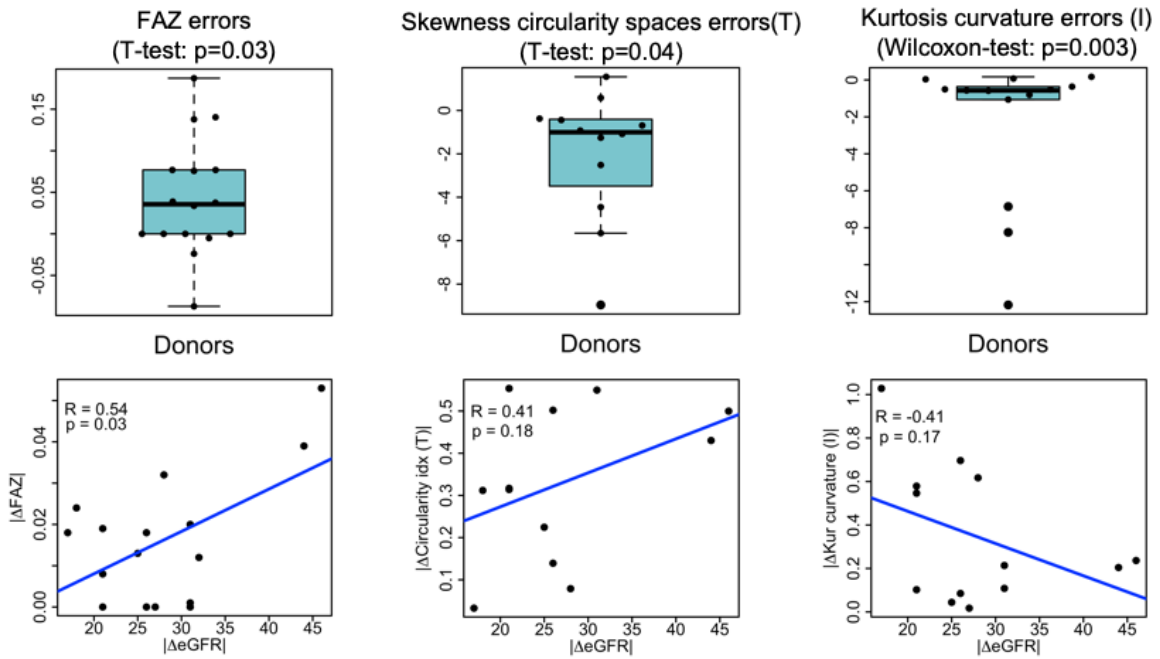

Figure 7.5: Boxplots of normalised difference in measurements between follow up visit and baseline in donors, and Pearson correlations between difference in retinal phenotypes and eGFR values.

7.5 Discussion

Previous studies have suggested that living kidney donors have normal kidney function since retaining near-healthy eGFR, the common clinical biomarker of kidney function [158], [159]. However, more recent investigations have shown that changes in clinical biomarkers are detectable only after a long period since the nephrectomy [160], [161] and living kidney donors are at higher risk of ESKD and CVD. This work hypothesises that subtle changes at the microvasculature level may happen in living kidney donors before changes in common clinical biomarkers and retinal imaging can help in identifying those donors most at risk. The OCT-A computational framework is used to analyse microvascular changes between groups of participants (Controls, CKD, and Donors). Using retinal features, it may be possible to discriminate between participants with CKD and healthy controls. Interestingly, most of the living kidney donors are not phenotypically aligned to the healthy group, indicating that further investigations using retinal imaging may elucidate how to discriminate participants with normal kidney

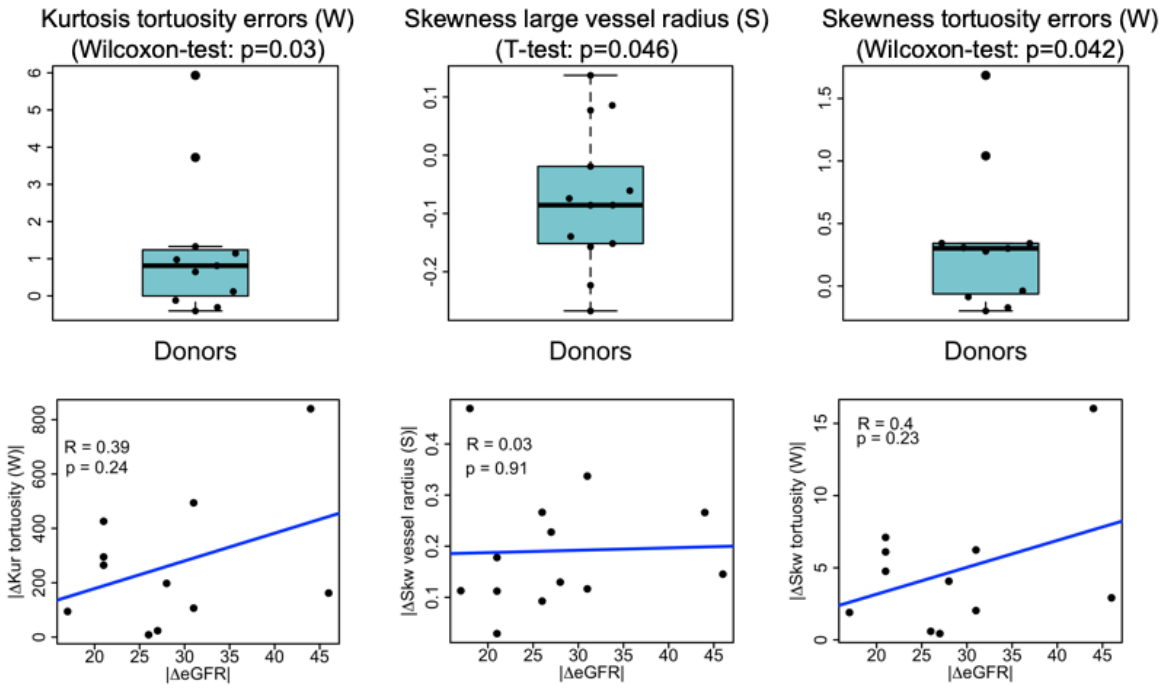

Figure 7.6: Boxplots of normalised difference in measurements between follow up visit and baseline in donors, and Pearson correlations between difference in retinal phenotypes and eGFR values.

function from those developing early-stage CKD. Based on these findings, for the first time, a longitudinal analysis of how OCT-A phenotypes evolve over time following kidney donation is proposed. Longitudinal results suggest that changes in FAZ, inter-capillary space shape, vessel size, tortuosity, and vessel curvature, are retinal microvascular characteristics that may help track the renal and cardiovascular consequences of kidney donation beyond existing clinical markers. Among those features, changes in retinal vessel caliber and FAZ area have been reported previously in studies including patients with CKD [42], whereas vessel tortuosity has been associated with diabetes [162] and hypertension [163] common risk factors for both CKD and CVD.

The pathogenesis of kidney impairment is still under investigation. Evidence suggests that microvascular alterations are a possible cause of renal dysfunction [66]. Compromised blood flow can arise from systemic inflammation, unbalance in angiogenic growth factors, and dysfunction of the glomerular endothelial cells. This can promote vessel rarefaction which increases haemodynamic dysfunction and renal ischaemia leading to kidney scarring and progressing to ESKD. Since eye and kidney diseases can be closely connected, retinal microvascular changes have been previously associated with renal dysfunction independently of age, gender, race, hypertension, and diabetes [153] Consequentially, retinal vascular alterations might reflect underlying mechanisms of inflammation, endothelial dysfunction, leading to ischemia and disruption of renal blood flow. It is hypothesised these mechanisms can also be, in the long-term, triggered in kidney donors due to the process of stabilisation of renal function in absence of one kidney. It should be highlighted the preliminary but potentially important nature of this work which limitations include the small sample size in both cross-sectional and longitudinal studies. Therefore, future work will involve the validation of these results on a larger cohort and the investigation of the more interesting aspect of longitudinal changes in individual patients.

To conclude, this chapter proposed the application of the OCT-A computation framework to the cross-sectional and longitudinal studies to identify changes in retinal changes in retinal microvascular phenotypes in living kidney donors. It is presented, for the first time, a study on the alterations in the retinal microvasculature over time after kidney donation. Although preliminary, this research represents a step forward towards the characterisation

of cardiovascular consequences in healthy individuals after donating a kidney that may contribute to redefining the risk assessment of kidney donation.

Chapter 8

Discussion

8.1 State-of-the-art and thesis objectives summary

Retinal image analysis has demonstrated great potential for revealing biomarkers of eye-related disease and systemic disease that undirectly affects the eye. This has led to an increasing interest in mining the retinal landscape for biomarker discovery of both ocular and systemic diseases. In this scenario, the recently developed OCT-A technology has enabled the visualisation of the smallest capillaries in the retina in a fast and efficient way without the need of a contrast agent, becoming a key modality for the study of the retinal microvascular system. Nonetheless, the potential of OCT-A in clinical diagnostic is still under investigation. The assessment of pathological conditions and the reproducibility of studies rely on the quality of the image processing. However, automated OCT-A image segmentation is an open problem in the field and benchmark data for method development are still limited. Hence, the first aim of this thesis was the assessment of a standardised image processing pipeline for OCT-A images by surveying several segmentation methodologies and by proposing different evaluation metrics able to capture similarities in pixelwise and structural characteristics between segmented OCT-A scans and manually labelled ground truth images (chapter 3).

Another limitation of the current clinical studies is the small number of OCT-A retinal phenotypes. Despite promising results have been reported in conditions such as diabetic retinopathy, chronic kidney disease, and Alzheimer's disease, the limited set of investigated vascular measurements is not sufficient to cover the full spectrum of retinal phenotypes to uniquely characterise diseases. Therefore, the second and the third aims of

this thesis were the development of a framework for the extraction of retinal microvascular metrics and the implementation of novel structural and functional phenotypes for the hypothesis-free discovery of new retinal biomarkers of disease (chapter 4).
Finally, OCT-A microvascular phenotypes have been primarily used to investigate associations with ocular and systemic diseases using statistical analysis (see chapter 2), however, OCT-A measurements can also help to identify patients suffering from diseases with a retinal vascular footprint and to detect early changes in the microvasculature for long-term risk assessment of conditions that might affect the vascular system. Therefore, the fourth and final aim of this thesis was the classification of patients' status using machine learning models built using the implemented retinal microvascular phenotypes extracted from modestly-sized image datasets (chapter 5, 6, 7).

8.2 Key findings

This thesis presented the first open dataset of retinal parafoveal OCT-A images with associated ground truth manual segmentations. Particular attention was paid to segmenting the images in a reproducible way demonstrating good inter- and intra-rater agreement. A comparison of state-of-the-art vessel enhancement and binarisation procedures under a unified computational framework was presented and the source code was made available. By introducing two novel topological metrics (LLC and TopS), segmentation quality measures were evaluated to guide the identification of the algorithm that not only provided the best agreement with the manually segmented images but also achieved the best preservation of the vascular network structure. Deep learning methods, U-Net and CS-Net, reached optimal performances in almost all the considered evaluation metrics, suggesting these methods as the best segmentation approach for parafoveal OCT-A image segmentation. Interestingly, OOF achieved segmentation performances in line with the neural network architectures without the requirement of extensive manually segmented images for training purposes. Moreover, this investigation highlighted how clinically relevant metrics used to analyse OCT-A images are sensitive to the segmentation method, suggesting that precaution should be taken when comparing the results of clinical studies and performing meta-analyses. This part of the thesis has been published in

Translational Vision Science & Technology [5].

A network-based framework, containing the implementation of well-known and novel retinal microvascular phenotypes divided into four groups of retinal features, graph-based, coordinate-based, topology-based, and flow-based metrics, was proposed for the analysis of OCT-A images and to cover the full spectrum of candidate retinal vascular biomarkers. This framework enables the hypothesis-free discovery of new retinal biomarkers of disease and the implementation of machine learning models using clinically interpretable retinal features. The OCT-A computational framework was applied in three different case studies with a retinal vascular footprint: diabetic retinopathy (DR), chronic kidney disease (CKD), and living kidney donation. In the DR study, consistently with previous investigations, results showed a reduction in vessel skeleton density and an enlargement of the intercapillary spaces in the superficial layer of the retina. In the CKD study, changes to vessel radius and curvature of the foveal avascular zone were reported in patients with CKD when compared to the healthy controls. The classification of participants, based on the retinal measurements extracted using the OCT-A framework, demonstrated that patients with DR were easier to identify than participants with diabetes without DR, whereas changes in patients with CKD were more subtle and challenging to detect. Overall, automated image classification approaches using the extracted retinal phenotypes achieved comparable results to the deep learning approach (VGG16) with the added advantage of feature interpretability. A description of the OCT-A computational framework and the application to diabetes and CKD studies has been published by Springer International Publishing as proceeding of the 7th MICCAI Workshop on Ophthalmic Medical Image Analysis (OMIA7) [6] The final application of the OCT-A computational framework proposed, for the first time, the use of non-invasive imaging of the retinal microvasculature as a tool to improve targeting living kidney donors at risk of CKD and cardiovascular disease. Results suggested that OCT-A microvascular phenotypes may help to gain insights into the timing of vascular changes in kidney donors enhancing the understanding and assessment of the risks of kidney donation.

In summary, the OCT-A computational framework developed in this thesis lays the foundation of a novel approach for retinal microvascular analysis that can contribute to realising the full diagnostic potential of OCT-A imaging and accelerating the

implementation of patient-specific approaches to achieving precision medicine.

8.3 Limitations and future work

Advances in the OCT-A computational framework

Despite the promising results, it is worth mentioning the limitations of this research. The OCT-A computational framework had been developed exclusively using images acquired by the Optovue RTVue XR Avanti retinal device and the implementation is customised on images centered at the macula with $3 \times 3\ mm^2$ field of view. Therefore, a generalisation of the OCT-A computational framework should be developed for the analysis of images captured using different OCT-A systems. Future work should also investigate more advanced segmentation procedures able to perform vessel segmentation in the deep layers of the retina, in the optic nerve, and in OCT-A scans with a larger field of view. Further studies on the assessment of the robustness of segmentation methods across OCT-A technologies from multiple manufacturers are also recommended. The characterisation of the microvasculature should be further explored by segmenting arteries and veins in OCT-A scans and by optimising current network-based metrics (such as tortuosity) based on vessel classification. Novel functional metrics should be implemented to further capture the haemodynamic information enclosed in OCT-A images. It will be also important to explore the use of phenotypes extracted from the other retinal layers (deep and choroid) to elucidate how diseases affect different parts of the eye.
Finally, further research should explore more advanced feature selection approaches, such as wrapper methods or genetic algorithms [148], to leverage the large number of biomarkers discovered without suffering from the peaking phenomenon.

Large OCT-A cohorts and longitudinal studies

This thesis has demonstrated the potential of OCT-A technology in ocular and systemic diseases in relatively small cohorts. Future analysis should validate these results on larger datasets of OCT-A scans possibly also from devices made by different manufacturers.
Furthermore, previous investigations on retinal vasculature have been carried out by using only one imaging modality (e.g., fundus camera or OCT). However, current ongoing

studies (e.g., PREVENT [94] and NHS Lothian cohort 3) involve the collection of images captured using multiple retinal devices. Different retinal imaging modalities provide different types of information that may be relevant to disease diagnosis. For example, OCT imaging allows the quantification of retinal thickness, important for detecting retinal ganglion cell damage. Ultra wild field retinal imaging captures vessels at the periphery of the retina, where early onset of diseases might manifest. Therefore, future work should also explore the possibility of combining different imaging modalities to acquire a more comprehensive view of the retinal vascular landscape. Combination of features extracted from multiple modalities may lead to a better understanding of the relationship between changes at the microscale and effects at the macroscale, allowing also future retrospective studies with large cohorts and retinal images such as UKBiobank [11] and SCONe (the Scottish Collaborative Optometry-Ophthalmology Network e-research) [12].

Finally, a promising future work should be the application of OCT-A technology to monitor changes over time in longitudinal scans. The study of longitudinal data may help to identify patients at risk and detect early onset of disease. Longitudinal studies should explore also associations between changes over time in retinal microvascular phenotypes and known clinical biomarkers of disease (such as beta-amyloid in Alzheimer's disease) to elucidate underlying biological mechanisms and the aetiology of retinal changes, unravelling the connection between the eye and other organs.

Appendix A

Evaluation metrics and statistics

Confusion matrix

Considering a boolean classification problem, the confusion matrix is a table with information about the performance of the classifier. Rows contain instances of the actual class, whereas columns contain instances of the predicted class.

		Predicted	
		Predicted (1)	**Predicted (0)**
Actual	**Actual (1)**	True Positive (TP)	False Negative (FN)
	Actual (0)	False Positive (FP)	True Negative (TN)

Precision

Given the confusion matrix, precision is defined as

$$Precision = \frac{TP}{TP + FP}, \tag{A.1}$$

indicating the ratio of the positively identified actual instances over all positive predicted instances.

Recall

Recall, also known as sensitivity or true positive rate (TPR), represents the ratio between the instances positively identified and the total number of positive actual instances,

$$Recall = \frac{TP}{TP + FN}. \tag{A.2}$$

Specificity

Specificity, also called true negative rate (TNR), is the ratio between the instances correctly predicted as negative and the total number of negative actual instances,

$$Recall = \frac{TN}{TN + FP}. \tag{A.3}$$

False positive rate

The false positive rate (FPR) describes the ratio between the incorrectly predicted negative instances and the total number of actual negative instances.

$$FPR = \frac{FP}{TN + FP}. \tag{A.4}$$

Accuracy

The accuracy of a classifier is defined as the ratio of correctly predicted instances over the the total number of instances, that is

$$Accuracy = \frac{TP + TN}{TP + FP + TN + FN}. \tag{A.5}$$

Receiver operator curve (ROC)

For each instance in a test set, the output of machine learning classifiers is a probability for that instance to belong to each class. A threshold of this predicted probability (typically 0.5)

is chosen to get a binary classification. The receiver operator curve is a graph showing the variation of FPR and TPR at different classification thresholds.

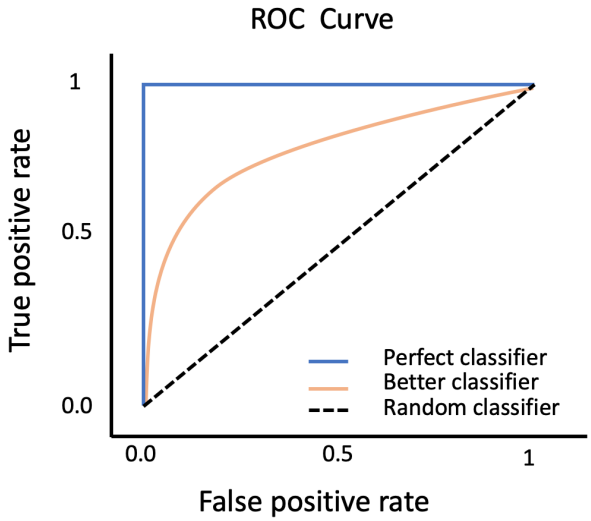

Figure A.1: Examples of ROC curves.

Area under the ROC Curve (AUC)

This AUC is a measure threshold invariant. It provides a score for the performance of the classification model by measuring the area under the ROC curve. It ranges from 0 to 1, and its maximum is reached only if the model correctly classify all the samples [164].

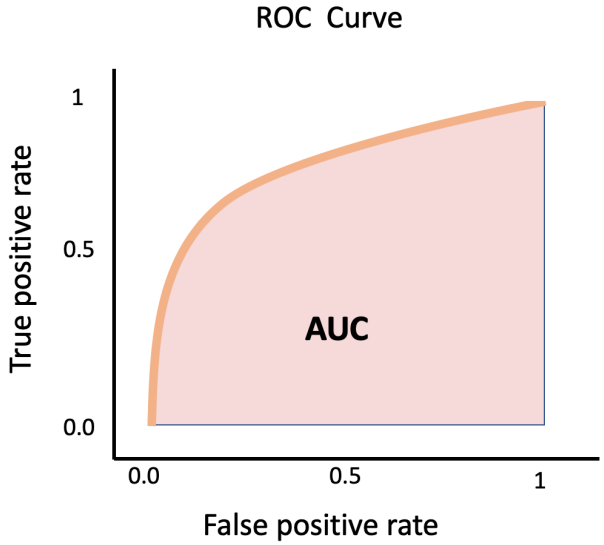

Figure A.2: Area under the ROC curve.

Mutual Information

Mutual information (MI) describes the mutual dependency between two random variables. Considering, X and Y two random variables, MI is defined as

$$I(X;Y) = \sum_{y \in Y} \sum_{x \in X} p_{(X,Y)}(x,y) \cdot log \left(\frac{p_{(X,Y)}(x,y)}{p_X(x) p_Y(y)} \right), \tag{A.6}$$

where $p_{(X,Y)}$ is the joint probability, log is the natural logarithm, and p_X and p_Y are the marginal probability density functions. MI satisfies the following properties:

- Non-negative: $I(X;Y) \geq 0$
- Symmetric: $I(X;Y) = I(Y;X)$
- $I(X;Y) = 0 \Leftrightarrow X$ and Y are independent.

MI is closely related to the concept of uncertainty described by the entropy measure. Indeed, considering the entropy of a random variable, X, $H(X)$, the MI described in equation A.6 can be computed as

$$\begin{aligned} I(X;Y) &= H(X) - H(X \backslash Y) \\ &= H(Y) - H(Y \backslash X) \\ &= H(X) + H(Y) - H(X,Y) \\ &= H(X,Y) - H(X \backslash Y) - H(Y \backslash X) \end{aligned} \tag{A.7}$$

Qualitatively, a high MI value corresponds to a reduction of uncertainty, while a very low MI value corresponds to an insignificant reduction.

In this work, MI is used as feature selection method as implemented in the *scikit-learn* python library [165]. The code is based on the implementation described by Ross (2014) [166].

Pearson correlation coefficient

The sample Pearson correlation coefficient, indicates the linear correlation between samples from two random variables. Given a set of n pairs of data $(x_1, y_1), ..., (x_n, y_n)$, the Pearson correlation coefficient, r_{xy} is defined as

$$r_{xy} = \frac{\sum i = 1^n (x_i - \bar{x})(y_i - \bar{y})}{\sqrt{\sum i = 1^n (x_i - \bar{x})^2} \sqrt{\sum i = 1^n (y_i - \bar{y})^2}}, \tag{A.8}$$

where $\bar{x}$ and $\bar{y}$ represent the sample mean.

Appendix B

Persistent homology and Betti numbers

The study of topological features and shapes of data, which takes the name of topological data analysis (TDA), is acquiring more and more interest in the medical imaging domain. Persistent homology (PH) is an algebraic tool that allows the extraction of topological features from a N-dimensional space and often applied in TDA. In computer vision, PH is based on the concept of cubical complex which represents the fundamental unit of the topological space. In this section, notations and definitions follow the ones used in [167]. Considering S, a 2-D image of size $N \times N$, with element $s_{ij} \in [0,1]$, where i indicates the i-th row and j the j-th column, a pixel in the image covers a unit square which represents an elementary square $Q_{ij} = [i, i+1] \times [j, j+1]$ of the space. Considering a threshold p of the pixel intensity value (also called filtration), we can obtain the cubical complex $B(p)$ as follows

$$B(p) = \bigcup_{i,j=0}^{N} Q_{i,j} : s_{i,j} \geq p. \tag{B.1}$$

Hence, *B(p)* represents a binarised image, with all pixels above p are set to 1 and 0 otherwise. By varying increasingly the value of the filtration, we obtain encapsulated cubical complexes.

$$\emptyset \subseteq B(1) \subseteq B(p_1) \subseteq B(p_2) \subseteq \ldots \subseteq B(0).$$

For each value of the filtration, it is possible to count the number of topological features by using the *Betti numbers*, β_k, where k corresponds to the topological feature of dimension

k. For example, given a filtration value p, β_0 counts the number of connected components in the cubical complex $B(p)$, β_1 represents the number of holes, and β_2 is the number of voids. In this work, we have used 2D images and the Betti number β_1 to propose a novel topological metric to evaluate the goodness of the segmentation approach in retrieving the same number of topological structures (chapter 3.6) [109].

Appendix C

Unstable retinal phenotypes

Unstable phenotypes obtained from the analysis described in chapter 4.

Retinal Phenotypes	p-values
Average path length (W)	0.036238496
Average clustering coeff (F)	0.047577583
kurt path length (F)	0.042161745
Graph density (I)	0.011728289
Number of nodes (I)	0.020852481
Number of edges (I)	0.030138957
Number of non-edges (I)	0.024002464
Non-edge percentage (I)	0.017140851
Edges percentage (I)	0.011728801
Skw edge radius (I)	0.032414447
Graph radius (S)	0.017238312
Graph diameter (S)	0.039526991
Std circularity (S)	0.010547654
Std difference circle areas (W)	0.032721409
Mean face area (F)	0.025409989
Mean face circularity (F)	0.003725012
Median circularity (F)	0.004223907
Kurtosis difference circle area (F)	0.014206482
Std circularity (I)	0.037948008
Kurtosis difference (I)	0.002961722
Kurtosis circularity (T)	0.032882412
kurtosis difference (T)	0.01696312
Mean difference circle area (S)	0.001427173
Median difference (S)	0.002783055

Retinal Phenotypes	p-values
Skw resistance (N)	0.047577583
Kurt resistance (N)	0.018171391
Skw resistance (I)	0.003785717
Kurt resistance (S)	0.018171391
Skw resistance (S)	0.003785717
Mean tortuosity (I)	0.014590497
Std tortuosity (I)	0.002961722
Kurt tortuosity (I)	0.009578147
Skw tortuosity (I)	0.010308689
Median curvature (I)	0.01206692
Mean tortuosity (S)	0.005631652
Std tortuosity (S)	0.035020861
Graphlet1 mean length (F)	0.007991359
Graphlet2 mean length (F)	0.02990997
Graphlet4 mean radius (F)	0.037493287
Graphlet5 mean radius (F)	0.04334887
Graphlet7 std.radius	0.003644568
Graphlet1 counts (N)	0.0226888
Graphlet2 counts (N)	0.04303485
Graphlet4 counts (N)	0.005136789
Graphlet5 counts (N)	0.007064647
Graphlet5 mean length (N)	0.033669432
Graphlet7 mean length (N)	0.033511074
Graphlet1 mean radius (I)	0.042158569
Graphlet2 mean radius (I)	0.016650156
Graphlet4 mean radius (I)	0.020030823
Graphlet5 std radius (S)	0.048563584
Graphlet 6 mean length (S)	0.036077784
Mean distance (L)	0.001985734
Std distance (W)	0.004534494
Skewness distance (W)	0.012806617
Kurtosis distance (W)	0.008894125
HS skw branching ratio (W)	0.002961722

Appendix D

Significant retinal phenotypes in DR

Following the analyses in chapter 5, statistically significant p-values obtained by using either a **t**-test or a Mann–Whitney–Wilcoxon test between healthy subjects, participants with DR, and diabetic patients without retinopathy (NoDR) are reported.

Phenotypes (DRvsControl)	P-values
Number of faces (W)	0.003021293
Mean face area (W)	0.001041667
Mean face circularity (W)	0.012838435
Median face circularity (W)	0.006683517
Number of faces (N)	0.005915138
Mean face area (N)	0.012826694
Std face area (N)	0.010862255
Mean face circularity (N)	0.002599365
Median face circularity (N)	0.000190626
Number of faces (I)	0.005033748
Number of faces (T)	0.003203301
Number of faces (S)	0.000110754
Mean face area (S)	0.009169926
Std face area (S)	0.002111491
Number of nodes	0.001780592
Number of edges	0.001808625
Graph density	0.000283039
Number of endpoints	0.002065509
Number of simplified edges	0.002102373
Skew path length (F)	0.009233062

Phenotypes (DRvs Control)	P-values
Skw edge radius (F)	0.001224423
Kur edge radius (F)	0.004115815
Graph density (N)	0.007044781
Number of nodes (N)	0.002888228
Number of edges (I)	0.00330961
Number of non-edges (I)	0.002275688
Percentage non-edegs (I)	0.007312621
Percentage edges (I)	0.007312621
Number of faces (I)	0.005113677
Median perimeter faces (I)	0.001256658
Graph density (T)	0.001200217
Number of nodes (T)	0.000653634
Number of edges (T)	0.000727812
Number of non-edges (T)	0.00047995
Percentage of non-edges (T)	0.001200225
Perfentage of edges (T)	0.001200224
Number of faces (T)	0.003105203
Median perimeter faces (T)	0.000681281
Kur perimeter faces (T)	0.013922058
Average degree (T)	0.014262377
Mean path tortuosity (T)	0.004513203
Std path tortuosity (T)	0.001155076
Median edge radius (T)	2.48E-05
Std edge radius (T)	0.004126523
Graph density (S)	0.000111288
Number of nodes (S)	0.000567337
Number of edges (S)	0.000611686
Number of non-edges (S)	0.000625554
Percentage non-edegs (S)	0.000111288
Percentage edges (S)	0.000111288
Number of faces (S)	0.000110665
Median perimeter faces (S)	0.010175007

Phenotypes (DRvs Control)	P-values
Mean perimeter faces (S)	0.000316909
Std perimeter faces (S)	0.000442677
Average path length (S)	0.002111491
Median path length (S)	0.006310309
Std path length (S)	0.011808292
Average degree (S)	0.003530944
Kur node degree (S)	0.004513203
Std path tortuosity (S)	0.01633041
Std edge radius (S)	0.002565295
Skw edge radius (S)	0.010862255
Kur edge radius (S)	0.006473883
Graphlet 1 mean radius (S)	0.000808465
Graphlet 1 std radius (S)	0.004693123
Graphlet 2 mean radius (F)	0.000144727
Graphlet 2 std radius (F)	0.003498179
Graphlet 4 mean radius (F)	0.000141772
Graphlet 4 std radius (F)	0.004855823
Graphlet 5 mean radius (F)	0.000457548
Graphlet 5 std radius (F)	0.013964416
Graphlet 7 count (F)	0.014363991
Graphlet 1 count (N)	0.005723945
Graphlet 1 std radius (N)	0.013753389
Graphlet 2counts (N)	0.007926892
Graphlet 2 mean radius (N)	0.008526856
Graphlet 2 std radius (N)	0.001500087
Graphlet 4 count (N)	0.007650675
Graphlet 4 mean radius (N)	0.002498935
Graphlet 4 std radius (N)	0.00562045
Graphlet 5 count (N)	0.008007482
Graphlet 5 mean radius (N)	0.002996341
Graphlet 5 std radius (N)	0.001971832
Graphlet 7 count (N)	0.000745857

Phenotypes (DRvs Control)	P-values
Graphlet 1 count (I)	0.015231025
Graphlet 2 count (I)	0.007384505
Graphlet 4 count (I)	0.005584652
Graphlet 5 count (I)	0.00521251
Graphlet 1 count (T)	0.00875745
Graphlet 1 mean length (T)	0.015639602
Graphlet 2 count (T)	0.002824178
Graphlet 4 count (T)	0.002178072
Graphlet 5 mean radius (T)	0.002269041
Graphlet 5 std radius (T)	0.013922058
Graphlet 1 count (S)	0.000200216
Graphlet 1 mean radius (S)	0.001349882
Graphlet 2 count (S)	0.001150874
Graphlet 2 std radius (S)	0.001049241
Graphlet 3 count (S)	0.002520383
Graphlet 4 count (S)	0.000111109
Graphlet 4 std radius (S)	0.002735967
Graphlet 5 count (S)	0.000132997
Graphlet 6 count (S)	0.002840374
Graphlet 7 count (S)	0.00122753
Mean resistance (F)	0.008408848
Median resistance (F)	0.001826292
Median resistance (N)	0.000828281
Std a2f (I)	0.007717001
Median resistance (I)	5.44E-05
Median a2f (T)	0.002824178
Skw resistance (T)	0.01598214
Std a2f (S)	0.007717001
Median resistance (S)	5.44E-05
Mean random walk length (W)	0.016051533
Std random walk length (W)	0.016363112
Mean node degree (W)	0.004107282

Phenotypes (DRvs Control)	P-values
Number of leaf nodes (F)	0.012266432
Mean node degree (N)	0.008437901
Mean node degree (I)	0.016000542
Mean node degree (T)	0.0104938
Mean random walk length (S)	0.002327095
Std random walk length (S)	0.010862255
Mean node degree (S)	0.003336895
Kur node degree (S)	0.012826694
Median tortuosity (W)	5.86E-07
Median tortuosity (I)	0.010248829
Median tortuosity (T)	0.0001467
Median tortuosity (S)	0.002299223
Number of leaf nodes Btree	0.01037707
Number of EE edges	0.004718336
Number of EI edges	0.007994055
Number of edges (N)	0.002885439
Number of non edges (N)	0.002260788
Percentage non-edges (N)	0.007044764
Percentage edges (N)	0.007044764
Number of faces (N)	0.005974584
Mean number of nodesper subarea (N)	0.011737043
Std number of nodes per subarea (N)	0.014471133
Mean edegs radisu (N)	0.000760306
Std edge radius (N)	0.008415459
Graph density (I)	0.00731262
Number of nodes (I)	0.0032873
Skew distance random nodes (F)	0.001279805
Mean edge radius (F)	8.23E-05
Median edge radius (F)	1.16E-08
Std edge radius (F)	0.000399082

Phenotypes (NoDRvsControl)	P-values
Median face area (F)	0.004574728
Kur face circularity (F)	0.00764042
Mean circularity ratio (F)	0.004700911
Median circularity ratio (F)	0.000605085
Median face circularity (N)	0.010403272
Std face area (I)	0.006153937
Median face area (S)	0.015577083
Std number of nodes (F)	0.009150614
Kur tuning points (F)	0.015538692
Median edge radius (S)	3.83E-06
Mean face perimeter (S)	0.011563585
Graphlet 5 count (F)	0.0124718
Graphlet 6 lstd length (I)	0.014101205
Median a2f (N)	0.012291894
Std a2f (I)	0.011563585
Kurt a2f (I)	0.002741139
Skw a2f (I)	0.002425216
Std a2f (S)	0.011563585
Kurt a2f (S)	0.002741139
Skw a2f (S)	0.002425216
Mean node degree (F)	0.011456258
Median tortuosity (W)	0.00405128
Std tortuosity (W)	0.010448889

Phenotypes (DRvsNoDR)	P-values
Number of faces (W)	0.007276045
Number of faces (T)	0.004529486
Number of faces (S)	0.001422597
Mean face area (S)	0.008711913
Std area (S)	0.006410198
Skw face circularity (S)	0.005253118
Std circularity ratio (S)	0.015631006
Number of nodes (W)	0.002898015
Number of edges (W)	0.003086879
Graph density	0.005081352
Number of ednpoints (W)	0.002729469
Number of simplified edges (W)	0.002932965
Graph density (F)	0.0111994
Percentage of non-edge (F)	0.0111994
Percentage of edges (F)	0.0111994
Std number of nodes per subarea (F)	0.012892595
Skw distance random node (F)	0.001703944
Std number of nodes (F)	0.002149666
Skw edge radius (F)	0.010807664
Graph density (N)	0.013831704
Number of nodes (N)	0.010102197
Number of edges (N)	0.010511831
Number of non edges (N)	0.011015579
Percentage of non-edge (N)	0.013831704
Percentage of edges (N)	0.013831704
Kur node degree (N)	0.01626643
Number of nodes (I)	0.015376859
Number of no-edges (I)	0.01531969
Graph density (T)	0.004588216
Number of nodes (T)	0.004439252
Number of edges (T)	0.004258447
Number of non-edges (T)	0.005070638

Phenotypes (DRvsNoDR)	P-values
Percentage non-edge (T)	0.004588216
Percentege edges (T)	0.004588216
Number of faces (T)	0.004126885
Median face perimeter (T)	0.004256533
Average path length (T)	0.002593444
Median path length (T)	0.002743346
Std path length (T)	0.006824675
Mean node degree (W)	0.014395937
Mean path length (F)	0.004601268
Std path length (F)	0.010119397
Std tortuosity path length (T)	0.001427975
Std number of turning points (T)	0.007368317
Graph density (S)	0.001670615
Number of nodes (S)	0.001262123
Number of edges (S)	0.001365775
Number of non-edges (S)	0.001877458
Percentage of non-edges (S)	0.001670615
Percentage edegs (S)	0.001670615
Number of faces (S)	0.001856255
Average node degree (S)	0.007383001
Skw number of nodes (S)	0.015631006
Kur number of nodes (S)	0.013554666
Std edge radius (S)	0.008711913
Graphlet 1 count (F)	0.00853888
Graphlet2 count (F)	0.008485724
Graphlet 4 count (F)	0.003970314
Graphlet 5 count (F)	0.006392112
Graphlet 7 count (F)	0.013434442
Graphlet 1 count (N)	0.01082123
Graphlet 3 count (N)	0.014747554
Graphlet 7 count (N)	0.005140128
Graphlet 1 count (T)	0.005948187

Phenotypes (DRvsNoDR)	P-values
Graphlet 2 count (T)	0.003248073
Graphlet 4 count (T)	0.00411817
Graphlet 5 count (T)	0.003814441
Graphlet 7 count (T)	0.016476205
Graphlet 1 count (S)	0.001472428
Graphlet 1 std radius (S)	0.000627012
Graphlet 2 count (S)	0.001213853
Graphlet 2 st radius (S)	0.005145413
Graphlet 3 count (S)	0.007234346
chraphlet 4 count (S)	0.00082636
Graphlet 4 std radius (S)	0.003897833
Graphlet 5 count (S)	0.002028231
Graphlet 5 std radius (S)	0.007863339
Graphlet 6 count (S)	0.004691766
Graphlet 7 count (S)	0.000637884
Mean node degree (W)	0.014395937
Mean random walk length (F)	0.004601268
Std random walk length (F)	0.010119397
Mean random walk length (N)	0.007593751
Mean node degree (N)	0.007360331
Mean randon walk length (S)	0.007155561
Mean node degree (S)	0.005811452
Kur curvature (N)	0.004451515

Appendix E

Significant retinal phenotypes in CKD

Following the analyses in chapter 6, statistically significant *p*-values obtained by using either a **t**-test or a Mann–Whitney–Wilcoxon test between healthy subjects and participants with CKD are reported.

Phenotype	p-value
Median resistance (I)	0.004435914
Median a2f (T)	0.037090076
Median resistance (S)	0.004435914
Std random walk length (W)	0.04087917
Kur random walk length (W)	0.042891146
Median tortuosity (W)	3.66E-07
Std tortuosity (W)	0.004833225
Kur tortuosity (W)	0.026057366
Skw tortuosity (W)	0.035308347
Mean tortuosity (N)	0.049674556
Std tortuosity (I)	0.013570987
Skw tortuosity (I)	0.033598809
Std curvature (I)	0.027271478
Kur curvature (I)	0.001393379
Skw curvature (I)	0.01265614
Median tortuosity (T)	0.00817405
Skw root to leaf node length	0.013965302
Kur root to leaf node length	0.023471039
Kur HS	0.031531931

Phenotype	p-value
Median resistance (I)	0.004435914
Median a2f (T)	0.037090076
Median resistance (S)	0.004435914
Std random walk length (W)	0.04087917
Kur random walk length (W)	0.042891146
Median tortuosity (W)	3.66E-07
Std tortuosity (W)	0.004833225
Kur tortuosity (W)	0.026057366
Skw tortuosity (W)	0.035308347
Mean tortuosity (N)	0.049674556
Std tortuosity (I)	0.013570987
Skw tortuosity (I)	0.033598809
Std curvature (I)	0.027271478
Kur curvature (I)	0.001393379
Skw curvature (I)	0.01265614
Median tortuosity (T)	0.00817405
Skw root to leaf node length	0.013965302
Kur root to leaf node length	0.023471039
Kur HS	0.031531931

Appendix F

Kidney donation study (SI)

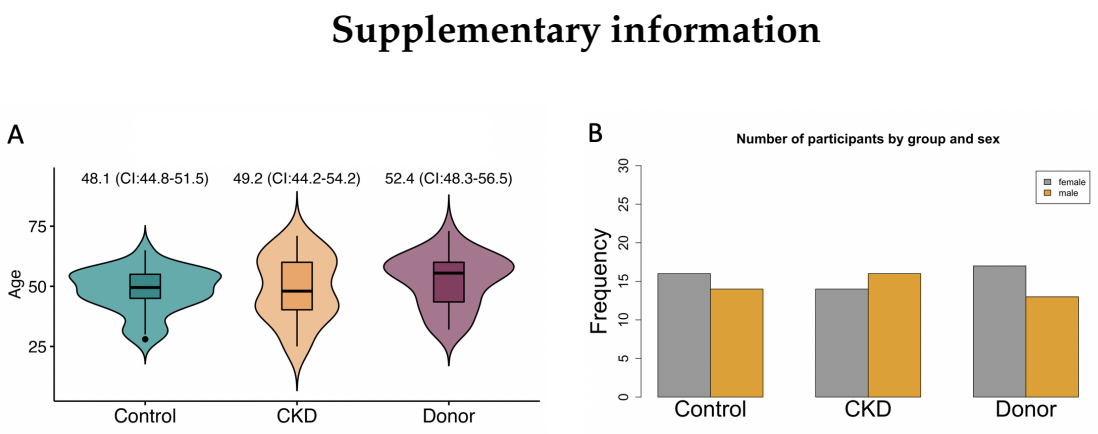

Figure F.1: Demographic data kidney donation study, age (A), and gender (B).

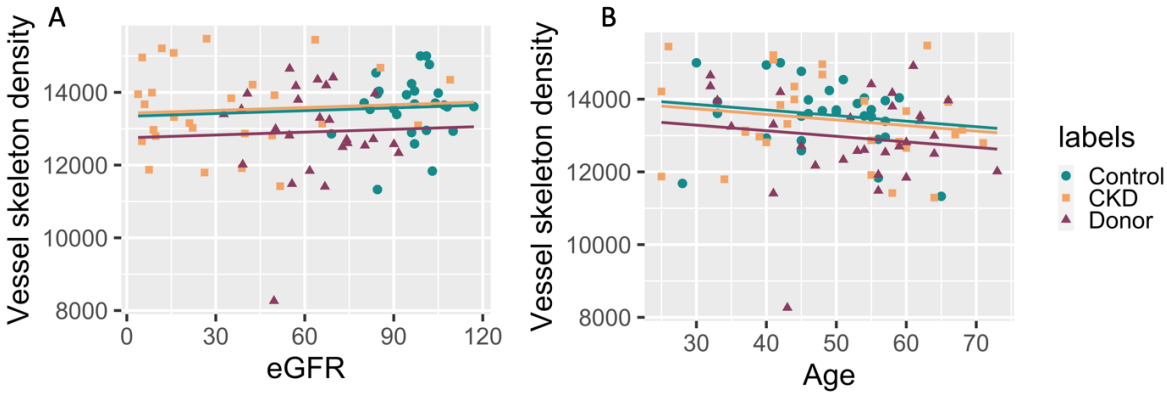

Figure F.2: (A) Association vessel skeleton density and age. (B)Association vessel skeleton density and eGFR.

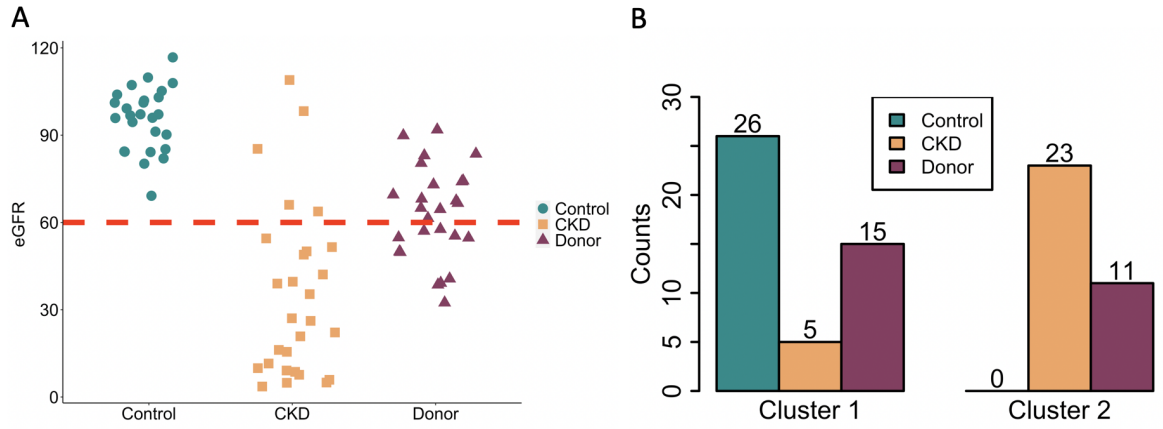

Figure F.3: (A) eGFR values. (B) Classification according to the clinical threshold (eGFR = 60). Note: some eGFR values are missing.

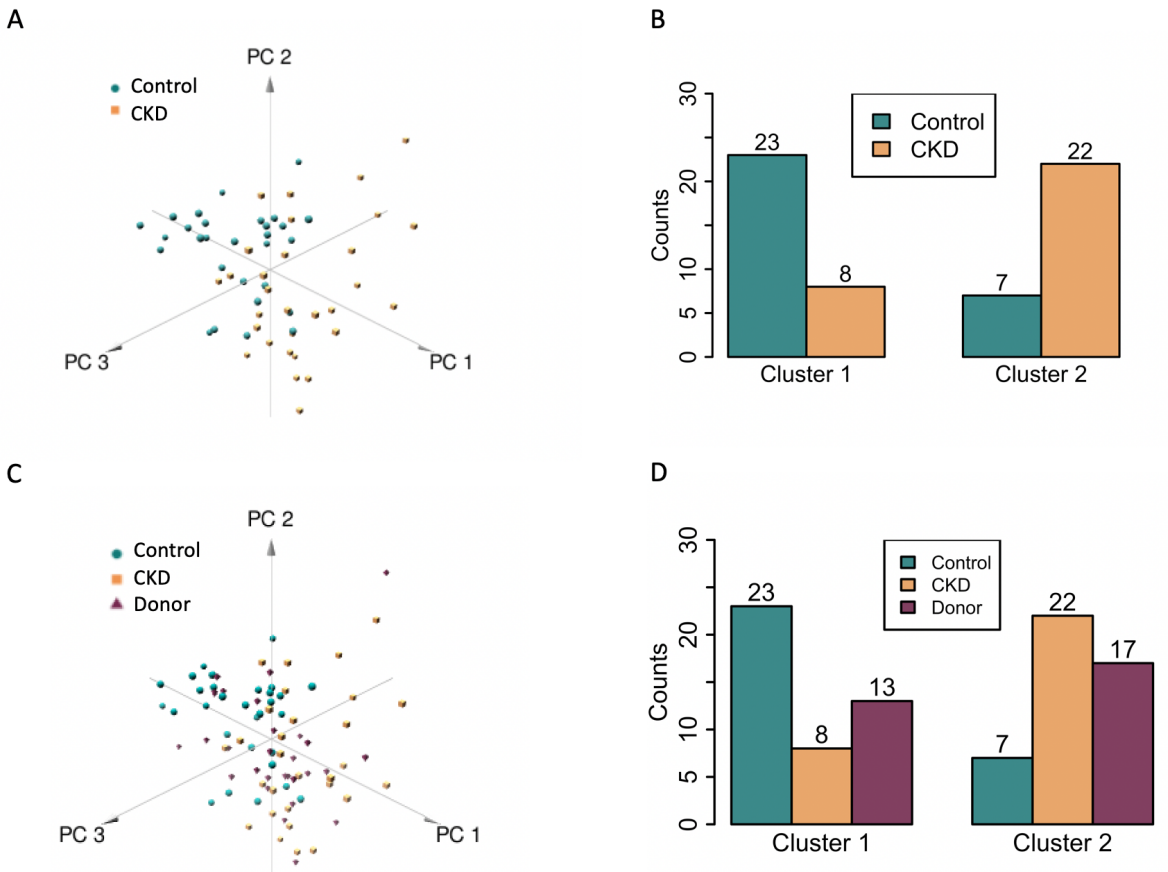

Figure F.4: (A) Principal component analysis. (B) Counts of patients in clusters 1 and 2.

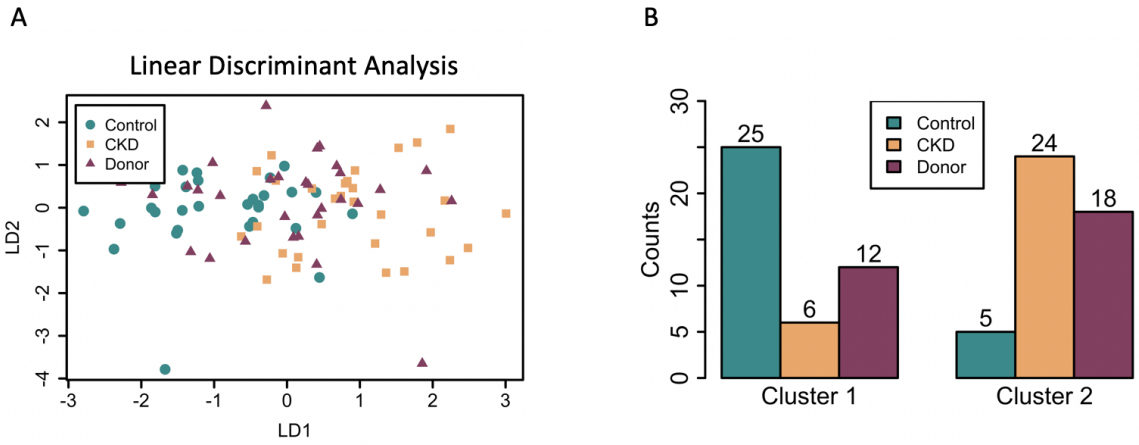

Figure F.5: (A) Linear discriminant analysis. (B) Clusters obtained using LD1 and LD2.

Bibliography

[1] D. S. Fong, L. Aiello, T. W. Gardner, G. L. King, G. Blankenship, J. D. Cavallerano, F. L. Ferris, and R. Klein, "Retinopathy in diabetes", *Diabetes Care*, vol. 27, no. suppl 1, s84–s87, 2004.

[2] T. E. Farrah, B. Dhillon, P. A. Keane, D. J. Webb, and N. Dhaun, "The eye, the kidney, and cardiovascular disease: old concepts, better tools, and new horizons", *Kidney International*, vol. 98, no. 2, pp. 323–342, 2020.

[3] J. Flammer, K. Konieczka, R. M. Bruno, A. Virdis, A. J. Flammer, and S. Taddei, "The eye and the heart", *European Heart Journal*, pp. 1270–1278, 2013.

[4] T. J. MacGillivray, E. Trucco, J. R. Cameron, B. Dhillon, J. G. Houston, and E. J. Van Beek, "Retinal imaging as a source of biomarkers for diagnosis, characterization and prognosis of chronic illness or long-term conditions", *British Journal of Radiology*, vol. 87, no. 1040, 2014.

[5] Y. Giarratano, E. Bianchi, C. Gray, A. Morris, T. MacGillivray, B. Dhillon, and M. O. Bernabeu, "Automated Segmentation of Optical Coherence Tomography Angiography Images: Benchmark Data and Clinically Relevant Metrics", *Translational Vision Science & Technology*, vol. 9, no. 13, 2020.

[6] Y. Giarratano, A. Pavel, J. Lian, R. Andreeva, A. Fontanella, R. Sarkar, L. J. Reid, S. Forbes, D. Pugh, T. E. Farrah, N. Dhaun, B. Dhillon, T. MacGillivray, and M. O. Bernabeu, *A Framework for the Discovery of Retinal Biomarkers in Optical Coherence Tomography Angiography (OCTA)*. Springer International Publishing, 2020, vol. 1, pp. 155–164.

[7] *Simple Anatomy of the Retina by Helga Kolb*, https://webvision.med.utah.edu/book/part-i-foundations/simple-anatomy-of-the-retina/, Accessed: 2021-05-21.

[8] J. Staal, M. Abramoff, M. Niemeijer, M. Viergever, and B. van Ginneken, "Ridge based vessel segmentation in color images of the retina", *IEEE Transactions on Medical Imaging*, vol. 23, no. 4, pp. 501–509, 2004.

[9] A. D. Hoover, V. Kouznetsova, and M. Goldbaum, "Locating blood vessels in retinal images by piecewise threshold probing of a matched filter response", *IEEE Transactions on Medical Imaging*, vol. 19, no. 3, pp. 203–210, 2000.

[10] *Messidor*, https://www.adcis.net/en/third-party/messidor/, Accessed: 2021-05-21.

[11] *UK Biobank*, https://www.ukbiobank.ac.uk/, Accessed: 2021-05-21.

[12] *SCONe*, https://www.ed.ac.uk/clinical-sciences/ophthalmology/scone, Accessed: 2021-05-21.

[13] H. R. Novotny and D. L. Alvis, "A Method of Photographing Fluorescence in Circulating Blood in the Human Retina", *Circulation*, vol. XXIV, pp. 82–86, 1961.

[14] B. Katherine Hu, *Fundus Photography and Fluorescein Angiography of Susac's Syndrome. In: Moran CORE, University of Utah's Clinical Ophthalmology Resource for Education*, http://morancore.utah.edu/section-12-retina-and-vitreous/fundus-photography-and-fluorescein-angiography-of-susacs-syndrome/, Accessed: 2021-05-21.

[15] D. Huang, E. Swanson, C. Lin, and et al., "Optical coherence tomography", *Science*, vol. 254, no. 5035, pp. 1178–1181, 1991.

[16] J. M. Schmitt, M. Yadlowsky, and R. Bonner, "Subsurface Imaging of Living Skin with Optical Coherence Microscopy", *Dermatology*, vol. 191, pp. 93–98, 1995.

[17] J. Fujimoto, M. Brezinski, G. Tearney, S. Boppart, B. Bouma, M. Hee, J. Southern, and S. E.A., "Optical biopsy and imaging using optical coherence tomography", *Nature Medicine*, vol. 1, no. 9, pp. 970–972, 1995.

[18] S. Boppart, J. Herrmann, C. Pitris, D. Stamper, M. Brezinski, and J. Fujimoto, "High-resolution optical coherence tomography-guided laser ablation of surgical tissue", *Journal of Surgical Research*, vol. 82, no. 2, pp. 275–284, 1999.

[19] *The OCT Photoreceptor Integrity Line*, http://www.achromatopsia.info/reduced-visual-acuity/, Accessed: 2021-05-21.

[20] S. Schaal, A. ElTanboly, M. Ismail, A. Switala, A. Shalaby, and et al., "A novel automated method for the objective quantification of Retinal layers reveals

sequential changes that occur in the Normal retina with age", *Frontiers in Nanoscience and Nanotechnology*, 2016.

[21] J. Campbell, M. Zhang, T. Hwang, S. Bailey, D. Wilson, Y. Jia, and D. Huang, "Detailed Vascular Anatomy of the Human Retina by Projection- Resolved Optical Coherence Tomography Angiography", *Scientific Reports*, no. September, pp. 1–11, 2017.

[22] J. Park, B. Soetikno, and A. Fawzi, "CHARACTERIZATION OF THE MIDDLE CAPILLARY PLEXUS USING OPTICAL COHERENCE TOMOGRAPHY ANGIOGRAPHY IN HEALTHY AND DIABETIC EYES", *Retina*, vol. 36, no. 11, pp. 2039–2050, 2016.

[23] F. Corvi, M. Pellegrini, S. Erba, M. Cozzi, G. Staurenghi, and A. Giani, "Reproducibility of Vessel Density, Fractal Dimension, and Foveal Avascular Zone Using 7 Different Optical Coherence Tomography Angiography Devices", *American Journal of Ophthalmology*, vol. 186, pp. 25–31, 2018.

[24] X. Li, W. Wu, H. Zhou, J. Deng, M. Zhao, T. Qian, C. Yan, X. Xu, and S. Yu, "A quantitative comparison of five optical coherence tomography angiography systems in clinical performance", *International Journal of Ophthalmology*, vol. 11, pp. 1784–1795, 2018.

[25] Y. Jia, O. Tan, J. Tokayer, B. Potsaid, Y. Wang, J. Jonathan, M. F. Kraus, H. Subhash, J. G. Fujimoto, J. Hornegger, and D. Huang, "Angiography with optical coherence tomography", *Optics Express*, vol. 20, no. 4, pp. 3116–3121, 2012.

[26] G. Coscas, "Heidelberg Spectralis Optical Coherence Tomography Angiography : Technical Aspects", *Developments in Ophthalmology*, vol. 56, pp. 1–5, 2016.

[27] R. K. Wang, "Angiography with optical coherence tomography", *IEEE Journal of Selected Topics in Quantum Electronics*, vol. 16, no. 3, pp. 545–554, 2010.

[28] J. Xu, S. Song, Y. Li, and R. Wang, "Complex-based oct angiography algorithm recovers microvascular information superior to amplitude or phase-based algorithm in phase-stable systems", *Physics in Medicine and Biology*, vol. 63, no. 1, pp. 1–29, 2018.

[29] Canon, *OCT-HS100 OPTICAL COHERENCE TOMOGRAPHY*. [Online]. Available: https://www.cmi.sk/sites/default/files/oct-hs100.pdf/.

[30] M. I. Ł. C. Hlebiej, I. W. G. Orczynska, A. N. R. Utkowski, J. A. K. Luczewski, T. O. G. Rzona, E. W. P. Ijewska, B. A. L. S. Ikorski, A. N. N. A. S. Zkulmowska, and M. Aciej, "Quality improvement of OCT angiograms with elliptical directional filtering", *Biomedical Optics Express*, vol. 10, no. 2, pp. 1013–1031, 2019.

[31] M. Chlebiej, I. Gorczynska, A. Rutkowski, J. Kluczewski, T. Grzona, E. Pijewska, B. L. Sikorski, A. Szkulmowska, and M. Szkulmowski, "Quality improvement of oct angiograms with elliptical directional filtering", *Biomedical Optics Express*, vol. 10, no. 2, pp. 1013–1031, Feb. 2019.

[32] B. Braaf, M. G. O. Gräfe, N. Uribe-Patarroyo, B. E. Bouma, B. J. Vakoc, J. F. de Boer, S. Donner, and J. Weichsel, "Oct-based velocimetry for blood flow quantification", in *High Resolution Imaging in Microscopy and Ophthalmology: New Frontiers in Biomedical Optics*, J. F. Bille, Ed. Cham: Springer International Publishing, 2019, pp. 161–179.

[33] B. Braaf, S. Donner, N. Uribe-patarroyo, B. E. Bouma, and B. J. Vakoc, " A Neural Network Approach to Quantify Blood Flow from Retinal OCT Intensity Time-Series Measurements", *Scientific Reports*, vol. 10, no. 9611, pp. 1–13, 2020.

[34] G. Savini, P. Barboni, V. Parisi, and M. Carbonelli, "The influence of axial length on retinal nerve fibre layer thickness and optic-disc size measurements by spectral-domain OCT", *British Journal of Ophthalmology*, vol. 96, no. 1, pp. 57–61, 2012.

[35] D. M. Sampson, P. Gong, D. An, M. Menghini, A. Hansen, D. A. Mackey, D. D. Sampson, and F. K. Chen, "Axial length variation impacts on superficial retinal vessel density and foveal avascular zone area measurements using optical coherence tomography angiography", *Investigative Ophthalmology & Visual Science*, vol. 58, no. 7, pp. 3065–3072, 2017.

[36] B. D. Krawitz, S. Mo, L. S. Geyman, S. A. Agemy, N. K. Scripsema, P. M. Garcia, T. Y. Chui, and R. B. Rosen, "Acircularity index and axis ratio of the foveal avascular zone in diabetic eyes and healthy controls measured by optical coherence tomography angiography", *Vision Research*, vol. 139, pp. 177–186, 2017.

[37] F. Y. Tang, D. S. Ng, A. Lam, F. Luk, R. Wong, C. Chan, S. Mohamed, A. Fong, J. Lok, T. Tso, F. Lai, M. Brelen, T. Y. Wong, C. C. Tham, and C. Y. Cheung, "Determinants of Quantitative Optical Coherence Tomography Angiography Metrics in Patients with Diabetes", vol. 7, no. 1, pp. 1–10, 2017.

[38] W. Choi, N. K. Waheed, E. M. Moult, M. Adhi, B. Lee, T. De Carlo, V. Jayaraman, C. R. Baumal, J. S. Duker, and J. G. Fujimoto, "Ultrahigh Speed Swept Source Optical Coherence Tomography Angiography of Retinal and Choriocapillaris Alterations in Diabetic Patients With and Without Retinopathy", *Retina*, vol. 37, no. 1, pp. 11–21, 2017.

[39] S. Zahid, R. Dolz-Marco, K. B. Freund, C. Balaratnasingam, K. Dansingani, F. Gilani, N. Mehta, E. Young, M. R. Klifto, B. Chae, L. A. Yannuzzi, and J. A. Young, "Fractal Dimensional Analysis of Optical Coherence Tomography Angiography in Eyes With Diabetic Retinopathy", *Investigative Ophthalmology & Visual Science*, vol. 57, no. 11, pp. 4940–4947, 2016.

[40] H. L. Rao, Z. S. Pradhan, M. H. Suh, S. Moghimi, K. Mansouri, and R. N. Weinreb, "Optical Coherence Tomography Angiography in Glaucoma", *Journal of Glaucoma*, vol. 29, no. 4, pp. 312–321, 2020.

[41] P. L. Nesper, P. K. Roberts, A. C. Onishi, H. Chai, L. Liu, L. M. Jampol, and A. A. Fawzi, "Quantifying Microvascular Abnormalities With Increasing Severity of Diabetic Retinopathy Using Optical Coherence Tomography Angiography", *Investigative ophthalmology & Visual Science*, vol. 58, no. 6, BIO307–BIO315, 2017.

[42] A. Kasumovic, I. Matoc, D. Rebic, N. Avdagic, and T. Halimic, "Assessment of Retinal Microangiopathy in Chronic Kidney Disease Patients", *Medical archives (Sarajevo, Bosnia and Herzegovina)*, vol. 74, no. 3, pp. 191–194, 2020.

[43] A. C. Onishi, P. L. Nesper, P. K. Roberts, G. A. Moharram, H. Chai, L. Liu, L. M. Jampol, and A. A. Fawzi, "Importance of considering the middle capillary plexus on OCT angiography in diabetic retinopathy", *Investigative Ophthalmology and Visual Science*, vol. 59, no. 5, pp. 2167–2176, 2018.

[44] Y. Ma, H. Hao, J. Xie, H. Fu, J. Zhang, J. Yang, Z. Wang, J. Liu, Y. Zheng, and Y. Zhao, "Rose: A retinal oct-angiography vessel segmentation dataset and new model", *IEEE Transactions on Medical Imaging*, vol. 40, no. 3, pp. 928–939, 2021.

[45] M. Li, Y. Zhang, Z. Ji, K. Xie, S. Yuan, Q. Liu, and Q. Chen, "IPN-V2 and OCTA-500: Methodology and dataset for retinal image segmentation", *arXiv*, pp. 1–12, 2020.

[46] "Early treatment diabetic retinopathy study design and baseline patient characteristics: Etdrs report number 7", *Ophthalmology*, vol. 98, no. 5, Supplement, pp. 741–756, 1991.

[47] H. Hammes, Y. Feng, F. Pfister, and M. Brownlee, "Diabetic retinopathy: Targeting vasoregression", *Diabetes*, vol. 60, no. 1, pp. 9–16, 2011.

[48] A. Y. Alibhai, E. M. Moult, R. Shahzad, C. B. Rebhun, C. Moreira-neto, M. Mcgowan, D. Lee, B. Lee, C. R. Baumal, A. J. Witkin, E. Reichel, J. S. Duker, J. G. Fujimoto, and N. K. Waheed, "Quantifying Microvascular Changes Using OCT Angiography in Diabetic Eyes without Clinical Evidence of Retinopathy", *Ophthalmology Retina*, vol. 2, no. 5, pp. 418–427, 2019.

[49] T. S. Hwang, S. S. Gao, L. Liu, A. K. Lauer, C. J. Flaxel, D. J. Wilson, D. Huang, Y. Jia, and O. Health, "Automated Quantification of Capillary Nonperfusion Using Optical Coherence Tomography Angiography in Diabetic Retinopathy", *JAMA Ophthalmology*, vol. 134, no. 4, pp. 367–373, 2016.

[50] A. Y. Kim, Z. Chu, A. Shahidzadeh, R. K. Wang, C. A. Puliafito, and A. H. Kashani, "Quantifying microvascular density and morphology in diabetic retinopathy using spectral-domain optical coherence tomography angiography", *Investigative Ophthalmology and Visual Science*, vol. 57, no. 9, OCT362–OCT370, 2016.

[51] N. Takase, M. Nozaki, A. Kato, H. Ozeki, M. Yoshida, and Y. Ogura, "Enlargement of foveal avascular zone in diabetic eyes evaluated by en face optical coherence tomography angiography", *Retina*, vol. 35, no. 11, pp. 2377–2383, 2015.

[52] L. Toto, E. Borrelli, L. Di Antonio, P. Carpineto, and R. Mastropasqua, "Retinal vascular plexuses' changes in dry age-related macular degeneration, evaluated by means of optical coherence tomography angiography", *Retina*, vol. 36, pp. 1566–1572, 2016.

[53] A. Miere, O. Semoun, S. Y. Cohen, A. El Ameen, M. Srour, C. Jung, H. Oubraham, G. Querques, and E. H. Souied, "Optical coherence tomography angiography features of subretinal fibrosis in age-related macular degeneration", *Retina*, vol. 35, pp. 2275–2284, 2015.

[54] *OCT-OptoVue*, https://www.oct-optovue.com/, Accessed: 2021-05-23.

[55] P. Lévêque, P. Zéboulon, E. Brasnu, C. Baudouin, and A. Labbé, "Optic Disc Vascularization in Glaucoma : Value of Spectral-Domain Optical Coherence Tomography Angiography", *Journal of Ophthalmology*, vol. 2016, 2016.

[56] K. D. Bojikian, C.-l. Chen, J. C. Wen, Q. Zhang, C. Xin, D. Gupta, R. C. Mudumbai, M. A. Johnstone, R. K. Wang, and P. Chen, "Optic Disc Perfusion in Primary Open Angle and Normal Tension Glaucoma Eyes Using Optical Coherence Tomography-Based Microangiography", *PLoS One*, vol. 11, no. 5, pp. 1–13, 2016.

[57] K. K. W. Cheng, B. L. Tan, L. Brown, C. Gray, E. Bianchi, B. Dhillon, T. Macgillivray, and A. J. Tatham, "Macular vessel density , branching complexity and foveal avascular zone size in normal tension glaucoma", *Scientific Reports*, pp. 1–9, 2021.

[58] J. M. Wardlaw, C. Smith, and M. Dichgans, "Mechanisms of sporadic cerebral small vessel disease: Insights from neuroimaging", *The Lancet Neurology*, vol. 12, no. 5, pp. 483–497, 2013.

[59] R. J. Cannistraro, M. Badi, B. H. Eidelman, D. W. Dickson, E. H. Middlebrooks, and J. F. Meschia, "Cns small vessel disease", *Neurology*, vol. 92, no. 24, pp. 1146–1156, 2019.

[60] S. P. Yoon, D. S. Grewal, A. C. Thompson, B. W. Polascik, C. Dunn, J. R. Burke, and S. Fekrat, "Retinal Microvascular and Neurodegenerative Changes in Alzheimer's Disease and Mild Cognitive Impairment Compared with Control Participants", *Ophthalmology Retina*, vol. 3, no. 6, pp. 489–499, 2019.

[61] O. M. Rifai, S. McGrory, C. B. Robbins, D. S. Grewal, A. Liu, S. Fekrat, and T. J. MacGillivray, "The application of optical coherence tomography angiography in Alzheimer's disease: A systematic review", *Alzheimer's & Dementia: Diagnosis, Assessment & Disease Monitoring*, vol. 13, no. 1, pp. 1–16, 2021.

[62] Y. Zhang, C. Shi, Y. Chen, W. Wang, S. Huang, Z. Han, X. Lin, F. Lu, and M. Shen, "Retinal Structural and Microvascular Alterations in Different Acute Ischemic Stroke Subtypes", *Journal of Ophthalmology*, vol. 2020, 2020.

[63] F. Costello and J. M. Burton, "Retinal imaging with optical coherence tomography: a biomarker in multiple sclerosis?", *Eye Brain*, vol. 31, no. 10, pp. 47–63, 2018.

[64] N. Feucht, M. Maier, G. Lepennetier, M. Pettenkofer, C. Wetzlmair, T. Daltrozzo, P. Scherm, C. Zimmer, M.-M. Hoshi, B. Hemmer, T. Korn, and B. Knier, "Optical

coherence tomography angiography indicates associations of the retinal vascular network and disease activity in multiple sclerosis", *Multiple Sclerosis Journal*, vol. 25, no. 2, pp. 224–234, 2019.

[65] X. Wang, Y. Jia, R. Spain, B. Potsaid, J. J. Liu, B. Baumann, J. Hornegger, J. G. Fujimoto, Q. Wu, and D. Huang, "Optical coherence tomography angiography of optic nerve head and parafovea in multiple sclerosis", *British Journal of Ophthalmology*, vol. 98, no. 10, pp. 1368–1373, 2014.

[66] R. Iliescu, S. R. Fernandez, S. Kelsen, C. Maric, and A. R. Chade, "Role of renal microcirculation in experimental renovascular disease", *Nephrology Dialysis Transplantation*, vol. 25, no. 4, pp. 1079–1087, 2010.

[67] M. Vadalà, M. Castellucci, G. Guarrasi, M. Terrasi, T. La Blasca, and G. Mulè, "Retinal and choroidal vasculature changes associated with chronic kidney disease", *Graefe's Archive for Clinical and Experimental Ophthalmology*, vol. 257, no. 8, pp. 1687–1698, 2019.

[68] L. Yeung, I. W. Wu, C. C. Sun, C. F. Liu, S. Y. Chen, C. H. Tseng, H. C. Lee, and C. C. Lee, "Early retinal microvascular abnormalities in patients with chronic kidney disease", *Microcirculation*, vol. 26, no. 7, pp. 1–10, 2019.

[69] I. W. Wu, C. C. Sun, C. C. Lee, C. F. Liu, T. Y. Wong, S. Y. Chen, J. C. C. Huang, C. H. Tseng, and L. Yeung, "Retinal neurovascular changes in chronic kidney disease", *Acta Ophthalmologica*, vol. 98, no. 7, e848–e855, 2020.

[70] *World Health Organization*, https://www.who.int/health-topics/cardiovascular-diseases/, Accessed: 2021-06-29.

[71] J. Wang, J. J. Iang, Y. Z. Hang, Y. W. Q. Ian, and J. F. Z. Hang, "Retinal and choroidal vascular changes in coronary heart disease : an optical coherence tomography angiography study", *Biomedical Optics Express*, vol. 10, no. 4, pp. 1532–1544, 2019.

[72] L. Arnould, C. Guenancia, A. Azemar, G. Alan, S. Pitois, F. Bichat, M. Zeller, P.-H. Gabrielle, A. M. Bron, C. Creuzot-Garcher, and Y. Cottin, "The EYE-MI Pilot Study: A Prospective Acute Coronary Syndrome Cohort Evaluated With Retinal Optical Coherence Tomography Angiography", *Investigative Ophthalmology & Visual Science*, vol. 59, no. 10, pp. 4299–4306, 2018.

[73] *High blood pressure (hypertension)*, https : / / www . mayoclinic . org / diseases - conditions / high - blood - pressure / symptoms - causes / syc - 20373410, Accessed: 2021-06-15.

[74] C. Sun, C. Ladores, J. Hong, D. Q. Nguyen, J. Chua, D. Ting, L. Schmetterer, T. Y. Wong, C. Y. Cheng, and A. C. Tan, "Systemic hypertension associated retinal microvascular changes can be detected with optical coherence tomography angiography", *Scientific Reports*, vol. 10, no. 1, pp. 1–9, 2020.

[75] W. H. Lee, J.-h. Park, Y. Won, M.-w. Lee, Y.-i. Shin, Y.-j. Jo, and J.-y. Kim, "Retinal Microvascular Change in Hypertension as measured by Optical Coherence Tomography Angiography", *Scientific Reports*, no. November 2018, pp. 1–7, 2019.

[76] C. R. Baumal, "Optical Coherence Tomography Angiography of Retinal Artery Occlusion", *Developments in Ophthalmology*, vol. 56, pp. 122–131, 2016.

[77] G. Damento, M. H. Chen, and T. Leng, "Spectral-domain optical coherence tomography angiography of central retinal artery occlusion", *Ophthalmic Surgery, Lasers and Imaging Retina*, vol. 47, no. 5, pp. 467–470, 2016.

[78] G. Tsai, T. Banaee, F. F. Conti, R. P. Singh, and C. Clinic, "Review article Optical Coherence Tomography Angiography in Eyes with Retinal Vein Occlusion", *Journal of Ophthalmic and Vision Research*, vol. 13, no. 3, pp. 315–322, 2018.

[79] T. M. Aslam, D. C. Hoyle, V. Puri, and G. Bento, "Differentiation of Diabetic Status Using Statistical and Tomography Angiography Images", *Translational Vision Science & Technology*, pp. 1–10, 2020.

[80] M. Alam, Y. Zhang, J. I. Lim, R. V. Chan, M. Yang, and X. Yao, "Quantitative Optical Coherence Tomography Angiography Features for Objective Classification and Staging of Diabetic Retinopathy", *Retina (Philadelphia, Pa.)*, vol. 40, no. 2, pp. 322–332, 2020.

[81] H. S. Sandhu, N. Eladawi, M. Elmogy, R. Keynton, O. Helmy, S. Schaal, and A. El-Baz, "Automated diabetic retinopathy detection using optical coherence tomography angiography: A pilot study", *British Journal of Ophthalmology*, vol. 102, no. 11, pp. 1564–1569, 2018.

[82] D. Le, M. Alam, C. K. Yao, J. I. Lim, Y.-T. Hsieh, R. V. P. Chan, D. Toslak, and X. Yao, "Transfer Learning for Automated OCTA Detection of Diabetic Retinopathy", *Translational Vision Science & Technology*, vol. 9, no. 2, pp. 35–35, 2020.

[83] S. Moccia, E. De Momi, S. El Hadji, and L. S. Mattos, "Blood vessel segmentation algorithms — Review of methods, datasets and evaluation metrics", *Computer Methods and Programs in Biomedicine*, vol. 158, pp. 71–91, 2018.

[84] T. E. De Carlo, A. T. Chin, M. A. Bonini Filho, M. Adhi, L. Branchini, D. A. Salz, C. R. Baumal, C. Crawford, E. Reichel, A. J. Witkin, J. S. Duker, and N. K. Waheed, "Detection of microvascular changes in eyes of patients with diabetes but not clinical diabetic retinopathy using optical coherence tomography angiography", *Retina*, vol. 35, no. 11, pp. 2364–2370, 2015.

[85] A. H. Kashani, C.-l. Chen, J. K. Gahm, F. Zheng, G. M. Richter, P. J. Rosenfeld, Y. Shi, and R. K. Wang, "Progress in Retinal and Eye Research Optical coherence tomography angiography : A comprehensive review of current methods and clinical applications", *Progress in Retinal and Eye Research*, vol. 60, pp. 66–100, 2017.

[86] R. Reif, J. Qin, L. An, Z. Zhi, S. Dziennis, and R. Wang, "Quantifying optical microangiography images obtained from a spectral domain optical coherence tomography system", *International Journal of Biomedical Imaging*, vol. 2012, 2012.

[87] M. Zhang, T. S. Hwang, C. Dongye, D. J. Wilson, D. Huang, and Y. Jia, "Automated quantification of nonperfusion in three retinal plexuses using projection-resolved optical coherence tomography angiography in diabetic retinopathy", *Investigative Ophthalmology and Visual Science*, vol. 57, no. 13, pp. 5101–5106, 2016.

[88] T. G. Schmidt, R. E. Linderman, M. R. Strampe, T. Y. Chui, R. B. Rosen, and J. Carroll, "The utility of frame averaging for automated algorithms in analyzing retinal vascular biomarkers in angiovue OCTA", *Translational Vision Science and Technology*, vol. 8, no. 1, 2019.

[89] N. Kanopoulos, N. Vasanthavada, and R. L. Baker, "Design of an image edge detection filter using the sobel operator", *IEEE Journal of solid-state circuits*, vol. 23, no. 2, pp. 358–367, 1988.

[90] D. A. Jesus, J. Barbosa Breda, K. Van Keer, A. Rocha Sousa, L. Abegão Pinto, and I. Stalmans, "Quantitative automated circumpapillary microvascular density

measurements: a new angioOCT-based methodology", *Eye (Basingstoke)*, vol. 33, no. 2, pp. 320–326, 2019.

[91] N. Eladawi, M. Elmogy, O. Helmy, A. Aboelfetouh, A. Riad, H. Sandhu, S. Schaal, and A. El-Baz, "Automatic blood vessels segmentation based on different retinal maps from OCTA scans", *Computers in Biology and Medicine*, vol. 89, no. August, pp. 150–161, 2017.

[92] P. Prentašic, M. Heisler, Z. Mammo, S. Lee, A. Merkur, E. Navajas, M. F. Beg, M. Šarunic, and S. Loncaric, "Segmentation of the foveal microvasculature using deep learning networks", *Journal of Biomedical Optics*, vol. 21, no. 7, p. 075 008, 2016.

[93] L. Mou, Y. Zhao, L. Chen, J. Cheng, Z. Gu, H. Hao, H. Qi, Y. Zheng, A. Frangi, and J. Liu, "Cs-net: Channel and spatial attention network for curvilinear structure segmentation", in *Medical Image Computing and Computer Assisted Intervention – MICCAI 2019*, D. Shen, T. Liu, T. M. Peters, L. H. Staib, C. Essert, S. Zhou, P.-T. Yap, and A. Khan, Eds., Cham: Springer International Publishing, 2019, pp. 721–730.

[94] C. W. Ritchie, K. Wells, and K. Ritchie, "The PREVENT research programme-A novel research programme to identify and manage midlife risk for dementia: The conceptual framework", *International Review of Psychiatry*, vol. 25, no. 6, pp. 748–754, 2013.

[95] P. A. Yushkevich, J. Piven, H. Cody Hazlett, R. Gimpel Smith, S. Ho, J. C. Gee, and G. Gerig, "User-guided 3D active contour segmentation of anatomical structures: Significantly improved efficiency and reliability", *Neuroimage*, vol. 31, no. 3, pp. 1116–1128, 2006.

[96] A. F. Frangi, W. J. Niessen, K. L. Vincken, and M. A. Viergever, "Multiscale vessel enhancement filtering", in *Medical Image Computing and Computer-Assisted Intervention - MICCAI'98*, A. C. W.M. Wells and S. Delp, Eds., ser. Lecture Notes in Computer Science, vol. 1496, Berlin, Germany: Springer Verlag, 1998, pp. 130–137.

[97] D. Kroon, *Hessian based frangi vesselness filter*, https://www.mathworks.com/matlabcentral/fileexchange/24409-hessian-based-frangi-vesselness-filter, Accessed: 2019-09-30.

[98] J. V. Soares, J. J. Leandro, R. M. Cesar, H. F. Jelinek, and M. J. Cree, "Retinal vessel segmentation using the 2-D Gabor wavelet and supervised classification", *IEEE*

Transactions on Medical Imaging, vol. 25, no. 9, pp. 1214–1222, 2006. eprint: 0510001 (cs).

[99] R. Annunziata and E. Trucco, "Accelerating Convolutional Sparse Coding for Curvilinear Structures Segmentation by Refining SCIRD-TS Filter Banks", *IEEE Transactions on Medical Imaging*, vol. 35, no. 11, pp. 2381–2392, 2016.

[100] M. W. Law and A. C. Chung, "Three dimensional curvilinear structure detection using optimally oriented flux", in *Computer Vision - ECCV 2008*, vol. 5305, Springer, 2008, pp. 368–382.

[101] A. Li, J. You, C. Du, and Y. Pan, "Automated segmentation and quantification of OCT angiography for tracking angiogenesis progression", *Biomedical Optics Express*, vol. 8, no. 12, p. 5604, 2017.

[102] W. Rawat and Z. Wang, "Deep Convolutional Neural Networks for Image Classification: A Comprehensive Review", *Neural Computation*, vol. 29, no. 9, pp. 2352–2449, Sep. 2017.

[103] O. Ronneberger, P. Fischer, and T. Brox, "U-net: Convolutional networks for biomedical image segmentation", in *Medical Image Computing and Computer-Assisted Intervention – MICCAI 2015*, N. Navab, J. Hornegger, W. M. Wells, and A. F. Frangi, Eds., Cham: Springer International Publishing, 2015, pp. 234–241.

[104] N. Otsu, "A threshold selection method from gray-level histograms", *IEEE Transactions on Systems, Man, and Cybernetics*, vol. 9, no. 1, pp. 62–66, 1979.

[105] D. Bradley and G. Roth, "Adaptive thresholding using the integral image", *Journal of Graphics Tools*, vol. 12, pp. 13–21, 2007.

[106] P. Rodrigues, P. Guimarães, T. Santos, S. Simão, T. Miranda, P. Serranho, and R. Bernardes, "Two-dimensional segmentation of the retinal vascular network from optical coherence tomography", *Journal of Biomedical Optics*, vol. 18, no. 12, p. 126 011, 2013.

[107] M. L. McHugh, "Interrater reliability: The kappa statistic", *Biochemia medica*, vol. 3, pp. 276–82, 2012.

[108] M. E. Gegundez-Arias, A. Aquino, J. M. Bravo, and D. Marin, "A function for quality evaluation of retinal vessel segmentations", *IEEE Transactions on Medical Imaging*, vol. 31, no. 2, pp. 231–239, 2012.

[109] X. Hu, L. Fuxin, D. Samaras, and C. Chen, "Topology-preserving deep image segmentation", *Advances in Neural Information Processing Systems*, vol. 32, no. NeurIPS, pp. 1–12, 2019.

[110] The GUDHI Project, *GUDHI User and Reference Manual*, 3.1.1. GUDHI Editorial Board, 2020. [Online]. Available: https://gudhi.inria.fr/doc/3.1.1/.

[111] D. Easley and J. Kleinberg, *Networks, Crowds, and Markets: Reasoning About a Highly Connected World*. USA: Cambridge University Press, 2010.

[112] M. Newman, *Networks: An Introduction*. USA: Oxford University Press, Inc., 2010.

[113] A. Chaiboonchoe, W. Jurkowski, J. Pellet, E. Glaab, A. Kolodkin, A. Raussel, A. Le Béchec, S. Ballereau, L. Meyniel, I. Crespo, H. Ahmed, V. Volpert, V. Lotteau, N. Baliga, L. Hood, A. d. Sol, R. Balling, and C. Auffray, "On different aspects of network analysis in systems biology", in *Systems Biology: Integrative Biology and Simulation Tools*, A. Prokop and B. Csukás, Eds. Dordrecht: Springer Netherlands, 2013, pp. 181–207.

[114] D. Watts and S. H. Strogatz, "Collective dynamics of 'small-world' networks", *Nature*, vol. 393, pp. 440–442, 1998.

[115] A.-L. "Barabási and R. Albert, "Emergence of scaling in random networks", *Science*, vol. 286, no. 5439, pp. 509–512, 1999.

[116] MATLAB, *version 9.9.0.1495850 (R2020b)*. Natick, Massachusetts: The MathWorks Inc., 2020.

[117] Y. Lu, M. Bernabeu, J. Lammer, C. Cai, M. Jones, C. Franco, L. Aiello, and J. Sun, "Computational fluid dynamics assisted characterization of parafoveal hemodynamics in normal and diabetic eyes using adaptive optics scanning laser ophthalmoscopy", *Biomedical Optics Express*, vol. 7, no. 12, pp. 33–38, 2017.

[118] Henderson, A., *Paraview guide, a parallel visualization application.* Kitware Inc., 2007.

[119] A. A. Hagberg, D. A. Schult, and P. J. Swart, "Exploring network structure, dynamics, and function using networkx", in *Proceedings of the 7th Python in Science Conference*, G. Varoquaux, T. Vaught, and J. Millman, Eds., Pasadena, CA USA, 2008, pp. 11–15.

[120] D. Muller and F. Preparata, "Finding the intersection of two convex polyhedra", *Theoretical Computer Science*, vol. 7, no. 2, pp. 217–236, 1978.

[121] S. Schneider and I. F. Sbalzarini, "Finding faces in a planar embedding of a graph", MOSAIC Group, MPI-CBG, Tech. Rep., 2015.

[122] M. Hiroki, K. Miyashita, and M. Oda, "Tortuosity of the white matter medullary arterioles is related to the severity of hypertension", *Cerebrovascular Diseases*, vol. 13, no. 4, pp. 242–250, 2002.

[123] M. B. Sasongko, T. Y. Wong, T. T. Nguyen, C. Y. Cheung, J. E. Shaw, and J. J. Wang, "Retinal vascular tortuosity in persons with diabetes and diabetic retinopathy", *Diabetologia*, vol. 54, no. 9, pp. 2409–2416, 2011.

[124] C. Y. L. Cheung, Y. Zheng, W. Hsu, M. L. Lee, Q. P. Lau, P. Mitchell, J. J. Wang, R. Klein, and T. Y. Wong, "Retinal vascular tortuosity, blood pressure, and cardiovascular risk factors", *Ophthalmology*, vol. 118, no. 5, pp. 812–818, 2011.

[125] E. Grisan, M. Foracchia, and A. Ruggeri, "A novel method for the automatic grading of retinal vessel tortuosity", *IEEE Transactions on Medical Imaging*, vol. 27, no. 3, pp. 310–319, 2008.

[126] W. E. Hart, M. Goldbaum, B. Côté, P. Kube, and M. R. Nelson, "Measurement and classification of retinal vascular tortuosity", *International Journal of Medical Informatics*, vol. 53, no. 2-3, pp. 239–252, 1999.

[127] E. Trucco, H. Azegrouz, and B. Dhillon, "Modeling the tortuosity of retinal vessels: Does caliber play a role?", *IEEE Transactions on Biomedical Engineering*, vol. 57, no. 9, pp. 2239–2247, 2010.

[128] E. Bullitt, G. Gerig, S. M. Pizer, W. Lin, and S. R. Aylward, "Measuring Tortuosity of the Intracerebral Vasculature from MRA Images", *IEEE Transactions on Medical Imaging*, vol. 22, no. 9, pp. 1163–1171, 2003.

[129] L. D. Corso, D. Moruzzo, B. Conte, M. Agelli, A. M. Romanelli, F. Pastine, M. Protti, F. Pentimone, and G. Baggiani, "Tortuosity, kinking, and coiling of the carotid artery: Expression of atherosclerosis or aging?", *Angiology*, vol. 49, no. 5, pp. 361–371, 1998.

[130] W. Lotmar, A. Freiburghaus, and D. Bracher, "Measurement of vessel tortuosity on fundus photographs", *Albrecht von Graefes Archiv für Klinische und Experimentelle Ophthalmologie*, vol. 211, no. 1, pp. 49–57, 1979.

[131] O. Smedby, N. Hogman, S. Nilsson, U. Erikson, A. Olsson, and G. Walldius, "Two-dimensional tortuosity of the superficial femoral artery in early atherosclerosis", *Journal of vascular research*, pp. 183–186, 1993.

[132] E. Bribiesca, "A measure of tortuosity based on chain coding", *Pattern Recognition*, vol. 46, pp. 716–724, 2013.

[133] L. Ramos, J. Novo, J. Rouco, S. Romeo, M. D. Álvarez, and M. Ortega, "Retinal vascular tortuosity assessment: Inter-intra expert analysis and correlation with computational measurements", *BMC Medical Research Methodology*, vol. 18, no. 1, pp. 1–11, 2018.

[134] N. Pržulj, D. G. Corneil, and I. Jurisica, "Modeling interactome: scale-free or geometric?", *Bioinformatics*, vol. 20, no. 18, pp. 3508–3515, 2004.

[135] N. Pržulj, "Biological network comparison using graphlet degree distribution", *Bioinformatics*, vol. 23, no. 2, e177–e183, 2007.

[136] W. Hayes, K. Sun, and N. Pržulj, "Graphlet-based measures are suitable for biological network comparison", *Bioinformatics*, vol. 29, no. 4, pp. 483–491, 2013.

[137] E. Katifori and M. O. Magnasco, "Quantifying loopy network architectures", *PLOS ONE*, vol. 7, no. 6, pp. 1–14, 2012.

[138] B. Y. Horton and E. Robert, "MORPHOLOGY", *Geological Society of America Bulletin*, vol. 56, no. March, pp. 275–370, 1945.

[139] C. Physics, "OpenStax", in *OpenStax*, OpenStax CNX, 2019, pp. 368–382.

[140] G. Hughes, "On the mean accuracy of statistical pattern recognizers", *IEEE Transactions on Information Theory*, vol. 14, no. 1, pp. 55–63, 1968.

[141] K. Kira and L. A. Rendell, "A practical approach to feature selection", in *Machine Learning Proceedings 1992*, D. Sleeman and P. Edwards, Eds., San Francisco (CA): Morgan Kaufmann, 1992, pp. 249–256.

[142] C. Ding and H. Peng, "Minimum redundancy feature selection from microarray gene expression data", *Journal of Bioinformatics and Computational Biology*, vol. 3, no. 2, pp. 185–205, 2005.

[143] S. Lee and D. K. Lee, "What is the proper way to apply the multiple comparison test?", *Korean Journal of Anesthesiology*, vol. 71, no. 5, pp. 353–360, 2018.

[144] R. Klein, M. D. Knudtson, K. E. Lee, R. Gangnon, and B. E. K. Klein, "The Wisconsin Epidemiologic Study of Diabetic Retinopathy: XXII the twenty-five-year progression of retinopathy in persons with type 1 diabetes", *Ophthalmology*, vol. 116, no. 3, pp. 497–503, 2009.

[145] R. A. Armstrong, "Statistical guidelines for the analysis of data obtained from one or both eyes", *Ophthalmic and Physiological Optics*, vol. 33, no. 1, pp. 7–14, 2013.

[146] *ImageNet*, https://www.image-net.org/, Accessed: 2021-06-03.

[147] R. Andreeva, A. Fontanella, Y. Giarratano, and M. O. Bernabeu, *DR Detection Using Optical Coherence Tomography Angiography (OCTA): A Transfer Learning Approach with Robustness Analysis*. Springer International Publishing, 2020, pp. 11–20.

[148] M. Chiesa, G. Maioli, G. I. Colombo, and L. Piacentini, "GARS : Genetic Algorithm for the identification of a Robust Subset of features in high-dimensional datasets", *BMC Bioinformatics*, vol. 21, pp. 1–11, 2020.

[149] L. G. Fine and J. T. Norman, "Chronic hypoxia as a mechanism of progression of chronic kidney diseases: From hypothesis to novel therapeutics", *Kidney International*, vol. 74, no. 7, pp. 867–872, 2008.

[150] D. H. Kang, J. Kanellis, C. Hugo, L. Truong, S. Anderson, D. Kerjaschki, G. F. Schreiner, and R. J. Johnson, "Role of the microvascular endothelium in progressive renal disease", *Journal of the American Society of Nephrology*, vol. 13, no. 3, pp. 806–816, 2002.

[151] M. Flisiński, A. Brymora, G. Elminowska-Wenda, J. Bogucka, K. Walasik, A. Stefańska, G. Odrowąż;-Sypniewska, and J. Manitius, "Influence of different stages of experimental chronic kidney disease on rats locomotor and postural skeletal muscles microcirculation", *Renal Failure*, vol. 30, no. 4, pp. 443–451, 2008.

[152] J. Törnig, K. Amann, E. Ritz, C. Nichols, M. Zeier, and G. Mall, "Arteriolar wall thickening, capillary rarefaction and interstitial fibrosis in the heart of rats with renal failure:the effects of ramipril, nifedipine and moxonidine.", *Journal of the American Society of Nephrology*, vol. 7, no. 5, pp. 667–675, 1996.

[153] T. Y. Wong, J. Coresh, R. Klein, P. Muntner, D. J. Couper, A. R. Sharrett, B. E. Klein, G. Heiss, L. D. Hubbard, and B. B. Duncan, "Retinal microvascular abnormalities

and renal dysfunction: The Atherosclerosis Risk in Communities Study", *Journal of the American Society of Nephrology*, vol. 15, no. 9, pp. 2469–2476, 2004.

[154] Q. L. Ooi, F. K. N. H. Tow, R. Deva, M. A. Alias, R. Kawasaki, T. Y. Wong, N. Mohamad, D. Colville, A. Hutchinson, and J. Savige, "The microvasculature in chronic kidney disease", *Clinical Journal of the American Society of Nephrology*, vol. 6, no. 8, pp. 1872–1878, 2011.

[155] L. S. Lim, C. Y.-l. Cheung, C. Sabanayagam, S. C. Lim, E. S. Tai, L. Huang, and T. Y. Wong, "Structural Changes in the Retinal Microvasculature and Renal Function", *Investigative Ophthalmology and Visual Science*, vol. 54, no. 4, pp. 1–3, 2013.

[156] N. K. Foundation, "K/doqi clinical practice guidelines for bone metabolism and disease in chronic kidney disease.", *American Journal of Kidney Diseases*, vol. 42, no. 4, S1–201, 2003.

[157] *World Health Organization*, https://www.who.int/transplantation/gkt/statistics/en/, Accessed: 2021-05-21.

[158] I. Fehrman-Ekholm, C. G. Elinder, M. Stenbeck, G. Tydén, and C. G. Groth, "Kidney donors live longer", *Transplantation*, vol. 64, no. 7, pp. 976–8, 1997.

[159] H. N. Ibrahim, R. Foley, L. Tan, T. Rogers, R. F. Bailey, H. Guo, C. R. Gross, and A. J. Matas, "Long-term consequences of kidney donation", *New England Journal of Medicine*, vol. 360, no. 5, pp. 459–469, 2009.

[160] G. Mjøen, S. Hallan, A. Hartmann, A. Foss, K. Midtvedt, O. Øyen, A. Reisæter, P. Pfeffer, T. Jenssen, T. Leivestad, P. D. Line, M. Øvrehus, D. O. Dale, H. Pihlstrøm, I. Holme, F. W. Dekker, and H. Holdaas, "Long-term risks for kidney donors", *Kidney International*, vol. 86, no. 1, pp. 162–167, 2014.

[161] A. D. Muzaale, A. B. Massie, M. C. Wang, R. A. Montgomery, M. A. McBride, J. L. Wainright, and D. L. Segev, "Risk of end-stage renal disease following live kidney donation", *JAMA - Journal of the American Medical Association*, vol. 311, no. 6, pp. 579–586, 2014.

[162] F. K. Sutter and H. Helbig, "Familial retinal arteriolar tortuosity: A review", *Survey of Ophthalmology*, vol. 48, no. 3, pp. 245–255, 2003.

[163] J. S. Wolffsohn, G. A. Napper, S.-M. Ho, A. Jaworski, and T. L. Pollard, "Improving the description of the retinal vasculature and patient history taking for monitoring

systemic hypertension", *Ophthalmic and Physiological Optics*, vol. 21, no. 6, pp. 441–449, 2001.

[164] T. Fawcett, "An introduction to roc analysis", *Pattern Recognition Letters*, vol. 27, no. 8, pp. 861–874, 2006, ROC Analysis in Pattern Recognition, ISSN: 0167-8655.

[165] F. Pedregosa, G. Varoquaux, A. Gramfort, V. Michel, B. Thirion, O. Grisel, M. Blondel, P. Prettenhofer, R. Weiss, V. Dubourg, J. Vanderplas, A. Passos, D. Cournapeau, M. Brucher, M. Perrot, and E. Duchesnay, "Scikit-learn: Machine learning in Python", *Journal of Machine Learning Research*, vol. 12, pp. 2825–2830, 2011.

[166] B. C. Ross, "Mutual Information between Discrete and Continuous Data Sets", *PLOS ONE*, vol. 9, no. 2, 2014.

[167] J. Clough, N. Byrne, I. Oksuz, V. A. Zimmer, J. A. Schnabel, and A. King, "A topological loss function for deep-learning based image segmentation using persistent homology", *IEEE Transactions on Pattern Analysis and Machine Intelligence*, pp. 1–1, 2020.